Cell

Neurons under T Cell Attack Coordinate Phagocyte-Mediated Synaptic Stripping

Graphical Abstract

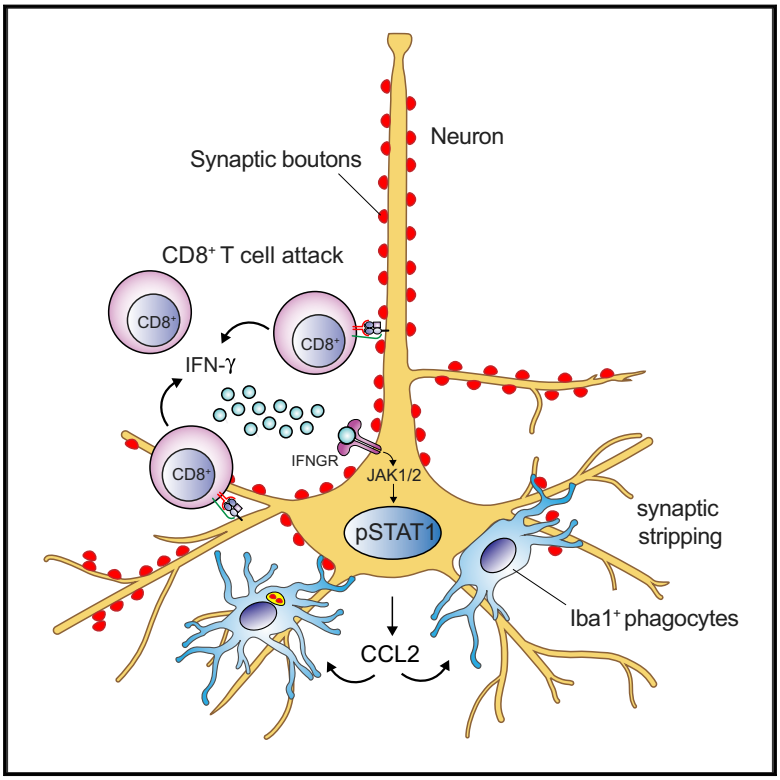

Authors

Giovanni Di Liberto, Stanislav Pantelyushin, Mario Kreutzfeldt, ..., Marco Prinz, Daniel D. Pinschewer, Doron Merkler

Correspondence

doron.merkler@unige.ch

In Brief

Neurons act as intermediaries between CD8+ T cells and phagocytes, driving their own synaptic loss during neuroinflammation.

Highlights

- Neuronal translatome during CD8+ T cell attack reveals disease-associated pathways
- Neuronally induced STAT1 and downstream CCL2 drive phagocyte-mediated synaptic loss
- STAT1/CCL2 signature is conserved in murine and human neuroinflammatory diseases
- Neuronal STAT1/CCL2 signaling blockade prevents synaptic stripping and disease

Data Resources

GSE110593

Di Liberto et al., 2018, Cell *175*, 1–14
October 4, 2018
https://doi.org/10.1016/j.cell.2018.07.049

CellPress

Please cite this article in press as: Di Liberto et al., Neurons under T Cell Attack Coordinate Phagocyte-Mediated Synaptic Stripping, Cell (2018), https://doi.org/10.1016/j.cell.2018.07.049

Article

Cell

Neurons under T Cell Attack Coordinate Phagocyte-Mediated Synaptic Stripping

Giovanni Di Liberto,[1] Stanislav Pantelyushin,[1,10] Mario Kreutzfeldt,[1] Nicolas Page,[1] Stefano Musardo,[2] Roland Coras,[3] Karin Steinbach,[1] Ilena Vincenti,[1] Bogna Klimek,[1] Thomas Lingner,[4] Gabriela Salinas,[4] Nathalie Lin-Marq,[5] Ori Staszewski,[6] Marta Joana Costa Jordão,[6] Ingrid Wagner,[1] Kristof Egervari,[1,5] Matthias Mack,[7] Camilla Bellone,[2] Ingmar Blümcke,[3] Marco Prinz,[6,8] Daniel D. Pinschewer,[9] and Doron Merkler[1,5,11,*]

[1]Department of Pathology and Immunology, University of Geneva, 1211 Geneva, Switzerland
[2]Department of Basic Neuroscience, University of Geneva, 1205 Geneva, Switzerland
[3]Department of Neuropathology, University Hospital Erlangen, 91054 Erlangen, Germany
[4]Microarray and Deep-Sequencing Core Facility, Institute for Developmental Biochemistry, University Medical Center Göttingen, Göttingen, Germany
[5]Division of Clinical Pathology, Geneva University Hospital, 1211 Geneva, Switzerland
[6]Institute of Neuropathology, Medical Faculty, University of Freiburg, Freiburg, Germany
[7]Department of Internal Medicine II – Nephrology, Regensburg Center for Interventional Immunology, Regensburg, Germany
[8]BIOSS Centre for Biological Signalling Studies, University of Freiburg, Freiburg, Germany
[9]Department of Biomedicine – Haus Petersplatz, Division of Experimental Virology, University of Basel, Basel, Switzerland
[10]Present address: Institute of Laboratory Animal Science, University of Zurich, Zurich, Switzerland
[11]Lead Contact
*Correspondence: doron.merkler@unige.ch
https://doi.org/10.1016/j.cell.2018.07.049

SUMMARY

Inflammatory disorders of the CNS are frequently accompanied by synaptic loss, which is thought to involve phagocytic microglia and complement components. However, the mechanisms accounting for aberrant synaptic connectivity in the context of CD8$^+$ T cell-driven neuronal damage are poorly understood. Here, we profiled the neuronal translatome in a murine model of encephalitis caused by CD8$^+$ T cells targeting antigenic neurons. Neuronal STAT1 signaling and downstream CCL2 expression were essential for apposition of phagocytes, ensuing synaptic loss and neurological disease. Analogous observations were made in the brains of Rasmussen's encephalitis patients. In this devastating CD8$^+$ T cell-driven autoimmune disease, neuronal STAT1 phosphorylation and CCL2 expression co-clustered with infiltrating CD8$^+$ T cells as well as phagocytes. Taken together, our findings uncover an active role of neurons in coordinating phagocyte-mediated synaptic loss and highlight neuronal STAT1 and CCL2 as critical steps in this process that are amenable to pharmacological interventions.

INTRODUCTION

Correct synaptic wiring is a fundamental prerequisite for proper neuronal functioning. Microglia, the brain-resident phagocytes, are important orchestrators of synaptic refinement and maintenance (Paolicelli et al., 2011). However, in the context of CNS inflammation, microglia, together with brain-infiltrating monocyte-derived macrophages, can promote pathological synaptic loss (Klein and Hunter, 2017; Prinz et al., 2017). Activated microglia engulf synaptic terminals in CNS inflammatory conditions through an interferon-α-dependent mechanism (Bialas et al., 2017) and complement component C3 cleavage products (Vasek et al., 2016).

In addition to phagocytes, cytotoxic CD8$^+$ T cells can also target neurons in neuroinflammatory conditions. These include viral infections (Chevalier et al., 2011), autoimmune diseases (Liblau et al., 2013), and paraneoplastic neurological disorders (Bien et al., 2012). Therefore, CD8$^+$ T cells damage neurons upon recognition of their cognate peptide-major histocompatibility complex (MHC) class I complex (Chevalier et al., 2011). This process can lead to cell death and, thus, irreversible neuronal dropout (Bernard-Valnet et al., 2016). Alternatively, it can trigger transection of neuronal processes, synaptic loss, and, thus, disruption of neuronal connectivity (Medana et al., 2001; Merkler et al., 2006). Aberrant synaptic inputs can alter neuronal excitability, which manifests as seizures and a decline in intellectual and motor performance (Vezzani et al., 2011). The cellular and molecular bases of CD8$^+$ T cell-driven synaptic pathology are currently unclear. It has been proposed that phagocytes are effectors of CD8$^+$ T cell-driven tissue damage (Kim et al., 2009). One may thus hypothesize that microglia execute CD8$^+$ T cell-driven synaptic degeneration, which remains to be tested experimentally.

We previously described an animal model (Merkler et al., 2006) in which CD8$^+$ T cell-derived interferon-γ (IFN-γ) triggered an acute loss of axosomatic synaptic connections, which clinically manifested as impaired motor coordination and balance (Kreutzfeldt et al., 2013). In this model, referred to as viral déjà vu, neonatal intra-cerebral (i.c.) infection of mice with an attenuated lymphocytic choriomeningitis virus (LCMV) variant (referred to as rLCMV) leads to viral persistence restricted to

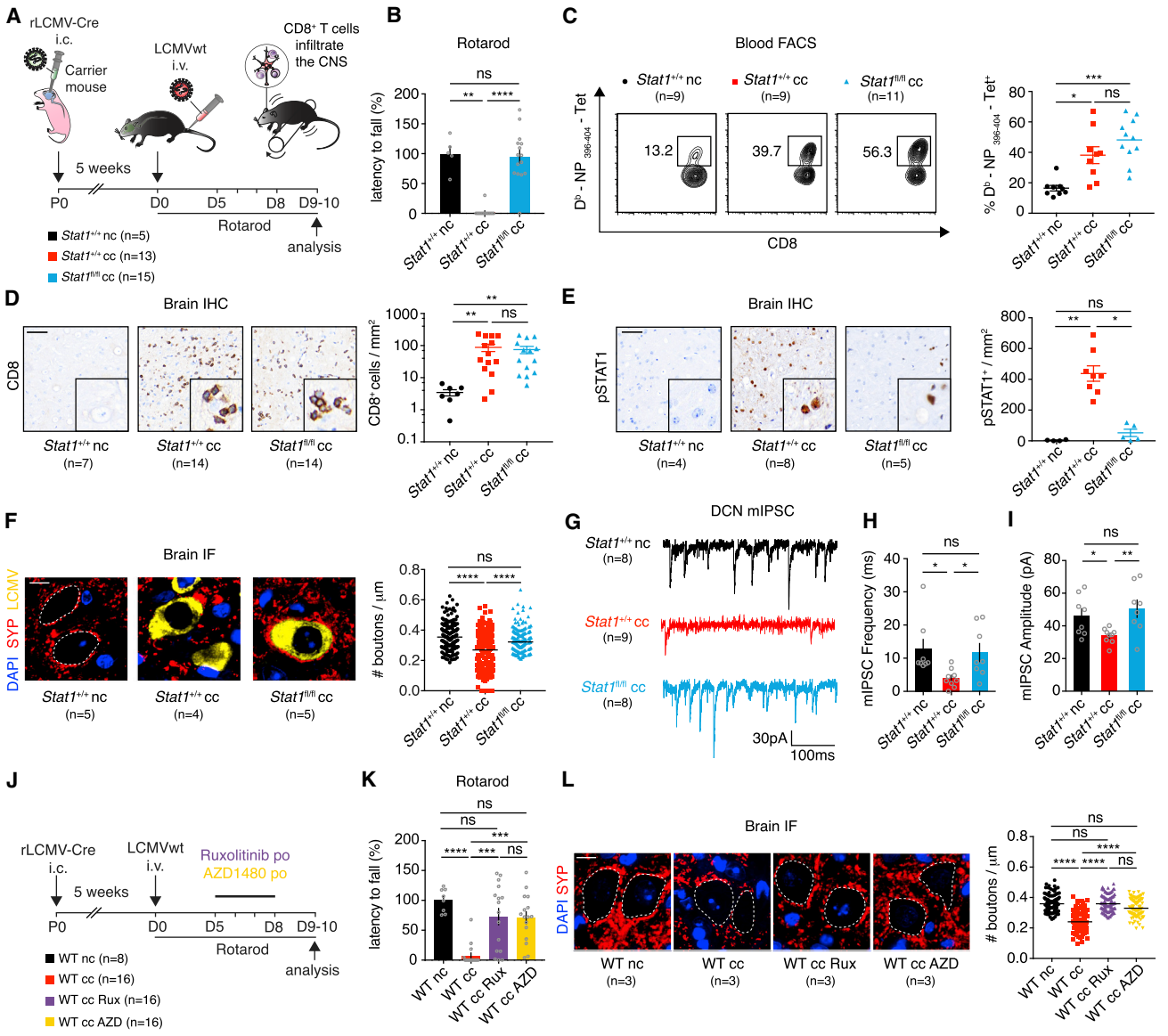

Figure 1. Neuronal JAK-STAT1 Signaling Is Essential for Synaptic Alterations and Motor Impairment in Viral Déjà Vu

(A) Experimental setup of viral déjà vu. *Stat1*$^{+/+}$ or *Stat1*$^{fl/fl}$ mice were infected intracerebrally (i.c.) with attenuated LCMV encoding for the Cre recombinase (rLCMV-Cre). At around 5 weeks of age, rLCMV-Cre carrier mice were challenged (cc) intravenously (i.v.) with LCMVwt to trigger a CD8$^+$ T cell response directed against the H-2D^b NP$_{396–404}$ epitope shared between rLCMV and LCMVwt (viral déjà vu). Motor performance was monitored by rotarod test for the subsequent days as indicated. At disease peak (days 9–10), brains were processed for histology (D–F) and electrophysiological recordings (G–I). *Stat1*$^{+/+}$ mice without neonatal infection but challenged with LCMVwt (non-carrier challenged, nc) served as controls.

(B) Rotarod performance of the indicated groups.

(C) Flow cytometry analysis of D^b-NP$_{396–404}$ Tet$^+$ CD8$^+$ T cells in the blood at disease peak.

(D) Representative images and quantification of CD8$^+$ T cells in the brain stem stained by immunohistochemistry (IHC).

(E) Representative IHC images and quantification of phosphorylated STAT1 (pSTAT1) in DCN. Scale bar, 50 µm; insets, 40 µm.

(F) Representative immunostainings for synaptophysin (SYP), LCMV-nucleoprotein (LCMV), and nuclei (DAPI) in DCN. Symbols represent DCN neurons (n = 29–60 neurons per mouse). Lines indicate the median. Scale bar, 10 µm.

(G–I) miniature inhibitory post-synaptic current (mIPSC) representative traces (G), mean mIPSC frequency (H), and amplitude (I) in DCN neurons. Symbols indicate recorded cells.

(J) Pharmacological JAK1/2 inhibition during viral déjà vu in WT mice. Ruxolitinib (Rux), AZD1480 (AZD), or vehicle (control) was given via the oral route (po) from day 5 to day 8 after LCMVwt i.v.

(K) Rotarod performance on day 10 after LCMVwt i.v. of the indicated groups.

(legend continued on next page)

CNS neurons. rLCMV is not cytolytic and fails to trigger a clinically significant $CD8^+$ T cell response after neonatal i.c. infection. Accordingly, such rLCMV carrier mice remain clinically healthy, but, when challenged intravenously (i.v.) with wild-type LCMV (LCMVwt) in late adolescence, they mount a potent $CD8^+$ T cell response against the immunodominant H-$2D^b$-restricted nucleoprotein-derived epitope, $NP_{396–404}$. This epitope is shared between rLCMV and LCMVwt, and, as a consequence, LCMVwt-carrier challenged mice develop severe CNS disease that is initiated by $CD8^+$ T cells encountering CNS neurons presenting $NP_{396–404}$ on H-$2D^b$ (Merkler et al., 2006).

The murine viral déjà vu disease model has histopathological features that closely recapitulate those of Rasmussen's encephalitis (RE), a rare but devastating inflammatory disease of the human CNS. This disease, which typically affects children under the age of 15, is characterized by drug-resistant epilepsy and progressive neurological decline (Varadkar et al., 2014). Analogous to the viral déjà vu model, in which $CD8^+$ T cells cluster around rLCMV-infected neurons, RE lesions are dominated by infiltrating $CD8^+$ T cells that show disease-specific clonal expansions (Schneider-Hohendorf et al., 2016) and are found in close proximity to neurons (Varadkar et al., 2014).

Here we utilized the viral déjà vu model to investigate the crosstalk between $CD8^+$ T cells, their target neurons, and phagocytes. We observed that signature elements of this crosstalk mechanism are recapitulated in a cohort of RE patients and correlate with epileptic activity. These findings offer novel grounds for therapeutic intervention in $CD8^+$ T cell-driven encephalitis and related disorders.

RESULTS

Neuronal JAK-STAT1 Signaling Is Essential for $CD8^+$ T Cell-Mediated Synaptic Alterations and Motor Impairment in Viral Déjà Vu Disease

We recently showed that neuronal expression of the IFN-γ receptor (IFNGR) is necessary for viral déjà vu disease (Kreutzfeldt et al., 2013). Here we tested whether signal transducer and activator of transcription 1 (STAT1), a key effector of IFN-γ signaling, represents a disease-relevant pathway in neurons downstream of IFNGR. We infected neonatal *Stat1*$^{+/+}$ or *Stat1*$^{fl/fl}$ mice with rLCMV, which expresses the Cre recombinase (rLCMV-Cre) and persists in CNS neurons (Kreutzfeldt et al., 2013) (referred to as "carrier"; Figure 1A). Viral tropism to neurons (Figure S1A) and viral load in the brain (Figure S1B) were unchanged in rLCMV-Cre carrier *Stat1*$^{fl/fl}$ mice compared with *Stat1*$^{+/+}$ mice. Furthermore, we measured Cre recombinase activity using loxP-flanked red fluorescent protein (RFP) reporter rLCMV-Cre carrier mice (Luche et al., 2007). We counted RFP reporter gene-expressing cells (400–522 RFP^+ cells per brain, n = 3 mice) and found that 93.0% ± 0.7% co-expressed the neuronal marker NeuN, whereas low proportions of RFP-positive cells expressed glial fibrillary acidic protein ($GFAP^+$) (astrocytes, 2.9% ± 0.4%), $Iba1^+$ (microglia, 2.4% ± 0.1%) or $CC1^+$ (oligodendrocytes, 1.5% ± 0.3%) (Figure S1C). In addition, 5-week-old rLCMV-Cre *Stat1*$^{fl/fl}$ carrier mice, non-carrier *Stat1*$^{+/+}$ mice, and carrier *Stat1*$^{+/+}$ mice that were not challenged with LCMVwt i.v. displayed similar rotarod performance and synaptic density in the deep cerebellar nuclei (DCN) (Figures S1D and S1E). Following i.v. challenge with LCMVwt, *Stat1*$^{+/+}$ but not *Stat1*$^{fl/fl}$ rLCMV-Cre carriers developed clinical manifestations of viral déjà vu disease, as measured by the rotarod test (Figure 1B), despite comparable $NP_{396–404}$-specific $CD8^+$ T cell responses in the blood (Figure 1C) and infiltrates in the CNS (Figure 1D). We further confirmed that rLCMV-Cre abrogated the expression of phosphorylated STAT1 (pSTAT1) in LCMVwt-challenged *Stat1*$^{fl/fl}$ carrier mice (Figure 1E), corroborating conditional neuronal deletion of *Stat1* in these mice (Figure S1F).

Based on these findings, we reasoned that neuronal STAT1 signaling may be required for neuronal dysfunction because of synapse loss. We enumerated synapses on neurons of the DCN, which are consistently infiltrated by $CD8^+$ T cells in viral déjà vu (Figure S1G) and belong to an important functional network, receiving the output of the cerebellar cortex through inhibitory projections of the Purkinje cells and projecting to motor nuclei (Figure S1H). $Synaptophysin^+$ (SYP^+) perisomatic boutons (corresponding to presynaptic terminals) densely lined the soma of DCN neurons in healthy non-carrier controls but were significantly reduced in LCMVwt i.v. challenged *Stat1*$^{+/+}$ carrier mice relative to *Stat1*$^{fl/fl}$ carrier mice (Figure 1F). In diseased *Stat1*$^{+/+}$ mice, synapse loss occurred predominantly at inhibitory presynaptic ($GAD65\text{-}67^+$) and postsynaptic ($gephyrin^+$) terminals (Figures S1I and S1J) but not at excitatory ($VGLUT1^+$) presynaptic terminals (Figure S1K). Nevertheless, the density of Purkinje cells projecting to the DCN remained unchanged, rendering anterograde neuro-axonal degeneration an unlikely explanation for the observed loss of inhibitory synaptic input (Figure S1L). To investigate the functional correlates of disturbed synaptic transmission, we performed whole-cell recordings of DCN neurons in acute slices of the inflamed cerebellum from viral déjà vu mice. Individual recordings of DCN neurons revealed a significant reduction in miniature inhibitory postsynaptic current (mIPSC) frequency (Figures 1G and 1H) and amplitude (Figure 1I; Figure S1M) in LCMVwt i.v. challenged *Stat1*$^{+/+}$ but not *Stat1*$^{fl/fl}$ carrier mice. Altogether, these results suggest that compromised inhibitory synaptic transmission in viral déjà vu mice requires neuronal STAT1 signaling, consistent with reduced inhibitory presynaptic and postsynaptic terminals in the DCN.

IFNGR signaling involves the Janus kinases JAK1 and JAK2, which phosphorylate STAT1 and enable its transcription factor activity (Darnell et al., 1994). We thus tested whether pharmacological inhibition of Janus kinases using ruxolitinib (an inhibitor of JAK1/2) or AZD1480 (preferential inhibitor for JAK2) could

(L) Immunostaining for SYP and DAPI; 30 DCN neurons per mouse; scale bar, 10 μm.

Error bars, SEM; ****$p < 0.0001$, ***$p < 0.001$, **$p < 0.01$, *$p < 0.05$; ns, not significant by Kruskal-Wallis test with Dunn's correction for multiple comparisons (A–H) or one-way ANOVA with Fisher's least significant difference (LSD) for multiple comparisons (I). Data are representative of four independent experiments (B, E, F, H, and I) or pooled from two independent experiments (C, D, K, and L). See also Figure S1.

improve viral déjà vu disease in WT mice (Figure 1J). Treatment with either of the inhibitors was started 5 days after LCMVwt i.v. challenge to minimize potential interference with T cell priming in secondary lymphoid organs. Both treatments significantly ameliorated viral déjà vu disease (Figure 1K), which was paralleled by a preservation of synaptic density (Figure 1L) and an almost complete abrogation of neuronal STAT1 phosphorylation (Figure S1N). Importantly, treatment with either ruxolitinib or AZD1480, respectively, did not affect viral tropism in the CNS (Figure S1O) or the viral burden (Figure S1P).

STAT1 Signaling Drives Neuronal Expression of Chemokines and Complement Factors

To investigate how neuronal JAK/STAT1 signaling results in synaptic alterations, we profiled the neuronal translatome by exploiting "RiboTag mice" (*Rpl22*$^{HA/+}$) (Sanz et al., 2009). Upon Cre-mediated recombination of their gene-targeted locus, *Rpl22*$^{HA/+}$ mice express a hemagglutinin (HA)-tagged ribosomal protein, L22, enabling the immunoprecipitation of ribosome-bound RNA. We inoculated neonatal *Rpl22*$^{HA/+}$ mice with rLCMV-Cre, inducing HA-tagged ribosomal expression in infected neurons (Figure 2A).

First we extracted ribosome-bound mRNA from the brains of 5- to 7-week-old *Rpl22*$^{HA+/-}$ carrier mice and performed next-generation RNA sequencing. We compared the transcriptional signatures detected within the translatome of these carrier mice with published single-cell transcriptomic signatures of neurons, microglia, astrocytes, oligodendrocytes, oligodendrocyte precursor cells (OPCs), and endothelial cells (Tasic et al., 2016). We observed a strong enrichment for neuron-specific transcripts in the translatome of rLCMV-Cre carrier *Rpl22*$^{HA/+}$ mice, whereas non-neuronal transcripts were low or absent (Figure S2). Furthermore, the cellular transcriptional signature of rLCMV-Cre carrier *Rpl22*$^{HA/+}$ mice showed a strong overlap with that of crosses between Thy1-Cre mice constitutively expressing the Cre recombinase under a neuron-specific Thy1 promoter (Thy1-Cre; Dewachter et al., 2002) and *Rpl22*$^{HA/+}$ mice (Figure S2A).

Next we compared the neuronal translatome 9 days after challenge with LCMVwt in STAT1-competent (*Rpl22*$^{HA/+}$x*Stat1*$^{+/+}$; developing viral déjà vu disease), conditionally STAT1-deficient (*Rpl22*$^{HA/+}$x*Stat1*$^{fl/fl}$; resistant to viral déjà vu disease), and non-challenged (*Rpl22*$^{HA/+}$x*Stat1*$^{+/+}$) rLCMV-Cre carrier mice (Figure 2A). The three groups clustered separately in multidimensional scaling analyses (Figure 2B). We found 916 differentially upregulated and 118 downregulated transcripts in *Rpl22*$^{HA/+}$x*Stat1*$^{+/+}$ carrier challenged mice relative to *Rpl22*$^{HA/+}$x*Stat1*$^{fl/fl}$ carrier challenged mice (cutoff of 2-fold change; adjusted $p < 0.05$; Tables S1 and S2). We used gene set enrichment analysis (GSEA) with compiled modules from gene ontology to generate the enrichment map network of *Rpl22*$^{HA/+}$x*Stat1*$^{+/+}$ relative to *Rpl22*$^{HA/+}$x*Stat1*$^{fl/fl}$ carrier challenged mice (Figure 2C; Table S3). The network analysis revealed that STAT1-competent mice showed upregulation of highly connected enriched gene sets with roles in immune response and downregulation of gene sets for synaptic activity. In addition, GSEA with Kyoto Encyclopedia of Genes and Genomes (KEGG) pathways revealed signatures of chemokine signaling and antigen processing and presentation as well as of the complement and coagulation cascades, all of which depended on neuronal STAT1 signaling (false discovery rate [FDR] < 0.01, normalized enrichment score [NES] > 1.5; Figures 2D and 2E; Table S4). Among the chemokines induced upon viral déjà vu, we found strong upregulation of the *Ccl2* and *Cxcl10* transcripts (40- and 20-fold relative to non-challenged controls, respectively), which we confirmed by *in situ* hybridization (ISH) (Figures 2F and S2B).

Neuronal STAT1 Signaling Is Required for CNS Phagocyte Apposition and Synaptic Stripping

The differentially expressed chemokines and complement factors in neurons observed above may act as a paracrine signal to modulate phagocytic activity. We thus speculated that STAT1-induced neuronal chemokines or complement factor instructed phagocytes to engulf synapses. Thus, we compared the accumulation and activation of phagocytes in *Stat1*$^{+/+}$ and *Stat1*$^{fl/fl}$ carrier mice upon LCMVwt i.v. challenge. Iba1^{+} phagocyte numbers (Figures 3A and 3B) and cellular size (Figures 3A and 3C) were increased in challenged *Stat1*$^{+/+}$ and *Stat1*$^{fl/fl}$ carriers compared with challenged *Stat1*$^{+/+}$ non-carrier mice, suggesting neuronal STAT1-independent phagocyte activation. Indeed, these Iba1^{+} phagocytes were devoid of the purinergic receptor P2Y12R, which is expressed only on resting microglia (Butovsky et al., 2014; Figure S3A).

However, in contrast to *Stat1*$^{fl/fl}$ carriers, Iba1^{+} phagocytes of diseased *Stat1*$^{+/+}$ mice displayed an ameboid morphology, as evident in increased cellular somata (Figure 3D) and decreased branching complexity of cytoplasmic processes (Figures S3B–S3E). In addition, we found abundant Iba1^{+} phagocytes in close apposition to or even enwrapping rLCMV-Cre infected neurons of diseased *Stat1*$^{+/+}$ mice, whereas such phagocyte behavior was comparably rare in *Stat1*$^{fl/fl}$ carrier mice (Figures 3E and 3F). Moreover, the juxtaposition of phagocytes and neurons was associated with a loss of presynaptic SYP^{+} terminals in *Stat1*$^{+/+}$ but not in *Stat1*$^{fl/fl}$ carriers (Figure 3G). The displacement of synapses by phagocytes (Figure 3H) and the colocalization of engulfed presynaptic terminals with the LAMP1^{+} lysosome compartment inside Iba1^{+} cells (Figure S3F) underpinned these phagocytes' active role in synapse elimination.

A substantial fraction of Iba1^{+} cells in the CNS of *Stat1*$^{+/+}$ mice with viral déjà vu disease lacked the microglia-specific marker TMEM119 (Bennett et al., 2016; Figure S3G), which pointed toward a monocyte-derived origin of these cells. To discriminate CNS-resident from blood-derived phagocytes, we used *Cx3cr1*$^{CreERT2/+}$x*Rosa*26-Stop-*Rfp*$^{fl/+}$ reporter mice (Yona et al., 2013). Tamoxifen treatment of these mice results in persistent RFP expression in microglia, but not blood monocytes, because of their differential turnover rates (Figure 3I; Goldmann et al., 2016). Newborn mice were inoculated i.c. with rLCMV and treated with tamoxifen at 3 weeks of age. Four weeks after the last tamoxifen application, almost all microglia expressed RFP (92.5% ± 1.4% cellular co-staining with Iba1 on histological brain sections), whereas circulating Ly6C^{high} and Ly6C^{low} monocytes were devoid of the reporter labeling (RFP^{+} cells, 0.07% ± 0.03% for Ly6C^{high} and 0.18% ± 0.06% for Ly6C^{low} monocytes in the blood). Viral déjà vu experiments in *Cx3cr1*$^{CreERT2/+}$x*Rosa*26-Stop-*Rfp*$^{fl/+}$

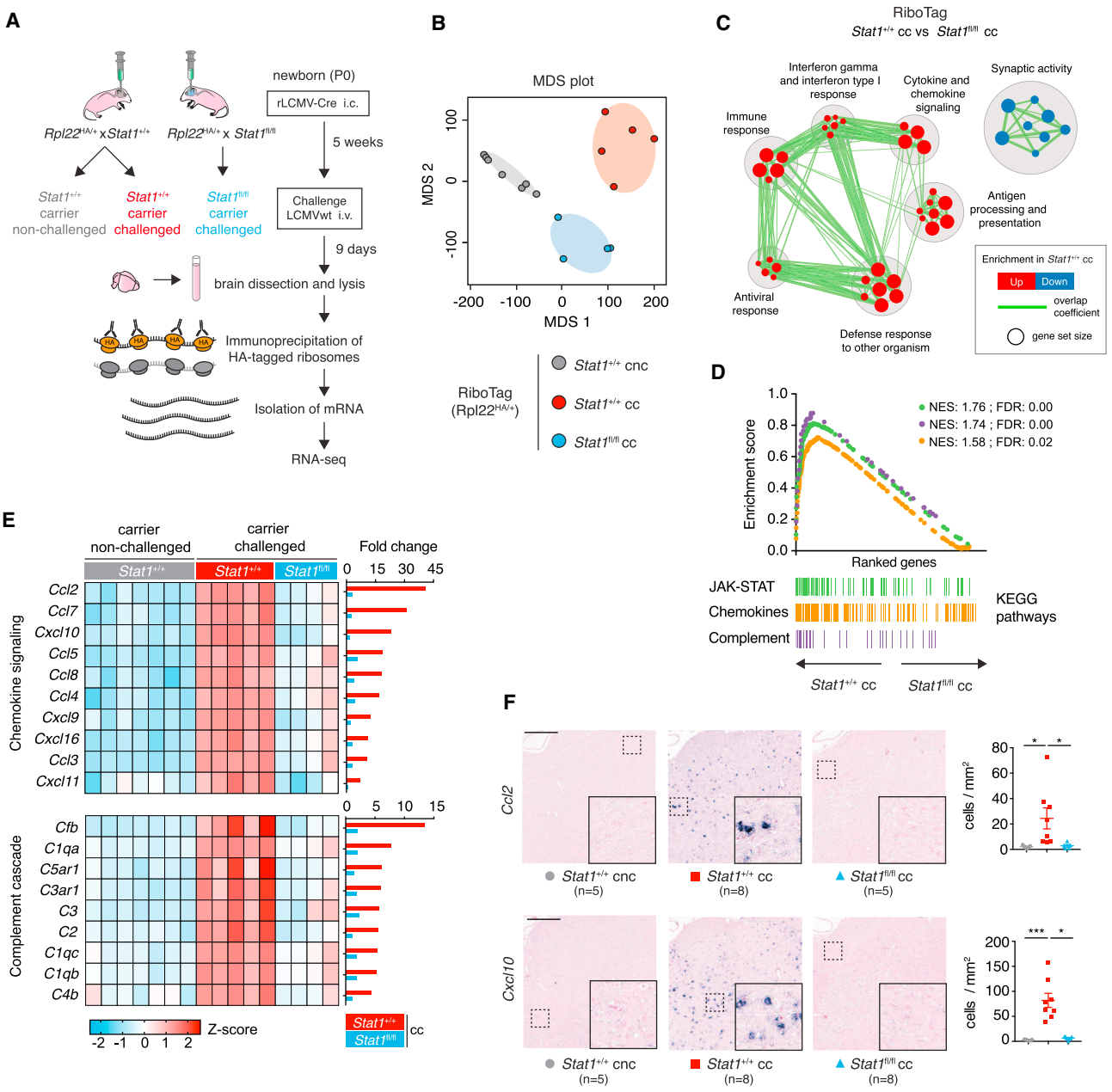

Figure 2. STAT1 Signaling Drives Neuronal Expression of Chemokines and Complement Factors

(A) The translatome of infected neurons of *Rpl22*$^{HA/+}$ rLCMV-Cre carrier mice was analyzed by next-generation RNA sequencing in the viral déjà vu setting (day 9 after LCMVwt i.v.).

(B) Multidimensional scaling (MDS) plot of the neuronal translatome of carrier non-challenged *Rpl22*$^{HA/+}$x*Stat1*$^{+/+}$, and carrier challenged STAT1-competent (*Rpl22*$^{HA/+}$x*Stat1*$^{+/+}$) and conditionally STAT1-deficient (*Rpl22*$^{HA/+}$x*Stat1*$^{fl/fl}$) mice.

(C) Network graph showing enriched GO terms imported to the enrichment map from a gene set enrichment analysis (GSEA) in *Rpl22*$^{HA/+}$x*Stat1*$^{+/+}$ versus *Rpl22*$^{HA/+}$x*Stat1*$^{fl/fl}$ challenged mice. Nodes represent individual gene sets and edges the relatedness between them (minimum overlap is 50%). Upregulated nodes are shown in red and downregulated nodes in blue.

(D) GSEA with KEGG modules of transcripts highly expressed in *Rpl22*$^{HA/+}$x*Stat1*$^{+/+}$ versus *Rpl22*$^{HA/+}$x*Stat1*$^{fl/fl}$ challenged mice. Normalized enrichment score (NES) indicates the cumulative enrichment, and false discovery rate (FDR) indicates the adjusted *q* value. Lines over the distribution of expression profiles mark the occurrence of the signature transcripts.

(E) Heatmaps and fold change of significantly altered transcripts in the chemokine signaling pathway and complement cascade of *Stat1*$^{+/+}$ and *Stat1*$^{fl/fl}$ carrier challenged (cc) mice (compared with *Stat1*$^{+/+}$ carrier non-challenged [cnc]), each column represents individual mice.

(F) *In situ* hybridization (ISH) of *Ccl2* and *Cxcl10* in brain sections of the indicated groups. Scale bars, 250 μm; insets, 125 μm.

Error bars, SEM; ***p < 0.001, *p < 0.05; ns, not significant by Kruskal-Wallis test with Dunn's correction for multiple comparisons. Data pooled from two independent experiments are shown (F). See also Figure S2 and Tables S1, S2, S3, and S4.

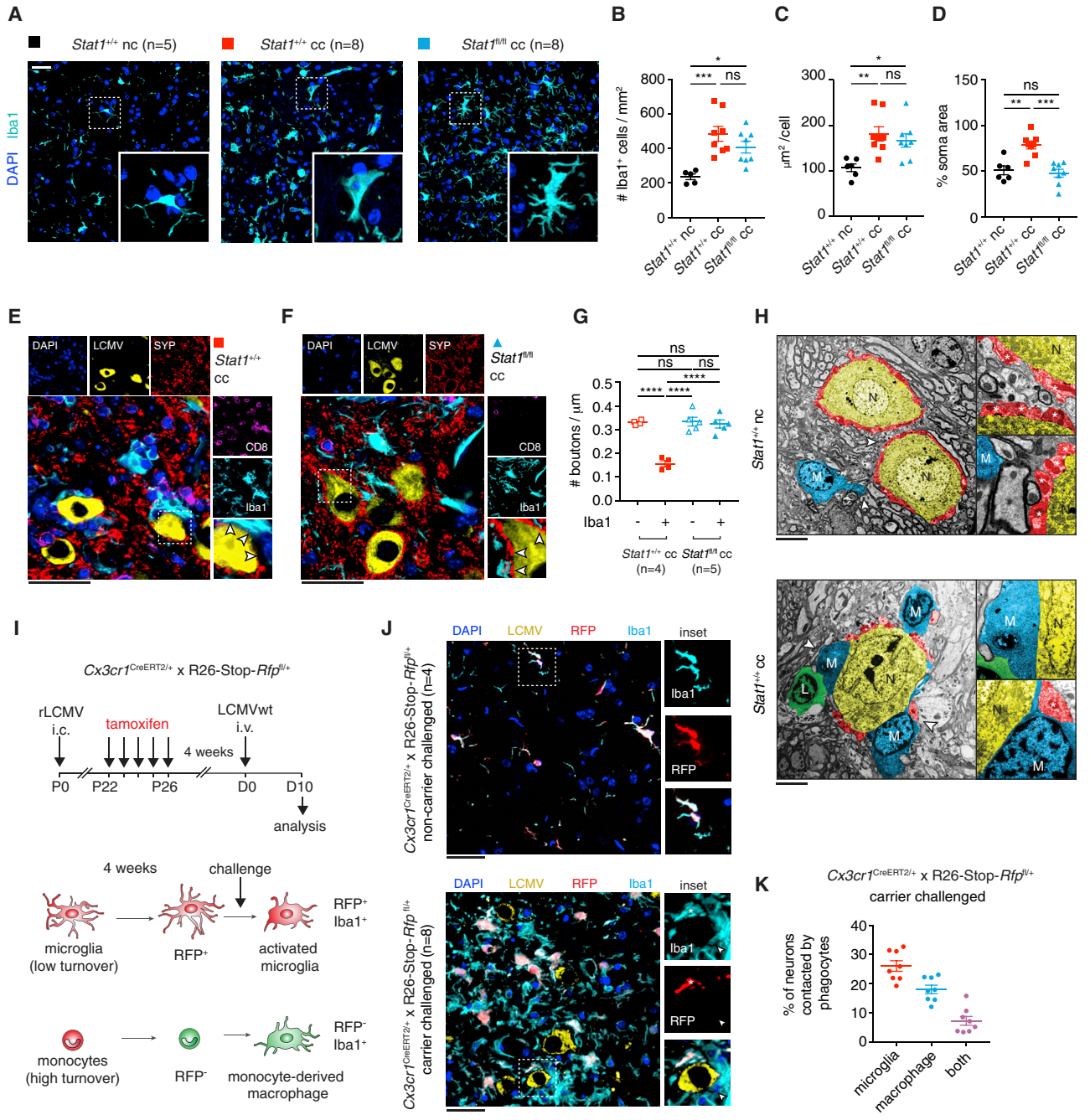

Figure 3. Neuronal STAT1 Signaling Is Required for CNS Phagocyte Recruitment and Synaptic Stripping

(A–H) Experimental setup as described in Figure 1A.

(A) Representative images of Iba1$^+$ phagocytes in DCN of *Stat1*$^{+/+}$ non-carrier challenged (*Stat1*$^{+/+}$ nc), *Stat1*$^{+/+}$ carrier challenged (*Stat1*$^{+/+}$ cc) and *Stat1*$^{fl/fl}$ carrier challenged (*Stat1*$^{fl/fl}$ cc) mice.

(B–D) Quantification of the density (B), size (C), and proportion (D) of somata area of Iba1$^+$ cells. Each symbol represents the average value of a single animal.

(E and F) Representative DCN section of *Stat1*$^{+/+}$ cc (E) and *Stat1*$^{fl/fl}$ cc (F) co-immunostained for LCMV-nucleoprotein (LCMV), synaptophysin (SYP), CD8$^+$ T cells (CD8) and Iba1$^+$ phagocytes (Iba1), and DAPI. Scale bars, 30 µm.

(G) Quantification of perisomatic bouton density of LCMV$^+$ DCN neurons with (+) or without (–) juxtaposed Iba1$^+$ cells. Each symbol represents the average value of a single animal (n = 29 to 60 neurons per mouse).

(H) Electron micrograph showing a region of DCN from challenged *Stat1*$^{+/+}$ nc and *Stat1*$^{+/+}$ cc. In diseased mice, a phagocyte (M, blue) closely apposing part of a neuronal soma (N, yellow) and a lymphocyte (L, green) in close vicinity can be observed. Asterisks (red) indicate axosomatic synapses. Arrowheads indicate regions magnified in the insets. Scale bars, 10 µm.

(legend continued on next page)

reporter mice revealed that both blood-derived phagocytes (Iba1$^+$, RFP$^-$ cells) and microglia (Iba1$^+$, RFP$^+$ cells) were juxtaposed to neurons (Figures 3J and 3K). Neuronal STAT1-dependent apposition of CNS phagocytes could also be detected in the hippocampal formation, resulting in synaptic stripping (Figure S3H) and impairment of inhibitory synaptic transmission of CA1 pyramidal neurons (Figures S3I–S3L).

Neuronal CCL2, but Not Complement C3/C4, Is Essential for Disease and Synaptic Stripping

Our translatome analyses had revealed STAT1-dependent induction of the chemokine CCL2 in neurons (Table S1). CCL2 regulates both the activation and recruitment of phagocytes in the CNS (Carson et al., 2006). To determine the significance of neuronal CCL2 for déjà vu disease, we established neonatal rLCMV-Cre carriers with a loxP-flanked *Ccl2* gene (*Ccl2*$^{fl/fl}$). We administered LCMVwt to rLCMV-Cre *Ccl2*$^{fl/fl}$ carrier mice and found that the absence of neuronal *Ccl2* (Figure S4A) largely protected mice from viral déjà vu disease (Figure 4A). This protection was not due to impaired recruitment of CD8$^+$ T cells into the CNS of CCL2$^{fl/fl}$ mice because the number of NP$_{396–404}$-specific CD8$^+$ T cells in the brain was even slightly increased compared with challenged *Ccl2*$^{+/+}$ carrier mice (Figure 4B). Also, the viral burden and cellular tropism were unaltered in the CNS of *Ccl2*$^{fl/fl}$ carrier mice (Figure S4B). However, *Ccl2*$^{fl/fl}$ carrier mice challenged i.v. with LCMVwt harbored a lower number of Iba1$^+$ cells in the inflamed CNS (Figure S4C), and the residual phagocytes displayed a ramified rather than ameboid phenotype (Figures S4D–S4H), similar to those in *Stat1*$^{fl/fl}$ carrier mice (Figure 3D). Accordingly, the density of presynaptic terminals in DCN neurons was preserved in *Ccl2*$^{fl/fl}$ carrier mice (Figure 4C), even in the ones that were in contact with phagocytes (Figure 4D). Moreover, such phagocyte-neuron contacts in *Ccl2*$^{fl/fl}$ carrier mice comprised a smaller proportion of neuronal perikarya circumference (Figure S4I), and fewer engulfed synaptophysin were detected inside the LAMP1$^+$ lysosomal compartment of Iba1$^+$ phagocytes (Figure S4J). These findings corroborated that neuronal CCL2 is key for phagocyte recruitment, subsequent synapse elimination, and, eventually, viral déjà vu disease.

In our neuronal translatome profiling, we also noted an increased expression of components of the complement cascade, such as *C1qa*, *C2*, and *C3* (Figures 2C–2E). C3 cleavage products can tag synapses and allow for microglia-mediated synaptic stripping (Vasek et al., 2016). To test whether neuronal complement contributed to the observed synaptic pathology and the ensuing viral déjà vu disease, we exploited mice deficient in the central complement components C3 and C4 (*C3C4*$^{-/-}$). *C3C4*$^{-/-}$ mice were not protected from viral déjà vu disease, neither by clinical assessment (Figure 4G) nor at the morphological level when assessing synaptic loss (Figures 4H–4J) and also displayed a similar viral load and neuronal tropism in the CNS (Figure S4K).

Of note, complement component C3 is known to play a role in synaptic pruning during postnatal development (Schafer et al., 2012). We thus compared the synaptic density in the DCN and rotarod performance of non-challenged *C3C4*$^{-/-}$ carrier mice at baseline with controls. However, we did not detect significant alterations in *C3C4*$^{-/-}$ carrier mice at baseline with regard to these evaluated parameters (Figures S4L and S4M). In addition, *C3C4*$^{-/-}$ and *C3C4*$^{+/+}$ carrier challenged mice displayed an unaltered proportion of neurons in contact with phagocytes (Figure S4N) and the same number of phagocytes with engulfed synaptophysin in LAMP1$^+$ compartments (Figure S4O). Altogether, these data show that the complement components C3/C4 are not essential for locomotor impairments and synaptic pathology in viral déjà vu disease.

Pharmacological Inhibition of Phagocyte Activation and Depletion of CCR2$^+$ Monocytes Ameliorate Viral Déjà Vu Disease

Our observations suggested that neurons under CD8$^+$ T cell attack recruited phagocytes, which, in turn, caused synaptic stripping. Hence, we tested whether pharmacological interference with phagocyte activation and/or recruitment offered clinical benefits for viral déjà vu in WT mice. Treatment with minocycline, which suppresses phagocyte activation (Tikka et al., 2001), was initiated 5 days after LCMVwt i.v. challenge (Figure 5A). Minocycline treatment significantly ameliorated viral déjà vu disease (Figure 5B) and prevented synaptic loss (Figure 5C). Iba1$^+$ phagocytes were reduced in numbers in the CNS of minocycline-treated mice (Figure 5D), whereas CD8$^+$ T cell infiltration (Figure 5E) and viral burden in the CNS (Figure S5A) were not affected. To test whether the observed effect of minocycline is due to possible antimicrobial effects rather than suppressed phagocyte activation, we similarly treated a group of mice with the broad-spectrum antibiotic amoxicillin-clavulanate (Brook et al., 2013) in the viral déjà vu setting. However, amoxicillin-clavulanate treatment did not protect mice from disease (Figures S5B and S5C).

In a complementary approach, we depleted CCR2$^+$ Ly6C^{high} monocytes using an anti-CCR2 antibody (MC-21 (Bruttger et al., 2015; Mack et al., 2001; Figure 5F). Treatment with the MC-21 antibody efficiently depleted Ly6C^{high} monocytes from peripheral blood (Figure S5D), as shown previously (Mildner et al., 2009). Further, MC-21 treatment afforded significant protection from viral déjà vu disease (Figure 5G) along with preservation of synaptic density (Figure 5H) and reduced numbers of Iba1$^+$ phagocytes in the CNS (Figures 5I and S5E). Conversely, MC-21 depletion did not reduce brain-infiltrating CD8$^+$ T cell numbers (Figure 5J) or viral burden in the CNS (Figure S5F).

(I) Experimental setup with *Cx3cr1*$^{CreERT2/+}$x*R26(Rosa26)*-Stop-*Rfp*$^{fl/+}$ reporter mice to distinguish between microglia and infiltrating macrophages in the viral déjà vu setting. 4 weeks after tamoxifen-induced Cre-LoxP recombination, microglia are RFP$^+$, whereas circulating monocytes are RFP$^-$.

(J) Representative immunostaining for Iba1$^+$ RFP$^+$ (microglia) and RFP$^-$ cells (blood-derived macrophages) apposing neurons of carrier challenged mice and non-carrier controls.

(K) Quantification of DCN neurons with (+) or without (–) contact to the two subsets of phagocytes.

Error bars, SEM; ****p < 0.0001, ***p < 0.001, **p < 0.01, *p < 0.05, ns, not significant by one-way ANOVA test with Tukey correction for multiple comparisons (B-G). Data are representative of four independent experiments (A–H) or two independent experiments (J and K). See also Figure S3.

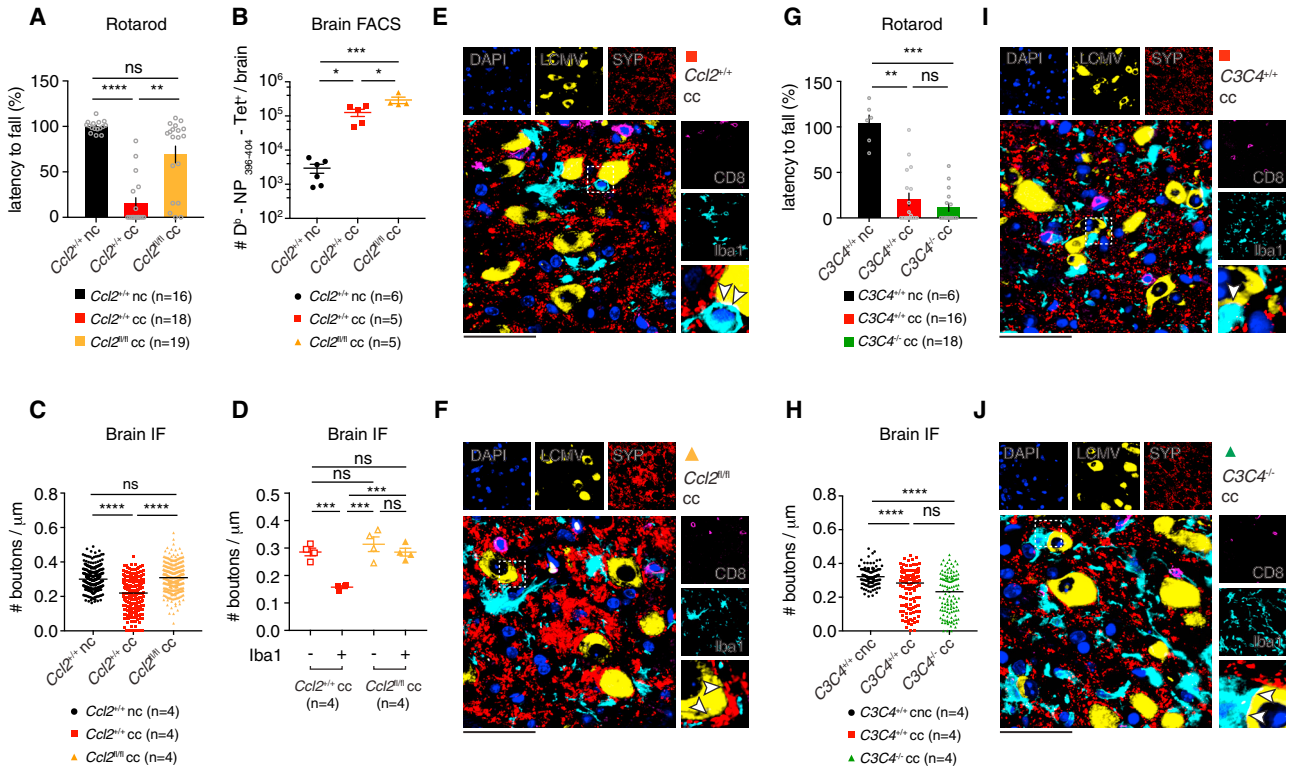

Figure 4. Neuronal CCL2, but Not Complement C3/C4, Is Essential for Disease and Synaptic Stripping

(A–J) Experimental setup as in Figure 1A.

(A) Rotarod performance at the peak of disease (day 10 after challenge) is shown for *Ccl2*$^{+/+}$ and *Ccl2*$^{fl/fl}$ carrier challenged (cc) mice. *Ccl2*$^{+/+}$ non-carrier challenged (*Ccl2*$^{+/+}$ nc) mice served as controls.

(B) Flow cytometric analysis of brain-infiltrating D_b-$NP_{396–404}$ Tet$^+$ CD8$^+$ T cells from the indicated groups.

(C and D) Perisomatic bouton density in DCN of the indicated groups at the peak of disease (C) and in relation to LCMV+ neurons with (+) or without (–) juxtaposed Iba1$^+$ cells (D). Symbols represent individual DCN neurons (29–60 neurons per mouse); lines indicate the median.

(E and F) Representative immunofluorescence co-staining of a DCN section of carrier challenged *Ccl2*$^{+/+}$ cc (E) and *Ccl2*$^{fl/fl}$ cc (F) mice stained for LCMV-nucleoprotein (LCMV), synaptophysin (SYP), CD8$^+$ T cells (CD8) and Iba1$^+$ phagocytes (Iba1), and DAPI.

(G) Rotarod performance at the peak of disease of carrier challenged (cc) *C3C4*$^{+/+}$ and *C3C4*$^{-/-}$ mice. *C3C4*$^{+/+}$ non-carrier challenged mice served as controls.

(H) Perisomatic bouton density was quantified in the DCN region. Symbols indicate individual DCN neurons (29–39 neurons per mouse) and lines indicate the median. For histological analysis, *C3C4*$^{+/+}$ carrier non-challenged (cnc) served as controls.

(I and J) Representative immunofluorescence co-staining of a DCN section of carrier challenged (I) *C3C4*$^{+/+}$ cc and (J) *C3C4*$^{-/-}$ cc animals.

Scale bars, 30 µm; error bars, SEM; ****p < 0.0001, ***p < 0.001, **p < 0.01, *p < 0.05; ns, not significant by Kruskal-Wallis test with Dunn's correction for multiple comparisons (A, C, G, and H) and by one-way ANOVA test with Tukey correction for multiple comparisons (B and D). Data are pooled from two independent experiments (A and G) or representative of two independent experiments (B–D and H–J). See also Figure S4.

Thus, phagocyte inhibition can reduce CD8$^+$ T cell-driven synaptic stripping.

RE Shares Cellular and Molecular Hallmarks with Viral Déjà Vu

To investigate whether our mechanistic findings in the viral déjà vu model might also apply to human disease, we analyzed RE biopsies obtained from 20 patients. We thus investigated whether the cellular and molecular hallmarks of viral déjà vu comprising a spatial association of CD8$^+$ T cells, pSTAT1, CCL2 together with phagocytes and synaptic loss could be found in RE biopsies. To this end, adjacent brain sections were stained for markers of the viral déjà vu signature (CD8, pSTAT1, CCL2, and CD68 for activated phagocytes), and distances between positive signals were used to generate 2D density maps for each marker. In contrast to control tissues of non-neurological diseases (NNDs), we observed high CD8$^+$, pSTAT1$^+$, CCL2$^+$, and CD68$^+$ densities (cluster) in tissue samples from RE patients at similar locations, appearing as white peaks when 2D density maps were stacked and visualized as a 3D surface plot (Figure 6A). Importantly, the number of CD8$^+$ T clusters correlated positively with the number of pSTAT1$^+$ clusters ($p < 0.05$, $R^2 = 0.91$) and CCL2$^+$ clusters ($p < 0.05$, $R^2 = 0.76$), and pSTAT1$^+$ clusters correlated positively with CCL2$^+$ clusters ($p < 0.05$, $R^2 = 0.83$) (Figures 6B–6D), which became particularly evident in cases with a disease duration of less than 3 years prior to surgery (Figure S6A). Neurons were frequently found in contact with CD68$^+$ phagocytes (Figures 6E–6G) and displayed a reduced density of axosomatic synaptic terminals in RE biopsies compared with age- and area-matched regions of NND (Figures 6H and 6I). Similar to

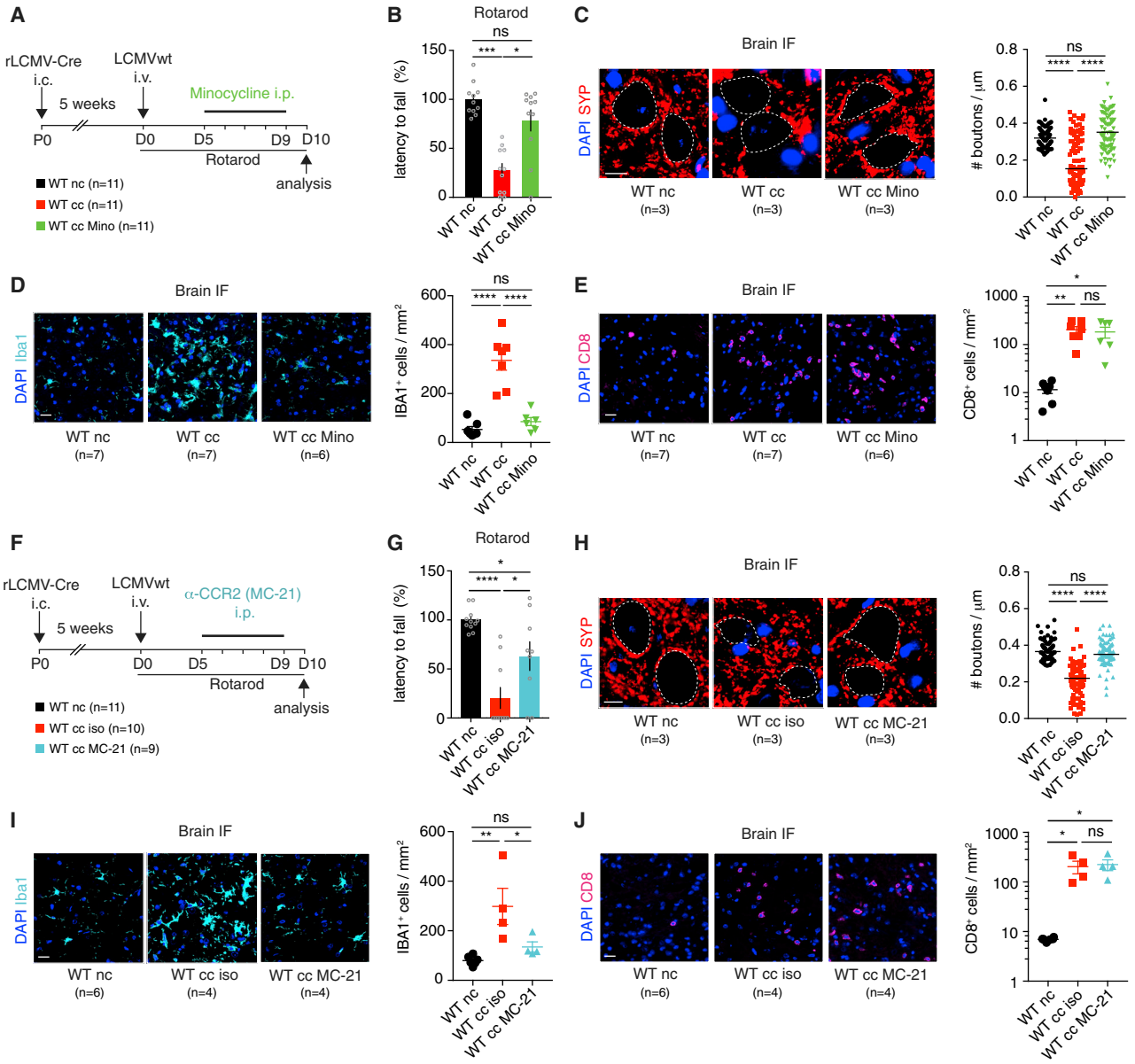

Figure 5. Pharmacological Depletion or Inhibition of CNS Phagocytes Ameliorates Viral Déjà Vu

(A) Experimental setup for administration of minocycline (mino, intraperitoneally [i.p.] every 24 hr) or PBS during viral déjà vu in wild-type (WT) mice.

(B) Rotarod performance at the peak of disease (day 10).

(C) Representative immunostaining of synaptophysin (SYP) of the indicated groups. Perisomatic bouton density was quantified in DCN regions (n = 30 neurons per mouse). Lines indicate the median. Scale bar, 10 µm.

(D and E) Representative immunofluorescence images and quantification of Iba1$^+$ phagocytes (D) and CD8$^+$ T cells (E) in DCN. Scale bars, 20 µm.

(F) Experimental setup for administration of α-CCR2 antibody (MC-21, i.p. every 24 hr) or isotype (iso) administration during viral déjà vu.

(G) Rotarod motor performance at the peak of disease of the indicated groups.

(H) Representative immunofluorescence images of synaptophysin (SYP) in a DCN section of the indicated groups. Perisomatic bouton density was quantified in DCN regions (n = 30 neurons per mouse). Lines indicate the median. Scale bar, 10 µm.

(I and J) Representative immunofluorescence images and quantification of Iba1$^+$ phagocytes (I) and CD8$^+$ T cells (J) in DCN. Scale bars, 20 µm.

Error bars, SEM; ****$p < 0.0001$, ***$p < 0.001$, **$p < 0.01$, *$p < 0.05$; ns, not significant by Kruskal-Wallis test with Dunn's correction for multiple comparisons (C) and by one-way ANOVA test with Tukey correction for multiple comparisons (G). See also Figure S5.

mice with viral déjà vu disease, the neuronal juxtaposition with phagocytes correlated with decreased synaptic densities in RE biopsies ($p < 0.0001$, $R^2 = 0.65$) (Figures 6J and 6K).

RE patients commonly suffer from *epilepsia partialis continua* (EPC) (Table S5), a drug-resistant focal motor *status epilepticus* with prolonged and regular jerking activity (Varadkar et al., 2014).

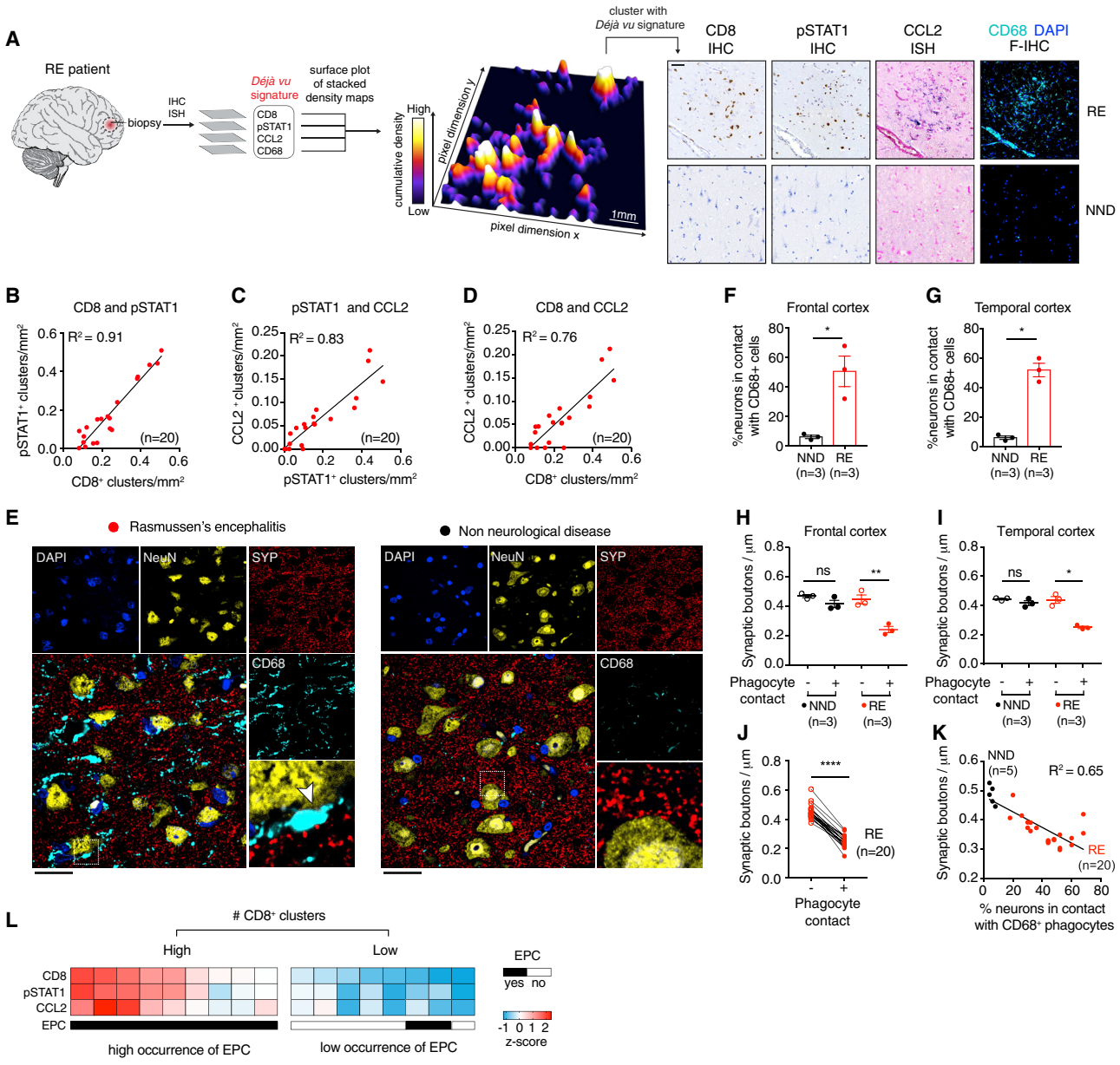

Figure 6. CD8⁺ T Cell Clusters in RE Correlate with pSTAT1 and CCL2 Expression and with Phagocyte-Associated Synaptic Loss and Predict Epileptic Activity

(A) Adjacent brain sections of a representative RE biopsy stained for CD8, pSTAT1 (IHC), or CCL2 (ISH) or CD68 and DAPI by fluorescence immunohistochemistry staining (F-IHC) and digitally aligned for coregistration. Positive cells for each marker were detected, and 2D signal density maps were generated. Individual 2D maps were stacked and visualized as a 3D surface plot. White peaks correspond to regions enriched in all markers. Scale bar, 1mm in surface plot and 50 µm in IHC and ISH.

(B–D) Correlations between (B) CD8⁺ and pSTAT1⁺ clusters, (C) pSTAT1⁺ and CCL2⁺ clusters, and (D) CD8⁺ and CCL2⁺ clusters in RE brain sections. Symbols represent individual RE patients.

(E) Representative images of RE and non-neurological disease (NND) co-immunostained for neurons (NeuN), synaptophysin (SYP), activated phagocytes (CD68), and DAPI. The inset on the left shows a phagocytic process interposed between neuronal somata and synaptic terminals (arrowhead). Scale bars, 20 µm.

(F and G) Quantification of the proportion of neurons in contact with CD68⁺ phagocytes in RE compared with age- and area-matched frontal (F) and temporal (G) NND.

(H and I) Quantification of perisomatic bouton density in RE and NND matched for age, frontal (H) and temporal (I) brain region (n = 40 neurons evaluated per patient) and stratified according to the presence (+) or absence (–) of contact with CD68⁺ cells.

(J and K) Comparison of perisomatic bouton density (J) in RE patients with (+) or without (–) phagocyte contact and (K) correlation with phagocyte apposition in RE and NND. Symbols represent individual patients (n = 40 neurons evaluated per patient).

(legend continued on next page)

To identify histological and clinical parameters in RE biopsies that identify patients with EPC, we used a classification and regression tree (CART) analysis. The CART model revealed that a high number of $CD8^+$ T cell clusters (>0.21/mm^2) was significantly associated with a more frequent occurrence of EPC (Figure 6L; t test values > 0.21 versus < 0.21; EPC, $p < 0.008237$; CD8, $p < 0.001282$).

To investigate whether the aforementioned pSTAT1-CCL2 signature can also be observed in other forms of human encephalitis involving $CD8^+$ T cell brain infiltration (Figures S6B, S6D, and S6F), we performed a similar analysis in small cohorts of viral encephalitis (herpes simplex virus encephalitis, n = 5, and group D adenovirus encephalitis, n = 1) and limbic encephalitis (n = 8) (Table S6). The latter comprises a group of autoimmune diseases in which both cellular and humoral adaptive immune responses against neuronal antigens are reported to be implicated in the pathogenesis (Dalmau and Graus, 2018). In all investigated cases of viral encephalitis, we found $pSTAT1^+$ cells, some of which could be assigned to neurons (Figures S6B and S6G), as well as clusters of CCL2 expression (Figures S6B and S6H) and $CD68^+$ phagocytes (Figures S6B and S6I). In addition, we found neuronal juxtaposition of $CD68^+$ phagocytes that was associated with synaptic loss (Figures S6C and S6J). In the studied limbic encephalitis cases, 3 out of 8 cases showed pSTAT1 positive neurons (Pattern 2, Figure S6D). In these 3, but not in the remaining 5 cases (pattern 1), we observed increased neuronal contact with phagocytes (Figure S6I), associated with synaptic loss (Figure S6J). Altogether, these data support that human disease conditions and viral déjà vu display similar signatures associated with synaptic alterations.

DISCUSSION

Our study of CNS inflammation establishes that neurons are not mere targets of $CD8^+$ T cells but assume an essential active role as intermediaries between $CD8^+$ T cells and phagocytes. Specifically, neurons orchestrated their own synaptic stripping by phagocytes through JAK1/2-STAT1 signaling and, in turn, CCL2 expression.

Phagocytes play a pivotal role in assuring correct synaptic connectivity in the developing and adult brain (Paolicelli et al., 2011) but also contribute to synapse pathology in inflammatory (Bialas et al., 2017) and neurodegenerative (Krasemann et al., 2017) CNS disorders. Several lines of evidence suggest that complement C3 is key for synapse removal by phagocytes under neuroinflammatory conditions. For instance, a recent study in the context of viral CNS infection reported a central role for the complement component C3 in the elimination of excitatory $VGLUT1^+$ presynaptic terminals by microglia (Vasek et al., 2016). Accordingly, we found upregulated expression of complement components C3 and C4 in neurons that occurred in a STAT1-dependent manner. However, C3 and C4 were not essential for disease precipitation or for synaptic removal in the viral déjà vu setting, which involves both inhibitory presynaptic and postsynaptic terminals.

Instead, our data reveal a novel mechanism that operates when $CD8^+$ T cells attack neurons *in vivo*. Animals lacking either STAT1 or CCL2 in neurons were largely protected from disease and synapse loss. Therefore, neuronally expressed CCL2 represented an essential step in the communication between neurons and phagocytes. CCL2 promoted the juxtaposition of phagocytes to neurons, which was necessary for synaptic engulfment and displacement. However, whether synaptic phagocytosis and displacement represent staggered sequences of the same process or can occur independent of each other needs further clarification.

Our study suggests that phagocytosis could be triggered by complement components other than C3 (Hong et al., 2016) or by complement-independent mechanisms (Datwani et al., 2009). Indeed, pathological exposure of the phospholipid phosphatidylserine or de-sialylated glycoprotein to the extracellular leaflet of the neuronal surfaces (Brown and Neher, 2014) can evoke phagocytosis via various phagocytic receptors, including triggering receptor expressed on myeloid cells 2 (TREM2) (Krasemann et al., 2017), which can function independently to complement tagging of neurons. It is thus conceivable that, depending on the pathophysiological context, mutually non-exclusive mechanisms contribute to synapse pathology in inflammatory CNS conditions. Furthermore, although total phagocytic contacts with neurons were similar in diseased $C3/C4^{-/-}$ and $C3/C4^{+/+}$ mice, a potential change in the ratio of microglia/macrophage in diseased $C3/C4^{-/-}$ mice cannot be excluded.

The present data emphasize that blood-derived $CCR2^+$ inflammatory monocytes are actively involved in the disease, resulting from $CD8^+$ T cell-neuron interactions. Accordingly, antibody-mediated depletion of $CCR2^+$ monocytes from the circulation ameliorated viral déjà vu disease, which is in line with previous reports attributing an important role to these cells in $CD8^+$T cell-mediated CNS disease (Fife et al., 2000). Besides blood-derived monocytes, brain-resident microglia also displayed engulfed synapses and may contribute to the immunopathogenesis of viral déjà vu disease, but this was not directly addressed in our study.

The patients in our RE cohort exhibited similar hallmarks in brain biopsies as mice with viral déjà vu disease. pSTAT1 and CCL2 expression in $CD8^+$ T cell "hotspots" render it likely that an analogous mechanism may operate in humans. The pSTAT1 signature was most evident in patients with shorter disease duration before surgery (less than 3 years), regardless of the brain region analyzed. This could indicate that the observed mechanism plays a role especially in early stages of RE pathology (Pardo et al., 2004) and, thus, could offer a time window for possible therapeutic interventions. Likewise, as postulated for limbic encephalitis (Dalmau and Graus, 2018), heterogeneity in the pathophysiology underlying RE disease cannot be excluded, which may equally contribute to the noted inter-individual variability

(L) Classification and regression tree (CART) analysis revealed that elevated numbers of $CD8^+$ clusters (>0.21 clusters/mm^2) predicted a higher occurrence of *epilepsia partialis continua* (EPC) in RE patients. Symbols represent individual patients.

Error bars, SEM; $^{**}p < 0.01$, $^{*}p < 0.05$; ns, not significant by paired t test (F, G, and J) and one-way ANOVA with Sidak correction for multiple comparisons (H and I). See also Figure S6 and Tables S5 and S6.

of $CD8^+$ T cell infiltrate density and corresponding pSTAT1-CCL2 signature. IFN-γ signature genes along with phagocyte activation are also observed in a variety of neuroinflammatory conditions, such as multiple sclerosis (Khaibullin et al., 2017) or HIV-associated neurocognitive disorders (Schrier et al., 2015), rendering our findings of potential significance to several diseases beyond RE. This is also supported by our observation that the pSTAT1-CCL2 signature was equally observed in a small cohort of herpes simplex encephalitis and in a subset of limbic encephalitis specimens (pattern 2). One may furthermore speculate that $CD8^+$ T cells, which constitute the majority of lymphocytic infiltrates in multiple sclerosis lesions (Hauser et al., 1986), could contribute, through a similar mechanism, to the synaptic alterations associated with the disease (Albert et al., 2017).

Neuronal synapse removal by phagocytes can obviously be detrimental to the organism, as evident in viral and autoimmune disorders of the CNS. This raises the question of its evolutionary benefit. We speculate that the isolation of antigenic neurons from their synaptic networks may allow $CD8^+$ T cells to limit retrograde *trans*-synaptic viral spread (Koyuncu et al., 2013), thus containing a viral infection while avoiding irreversible neuronal loss (Binder and Griffin, 2001). Alterations of synapses are potentially reversible (Marzo et al., 2016), opening opportunities for non-cytolytic viral clearance and later re-integration of the preserved neurons into signaling circuits.

STAT1 signaling and phagocyte recruitment, as crucial events in neuronal stripping, offer opportunities for pharmacological interventions. Minocycline may be beneficial in preventing synaptic stripping through interference with phagocyte activation (Tikka et al., 2001), although off-target effects on vessels, apoptosis, and cell proliferation have been described (Garrido-Mesa et al., 2013). Nevertheless, drugs such as minocycline and small molecular inhibitors of JAKs (e.g., ruxolitinib and AZD1480) can pass the blood-brain barrier and have been approved by the United States Food and Drug Administration (FDA) for other purposes (O'Shea et al., 2015), making them attractive candidates for exploratory clinical trials.

In summary, our study demonstrates that neurons instruct phagocytes to remove synaptic terminals upon $CD8^+$ T cell attack, opening up novel strategies for pharmacological interventions in RE and other T cell-mediated CNS diseases.

STAR★METHODS

Detailed methods are provided in the online version of this paper and include the following:

- KEY RESOURCES TABLE
- CONTACT FOR REAGENT AND RESOURCE SHARING
- EXPERIMENTAL MODEL AND SUBJECT DETAILS
  - Mice
  - Human brain samples
- METHODS DETAILS
  - Virus infection
  - *Viral déjà vu* setup
  - Tamoxifen treatment
  - Pharmacological interventions
  - Antibody treatment for $CCR2^+$ monocyte depletion
  - Rotarod
  - Flow cytometry
  - Histology
  - Antibodies
  - Analysis of phagocyte morphology
  - Quantification of synaptic terminals in the deep cerebellar nuclei
  - Quantification of synaptic terminals in the hippocampal CA1 region
  - Quantification of phagocyte engulfing synaptic terminals
  - Electron microscopy
  - Electrophysiology
  - *In situ* hybridization
  - RNAscope *in situ* hybridization
  - RiboTag-purification
  - RNA-seq analysis
  - CART analysis
- QUANTIFICATION AND STATISTICAL ANALYSIS
- DATA AND SOFTWARE AVAILABILITY
  - Software
  - Data Resources

SUPPLEMENTAL INFORMATION

Supplemental Information includes six figures and six tables and can be found with this article online at https://doi.org/10.1016/j.cell.2018.07.049.

ACKNOWLEDGMENTS

This work was supported by the Gebert-Rüf Foundation (GRS-049/13 to D.M.). D.M. and D.D.P. are supported by the Klaus-Tschira Foundation and Swiss National Science Foundation. D.M. and N.P. are supported by the Swiss MS Society. D.M. is supported by the Helmut Horten Foundation. M.P. is supported by the BMBF-funded Competence Network of Multiple Sclerosis (KKNMS), the Sobek-Stiftung, the DFG (SFB 992, SFB1160, SFB/TRR167, and Reinhart-Koselleck grant), and the Ministry of Science, Research and the Arts, Baden-Wuerttemberg (Sonderlinie "Neuroinflammation"). We acknowledge Philippe Henchoz for EM. We thank Angela Andersen (Life Science Editors) for her support in manuscript editing.

AUTHOR CONTRIBUTIONS

G.D.L. generated most of the data along with S.P. M.K. performed part of the image analysis. N.P., K.S., B.K., and I.V. performed part of the flow cytometry analysis. K.E. did part of the histological analysis. S.M. and C.B. performed electrophysiological recordings. R.C. and I.B. participated in human brain analysis. T.L. and G.S. performed RNA sequencing analysis. N.L.-M. performed *in situ* hybridization. I.W. performed part of the immunostainings. O.S. contributed to human sample evaluation. M.J.C.J. was involved in MC-21 antibody depletion experiments. M.M. provided the MC-21 antibody. M.P. and D.D.P. participated in discussions of the results. G.D.L., D.D.P., and D.M. wrote the manuscript. D.M. designed and supervised the study.

DECLARATION OF INTERESTS

The authors declare no competing interests.

Received: March 2, 2018
Revised: June 11, 2018
Accepted: July 30, 2018
Published: August 30, 2018

REFERENCES

Albert, M., Barrantes-Freer, A., Lohrberg, M., Antel, J.P., Prineas, J.W., Palkovits, M., Wolff, J.R., Brück, W., and Stadelmann, C. (2017). Synaptic pathology in the cerebellar dentate nucleus in chronic multiple sclerosis. Brain Pathol. *27*, 737–747.

Bennett, M.L., Bennett, F.C., Liddelow, S.A., Ajami, B., Zamanian, J.L., Fernhoff, N.B., Mulinyawe, S.B., Bohlen, C.J., Adil, A., Tucker, A., et al. (2016). New tools for studying microglia in the mouse and human CNS. Proc. Natl. Acad. Sci. USA *113*, E1738–E1746.

Bernard-Valnet, R., Yshii, L., Quériault, C., Nguyen, X.H., Arthaud, S., Rodrigues, M., Canivet, A., Morel, A.L., Matthys, A., Bauer, J., et al. (2016). CD8 T cell-mediated killing of orexinergic neurons induces a narcolepsy-like phenotype in mice. Proc. Natl. Acad. Sci. USA *113*, 10956–10961.

Bialas, A.R., Presumey, J., Das, A., van der Poel, C.E., Lapchak, P.H., Mesin, L., Victora, G., Tsokos, G.C., Mawrin, C., Herbst, R., and Carroll, M.C. (2017). Microglia-dependent synapse loss in type I interferon-mediated lupus. Nature *546*, 539–543.

Bien, C.G., Vincent, A., Barnett, M.H., Becker, A.J., Blumcke, I., Graus, F., Jellinger, K.A., Reuss, D.E., Ribalta, T., Schlegel, J., et al. (2012). Immunopathology of autoantibody-associated encephalitides: clues for pathogenesis. Brain *135*, 1622–1638.

Binder, G.K., and Griffin, D.E. (2001). Interferon-gamma-mediated site-specific clearance of alphavirus from CNS neurons. Science *293*, 303–306.

Brook, I., Wexler, H.M., and Goldstein, E.J. (2013). Antianaerobic antimicrobials: spectrum and susceptibility testing. Clin. Microbiol. Rev. *26*, 526–546.

Brown, G.C., and Neher, J.J. (2014). Microglial phagocytosis of live neurons. Nat. Rev. Neurosci. *15*, 209–216.

Bruttger, J., Karram, K., Wörtge, S., Regen, T., Marini, F., Hoppmann, N., Klein, M., Blank, T., Yona, S., Wolf, Y., et al. (2015). Genetic Cell Ablation Reveals Clusters of Local Self-Renewing Microglia in the Mammalian Central Nervous System. Immunity *43*, 92–106.

Butovsky, O., Jedrychowski, M.P., Moore, C.S., Cialic, R., Lanser, A.J., Gabriely, G., Koeglsperger, T., Dake, B., Wu, P.M., Doykan, C.E., et al. (2014). Identification of a unique TGF-β-dependent molecular and functional signature in microglia. Nat. Neurosci. *17*, 131–143.

Carson, M.J., Doose, J.M., Melchior, B., Schmid, C.D., and Ploix, C.C. (2006). CNS immune privilege: hiding in plain sight. Immunol. Rev. *213*, 48–65.

Chevalier, G., Suberbielle, E., Monnet, C., Duplan, V., Martin-Blondel, G., Farrugia, F., Le Masson, G., Liblau, R., and Gonzalez-Dunia, D. (2011). Neurons are MHC class I-dependent targets for CD8 T cells upon neurotropic viral infection. PLoS Pathog. *7*, e1002393.

Dalmau, J., and Graus, F. (2018). Antibody-Mediated Encephalitis. N. Engl. J. Med. *378*, 840–851.

Darnell, J.E., Jr., Kerr, I.M., and Stark, G.R. (1994). Jak-STAT pathways and transcriptional activation in response to IFNs and other extracellular signaling proteins. Science *264*, 1415–1421.

Datwani, A., McConnell, M.J., Kanold, P.O., Micheva, K.D., Busse, B., Shamloo, M., Smith, S.J., and Shatz, C.J. (2009). Classical MHCI molecules regulate retinogeniculate refinement and limit ocular dominance plasticity. Neuron *64*, 463–470.

Dewachter, I., Reversé, D., Caluwaerts, N., Ris, L., Kuipéri, C., Van den Haute, C., Spittaels, K., Umans, L., Serneels, L., Thiry, E., et al. (2002). Neuronal deficiency of presenilin 1 inhibits amyloid plaque formation and corrects hippocampal long-term potentiation but not a cognitive defect of amyloid precursor protein [V717I] transgenic mice. J. Neurosci. *22*, 3445–3453.

Fife, B.T., Huffnagle, G.B., Kuziel, W.A., and Karpus, W.J. (2000). CC chemokine receptor 2 is critical for induction of experimental autoimmune encephalomyelitis. J. Exp. Med. *192*, 899–905.

Garrido-Mesa, N., Zarzuelo, A., and Gálvez, J. (2013). Minocycline: far beyond an antibiotic. Br. J. Pharmacol. *169*, 337–352.

Gendusa, R., Scalia, C.R., Buscone, S., and Cattoretti, G. (2014). Elution of High-affinity (>10-9 KD) Antibodies from Tissue Sections: Clues to the Molecular Mechanism and Use in Sequential Immunostaining. J. Histochem. Cytochem. *62*, 519–531.

Goldmann, T., Wieghofer, P., Jordão, M.J., Prutek, F., Hagemeyer, N., Frenzel, K., Amann, L., Staszewski, O., Kierdorf, K., Krueger, M., et al. (2016). Origin, fate and dynamics of macrophages at central nervous system interfaces. Nat. Immunol. *17*, 797–805.

Hauser, S.L., Bhan, A.K., Gilles, F., Kemp, M., Kerr, C., and Weiner, H.L. (1986). Immunohistochemical analysis of the cellular infiltrate in multiple sclerosis lesions. Ann. Neurol. *19*, 578–587.

Hong, S., Beja-Glasser, V.F., Nfonoyim, B.M., Frouin, A., Li, S., Ramakrishnan, S., Merry, K.M., Shi, Q., Rosenthal, A., Barres, B.A., et al. (2016). Complement and microglia mediate early synapse loss in Alzheimer mouse models. Science *352*, 712–716.

Kallert, S.M., Darbre, S., Bonilla, W.V., Kreutzfeldt, M., Page, N., Müller, P., Kreuzaler, M., Lu, M., Favre, S., Kreppel, F., et al. (2017). Replicating viral vector platform exploits alarmin signals for potent $CD8^+$ T cell-mediated tumour immunotherapy. Nat. Commun. *8*, 15327.

Khaibullin, T., Ivanova, V., Martynova, E., Cherepnev, G., Khabirov, F., Granatov, E., Rizvanov, A., and Khaiboullina, S. (2017). Elevated Levels of Proinflammatory Cytokines in Cerebrospinal Fluid of Multiple Sclerosis Patients. Front. Immunol. *8*, 531.

Kim, J.V., Kang, S.S., Dustin, M.L., and McGavern, D.B. (2009). Myelomonocytic cell recruitment causes fatal CNS vascular injury during acute viral meningitis. Nature *457*, 191–195.

Kim, K.W., Vallon-Eberhard, A., Zigmond, E., Farache, J., Shezen, E., Shakhar, G., Ludwig, A., Lira, S.A., and Jung, S. (2011). In vivo structure/function and expression analysis of the CX3C chemokine fractalkine. Blood *118*, e156–e167.

Klein, R.S., and Hunter, C.A. (2017). Protective and Pathological Immunity during Central Nervous System Infections. Immunity *46*, 891–909.

Koyuncu, O.O., Hogue, I.B., and Enquist, L.W. (2013). Virus infections in the nervous system. Cell Host Microbe *13*, 379–393.

Krasemann, S., Madore, C., Cialic, R., Baufeld, C., Calcagno, N., El Fatimy, R., Beckers, L., O'Loughlin, E., Xu, Y., Fanek, Z., et al. (2017). The TREM2-APOE Pathway Drives the Transcriptional Phenotype of Dysfunctional Microglia in Neurodegenerative Diseases. Immunity *47*, 566–581.e9.

Kreutzfeldt, M., Bergthaler, A., Fernandez, M., Brück, W., Steinbach, K., Vorm, M., Coras, R., Blümcke, I., Bonilla, W.V., Fleige, A., et al. (2013). Neuroprotective intervention by interferon-γ blockade prevents CD8+ T cell-mediated dendrite and synapse loss. J. Exp. Med. *210*, 2087–2103.

Liblau, R.S., Gonzalez-Dunia, D., Wiendl, H., and Zipp, F. (2013). Neurons as targets for T cells in the nervous system. Trends Neurosci. *36*, 315–324.

Luche, H., Weber, O., Nageswara Rao, T., Blum, C., and Fehling, H.J. (2007). Faithful activation of an extra-bright red fluorescent protein in "knock-in" Cre-reporter mice ideally suited for lineage tracing studies. Eur. J. Immunol. *37*, 43–53.

Mack, M., Cihak, J., Simonis, C., Luckow, B., Proudfoot, A.E., Plachý, J., Brühl, H., Frink, M., Anders, H.J., Vielhauer, V., et al. (2001). Expression and characterization of the chemokine receptors CCR2 and CCR5 in mice. J. Immunol. *166*, 4697–4704.

Marzo, A., Galli, S., Lopes, D., McLeod, F., Podpolny, M., Segovia-Roldan, M., Ciani, L., Purro, S., Cacucci, F., Gibb, A., and Salinas, P.C. (2016). Reversal of Synapse Degeneration by Restoring Wnt Signaling in the Adult Hippocampus. Curr. Biol. *26*, 2551–2561.

Medana, I., Martinic, M.A., Wekerle, H., and Neumann, H. (2001). Transection of major histocompatibility complex class I-induced neurites by cytotoxic T lymphocytes. Am. J. Pathol. *159*, 809–815.

Merkler, D., Horvath, E., Bruck, W., Zinkernagel, R.M., Del la Torre, J.C., and Pinschewer, D.D. (2006). "Viral déjà vu" elicits organ-specific immune disease independent of reactivity to self. J. Clin. Invest. *116*, 1254–1263.

Mildner, A., Mack, M., Schmidt, H., Brück, W., Djukic, M., Zabel, M.D., Hille, A., Priller, J., and Prinz, M. (2009). CCR2+Ly-6Chi monocytes are crucial for the

effector phase of autoimmunity in the central nervous system. Brain *132*, 2487–2500.

O'Shea, J.J., Schwartz, D.M., Villarino, A.V., Gadina, M., McInnes, I.B., and Laurence, A. (2015). The JAK-STAT pathway: impact on human disease and therapeutic intervention. Annu. Rev. Med. *66*, 311–328.

Paolicelli, R.C., Bolasco, G., Pagani, F., Maggi, L., Scianni, M., Panzanelli, P., Giustetto, M., Ferreira, T.A., Guiducci, E., Dumas, L., et al. (2011). Synaptic pruning by microglia is necessary for normal brain development. Science *333*, 1456–1458.

Pardo, C.A., Vining, E.P., Guo, L., Skolasky, R.L., Carson, B.S., and Freeman, J.M. (2004). The pathology of Rasmussen syndrome: stages of cortical involvement and neuropathological studies in 45 hemispherectomies. Epilepsia *45*, 516–526.

Prinz, M., Erny, D., and Hagemeyer, N. (2017). Ontogeny and homeostasis of CNS myeloid cells. Nat. Immunol. *18*, 385–392.

R Development Core Team (2017). R: A Language and Environment for Statistical Computing (R Foundation for Statistical Computing).

Sanz, E., Yang, L., Su, T., Morris, D.R., McKnight, G.S., and Amieux, P.S. (2009). Cell-type-specific isolation of ribosome-associated mRNA from complex tissues. Proc. Natl. Acad. Sci. USA *106*, 13939–13944.

Schafer, D.P., Lehrman, E.K., Kautzman, A.G., Koyama, R., Mardinly, A.R., Yamasaki, R., Ransohoff, R.M., Greenberg, M.E., Barres, B.A., and Stevens, B. (2012). Microglia sculpt postnatal neural circuits in an activity and complement-dependent manner. Neuron *74*, 691–705.

Schneider-Hohendorf, T., Mohan, H., Bien, C.G., Breuer, J., Becker, A., Görlich, D., Kuhlmann, T., Widman, G., Herich, S., Elpers, C., et al. (2016). CD8(+) T-cell pathogenicity in Rasmussen encephalitis elucidated by large-scale T-cell receptor sequencing. Nat. Commun. *7*, 11153.

Schrier, R.D., Hong, S., Crescini, M., Ellis, R., Pérez-Santiago, J., Spina, C., and Letendre, S.; HNRP Group (2015). Cerebrospinal fluid (CSF) CD8+ T-cells that express interferon-gamma contribute to HIV associated neurocognitive disorders (HAND). PLoS ONE *10*, e0116526.

Shi, C., Jia, T., Mendez-Ferrer, S., Hohl, T.M., Serbina, N.V., Lipuma, L., Leiner, I., Li, M.O., Frenette, P.S., and Pamer, E.G. (2011). Bone marrow mesenchymal stem and progenitor cells induce monocyte emigration in response to circulating toll-like receptor ligands. Immunity *34*, 590–601.

Tasic, B., Menon, V., Nguyen, T.N., Kim, T.K., Jarsky, T., Yao, Z., Levi, B., Gray, L.T., Sorensen, S.A., Dolbeare, T., et al. (2016). Adult mouse cortical cell taxonomy revealed by single cell transcriptomics. Nat. Neurosci. *19*, 335–346.

Tikka, T., Fiebich, B.L., Goldsteins, G., Keinanen, R., and Koistinaho, J. (2001). Minocycline, a tetracycline derivative, is neuroprotective against excitotoxicity by inhibiting activation and proliferation of microglia. J. Neurosci. *21*, 2580–2588.

Varadkar, S., Bien, C.G., Kruse, C.A., Jensen, F.E., Bauer, J., Pardo, C.A., Vincent, A., Mathern, G.W., and Cross, J.H. (2014). Rasmussen's encephalitis: clinical features, pathobiology, and treatment advances. Lancet Neurol. *13*, 195–205.

Vasek, M.J., Garber, C., Dorsey, D., Durrant, D.M., Bollman, B., Soung, A., Yu, J., Perez-Torres, C., Frouin, A., Wilton, D.K., et al. (2016). A complement-microglial axis drives synapse loss during virus-induced memory impairment. Nature *534*, 538–543.

Vezzani, A., French, J., Bartfai, T., and Baram, T.Z. (2011). The role of inflammation in epilepsy. Nat. Rev. Neurol. *7*, 31–40.

Wallner, B., Leitner, N.R., Vielnascher, R.M., Kernbauer, E., Kolbe, T., Karaghiosoff, M., Rülicke, T., Decker, T., and Müller, M. (2012). Generation of mice with a conditional Stat1 null allele. Transgenic Res. *21*, 217–224.

Wessels, M.R., Butko, P., Ma, M., Warren, H.B., Lage, A.L., and Carroll, M.C. (1995). Studies of group B streptococcal infection in mice deficient in complement component C3 or C4 demonstrate an essential role for complement in both innate and acquired immunity. Proc. Natl. Acad. Sci. USA *92*, 11490–11494.

Yona, S., Kim, K.W., Wolf, Y., Mildner, A., Varol, D., Breker, M., Strauss-Ayali, D., Viukov, S., Guilliams, M., Misharin, A., et al. (2013). Fate mapping reveals origins and dynamics of monocytes and tissue macrophages under homeostasis. Immunity *38*, 79–91.

STAR★METHODS

KEY RESOURCES TABLE

REAGENT or RESOURCE	SOURCE	IDENTIFIER
Antibodies		
mouse anti-APC (clone CC-1)	Millipore	Cat# OP80; RRID: AB_2057371
mouse anti-calbindin D28K (clone D-4)	Santa Cruz Biotechnology	Cat# sc-365360; RRID: AB_10841576
mouse anti-CD68 (clone PG-M1)	DAKO	Cat# M0876; RRID: AB_2074844
rat anti-CD8 (clone 4SM15)	Invitrogen	Cat# 14-0808-80; RRID: AB_2572860
rat anti-CD8 (clone YTS169)	Invitrogen	Cat# MA1-82375; RRID: AB_2075774
rat anti-F4/80 (clone A3-1)	Bio-Rad	Cat# MCA497RT; RRID: AB_1102558
mouse anti-GAD65-67 (clone C-9)	Santa Cruz Biotechnology	Cat# sc-365180; RRID: AB_10710523
mouse anti-gephyrin (clone G-6)	Santa Cruz Biotechnology	Cat# sc-25311; RRID: AB_627670
Chicken anti-GFAP (polyclonal)	Abcam	Cat# ab4674; RRID: AB_304558
rabbit anti-Iba1(polyclonal)	WAKO	Cat# 019-19741; RRID: AB_839504
rat anti-LAMP1 (clone 1D4B)	Santa Cruz Biotechnology	Cat# sc-19992; RRID: AB_2134495
rabbit anti-LCMV NP (sera)	generated by prime- boost immunization against purified LCMV-NP	N/A
rat anti-LCMV NP (sera)	generated by prime- boost immunization against purified LCMV-NP	N/A
rabbit anti-NeuN (clone EPR12763)	Abcam	Cat# ab190195; RRID: AB_2716282
rabbit anti-P2Y12R (polyclonal)	Sigma-Aldrich	Cat# HPA014518; RRID: AB_2669027
rabbit anti–pSTAT1 (clone 58D6)	Cell Signaling Technology	Cat# 9167; RRID: AB_561284
rabbit anti-RFP (polyclonal)	Abcam	Cat# ab124754; RRID: AB_10971665
mouse anti-synaptophysin (clone 27G12)	Novocastra	Cat# NCL-L- SYNAP-299; RRID: AB_564017
rabbit anti-TMEM119 (clone 28-3)	Abcam	Cat# ab209064; RRID: AB_2728083
mouse anti-VGLUT1 (clone A-8)	Santa Cruz Biotechnology	Cat# sc-377425; RRID: AB_2687960
anti-mouse Dylight-488	Jackson ImmunoResearch Laboratories	Cat# 715-485-151; RRID: AB_2341099
anti-rabbit AlexaFluor 555	Thermofisher	Cat# A31572; RRID: AB_162543
anti-mouse Atto 647	LifeSpan Biosciences	Cat# LS- C209483; RRID: AB_2736984
Anti-chicken AlexaFluor 647	Thermofisher	Cat# A21449; RRID: AB_1500594
anti-rat Cy3	Jackson ImmunoResearch Laboratories	Cat# 712-165-153; RRID: AB_2340667
anti-mouse AlexaFluor 555	Thermofisher	Cat# A21127; RRID: AB_2535769
AlexaFluor 647 Antibody Labeling Kit	Thermofisher	Cat# A20186
rat anti-CD8a (clone 53–6.7)	eBioscience	Cat# 11-0081-85; RRID: AB_464916
rat anti-CD11b (M1/70)	eBioscience	Cat# 17-0112-81; RRID: AB_469342
rat anti-CD45 (30-F11)	Biolegend	Cat# 103126; RRID: AB_493535
rat anti-CD45R/B220 (RA3-6B2)	Biolegend	Cat# 103236; RRID: AB_893354
rat anti-CD115 (AFS98)	Biolegend	Cat# 135506; RRID: AB_1937253
rat anti-Ly6C (HK1.4)	Biolegend	Cat# 128036; RRID: AB_2562353
rat anti-Ly6G (1A8)	Biolegend	Cat#127622; RRID: AB_10643269

(*Continued on next page*)

Continued

REAGENT or RESOURCE	SOURCE	IDENTIFIER
mouse anti-NK1.1 (PK136)	Biolegend	Cat# 108730; RRID: AB_2291262
rat anti-CCR2 (SA203G11)	Biolegend	Cat# 150609; RRID: AB_2616981
D^b-$NP_{396-404}$-tetramer	NIH tetramer core facility	N/A
rat anti-CCR2 (MC-21)	provided by Matthias Mack	N/A
rat IgG2b isotype control	Bioxcell	Cat# BE0090; RRID: AB_1107780
Alkaline Phosphatase-labeled antidigoxigenin antibody	Roche	Cat# 11093274910; RRID: AB_514497
Bacterial and Virus Strains		
LCMVwt (Armstrong)	(Kallert et al., 2017)	N/A
rLCMV-Cre	(Kreutzfeldt et al., 2013)	N/A
rLCMV/INDG	(Merkler et al., 2006)	N/A
Biological Samples		
Brain autopsies/biopsies of Rasmussen's encephalitis, Limbic encephalitis, viral encephalitis, Non-neurological disease (NND)	Department of Neuropathology, Universitätsklinikum Erlangen; Institute of Neuropathology, University of Freiburg; Division of Clinical Pathology, University Hospital of Geneva	N/A
Chemicals, Peptides, and Recombinant Proteins		
DAPI	Molecular Probes	Cat# D1306
Collagenase A	Roche	Cat# 11088793001
DNaseI	Roche	Cat# 10104159001
Tamoxifen	Sigma	Cat# T5648
Minocycline	Sigma	Cat# M2280000
Amoxicillin trihydrate: potassium Clavulanate (4:1)	Sigma	Cat# SMB00607-1G
Solutol	Sigma	Cat# 70142-34-6
Ruxolitinib	Selleck chemicals	Cat# S1378
AZD1480	Selleck chemicals	Cat# S2162
Critical Commercial Assays		
AccuCheck Counting Beads	Molecular Probes	Cat# PCB100
Tyramide signal amplification (TSA) 555	Thermofisher	Cat# B40955
Tyramide signal amplification (TSA) 647	Thermofisher	Cat# B40958
anti-mouse DAKO EnVision system HRP	DAKO	Cat# K4001
anti-rabbit DAKO EnVision system HRP	DAKO	Cat# K4003
Alexa Fluor 647 Antibody Labeling Kit	Thermofisher	Cat# A20186
Fixation buffer	Biolegend	Cat# 420801
RNeasy Plus Mini Kit	QIAGEN	Cat# 74034
TruSeq Stranded Total RNA Library Prep Kit with Ribo-Zero Gold	Illumina	Cat# RS-122-2301, RS-122-2302, and RS-122-2303
mouse anti-HA.11 Ascites	Covance	Cat# MMS-101R
RNAscope Fluorescent Multiplex Kit V2	Advanced Cell Diagnostics	Cat# 323100
Dynabeads protein G-Magnetic	Invitrogen	Cat# 100.03D, 100.04D
BD FACS Lysing Solution (BD)	BD	Cat# 349202
Percoll	GE Healthcare	Cat# 17-0891-01
Zombie NIR Fixable Viability Kit	Biolegend	Cat# 423105

(*Continued on next page*)

Continued

REAGENT or RESOURCE	SOURCE	IDENTIFIER
RNAlater stabilization solution	Thermofisher	Cat# AM7020
Tissue Lyser II	QIAGEN	Cat# 85300
TRIzol reagent	Thermofisher	Cat# 15596026
RNeasy plus Micro Kit	QIAGEN	Cat# 74034
RiboHybe hybridization buffer (from kit RiboMap)	Ventana Medical Systems	Cat# 760-102
RiboWash	Ventana Medical Systems	Cat# 760-105
RiboFix reagent (from kit RiboMap)	Ventana Medical Systems	Cat# 760-102
BlueMap NBT/BCIP substrate kit	Ventana Medical Systems	Cat# 760-120
Nuclear red dye	Ventana Medical Systems	Cat# 780-2218
Aquatex	Merck	Cat# 108562
Protease 1 Reagent	Ventana Medical Systems	Cat# 760-2018
Deposited Data		
RNA-seq from neuronal STAT1-compentent and STAT1-deficient Ribotag mice in viral déjà vu	This paper	GEO: GSE110593
Adult Mouse Cortical Cell Taxonomy by Single Cell Transcriptomics	Tasic et al., 2016	GEO: GSE71585
Experimental Models: Organisms/Strains		
Mouse: C57BL/6J	Charles River	Stock# 000664
Mouse: *Ccl2*$^{fl/fl}$	Jackson Laboratories	Stock# 016849
Mouse: *C3C4*$^{-/-}$	Swiss Immunological Mutant Mouse Repository	N/A
Mouse: *Rosa26*-Stop-*Rfp*	Swiss Immunological Mutant Mouse Repository	N/A
Mouse: *Stat1*$^{fl/fl}$	provided by M. Müller (University of Veterinary Medicine Vienna, Austria)	N/A
Mouse: *Cx3cr1*^{CreERT2}	Jackson Laboratories	Stock# 020940
Mouse: *Rpl22*$^{HA/HA}$	Jackson Laboratories	Stock# 011029
Oligonucleotides		
for human *CCL2*, forward 5′CCGTAATACGACTCACTATAGGGAAAGTCTCT GCCGCCCTTC3′	Microsynth	N/A
for human *CCL2*, reverse 5′CCGATTTAGGTGACACTATAGAATCGGAGTTT GGGTTTGCTTG3′	Microsynth	N/A
for mouse *Ccl2,* forward 5′CCGTAATACGACTCACTATAGGGCAGGTGTC CCAAAGAAGCTG3′	Microsynth	N/A
for mouse *Ccl2,* reverse 5′CCGATTTAGGTGACACTATAGAATGGATTCAC AGAGAGGGAAAA-3′	Microsynth	N/A
for mouse *Cxcl10,* forward 5′CCGTAATACGACTCACTATAGGGAGAGACAT CCCGAGCCAAC3′	Microsynth	N/A

(*Continued on next page*)

Continued

REAGENT or RESOURCE	SOURCE	IDENTIFIER
for mouse *Cxcl10,* reverse 5′CCGATTTAGGTGACACTATAGAAGAGGCTCT CTGCTGTCCATC3′	Microsynth	N/A
Mouse *Ccl2* probe channel 1	Advanced Cell Diagnostics	Cat# 311791
Mouse *Rbfox3* probe channel 2	Advanced Cell Diagnostics	Cat# 313311-C2
Human *Ccl2* probe channel 1	Advanced Cell Diagnostics	Cat# 423811
Recombinant DNA		
3′UTR-VSVGP-IGR-Cre-5′UTR-PolI (pDM019), for rLCMV-Cre	(Kreutzfeldt et al., 2013)	N/A
polI-CRE-IGR-NP (pDP083), for rLCMV-Cre and rLCMV/INDG	(Kreutzfeldt et al., 2013)	N/A
polI-CRE-IGR-GP (pDM003), for rLCMV/INDG	(Merkler et al., 2006)	N/A
Software and Algorithms		
Imaris 5.7.2 x64	Bitplane	N/A
Definiens Developer 2.5	Definiens	N/A
FlowJo 10.2	TreeStar	N/A
R language and environment for statistical computing and graphics	https://www.r-project.org	N/A
STAR (version 2.3.0e)	https://github.com/alexdobin/STAR/blob/master/CHANGES.md	N/A
SAMtools	http://samtools.sourceforge.net	N/A
HTSeq	http://htseq.readthedocs.io/en/release_0.10.0/	N/A
Bioconductor and packages	https://www.bioconductor.org	N/A
Gene set enrichment analysis (GSEA) Desktop application v2.2.1	https://software.broadinstitute.org/gsea/index.jsp	N/A
Enrichment Map plugin	http://www.baderlab.org/Software/EnrichmentMap	N/A
Cytoscape version 3.6.0	http://www.cytoscape.org/	N/A
MiniAnalysis 6	Synaptosoft	N/A
FIJI	https://fiji.sc/	N/A
FastQC software	http://www.bioinformatics.babraham.ac.uk/projects/fastqc/	N/A
CASAVA (version 1.8.2)	http://emea.support.illumina.com/downloads/casava_software_version_18_user_guide_(15011196_b).html?langsel=/ch/	N/A
DESeq2 package (version 1.8)	https://bioconductor.org/packages/release/bioc/html/DESeq2.html	N/A
biomaRt package (version 2.24.0)	https://www.bioconductor.org/packages/devel/bioc/html/biomaRt.html	N/A
Pannoramic Viewer software	3DHistech https://www.3dhistech.com/pannoramic_viewer	N/A

CONTACT FOR REAGENT AND RESOURCE SHARING

Further information and requests for reagents may be directed to, and will be fulfilled by the corresponding author Doron Merkler (doron.merkler@unige.ch).

EXPERIMENTAL MODEL AND SUBJECT DETAILS

Mice

Male and female sex-matched newborn mice (P0) were used for intracerebral infection or left uninfected as non-carrier controls. Subsequently, mice between five weeks and ten weeks were used for all the experiments and analyses.

C57BL/6J, *Ccl2*$^{fl/fl}$ (Shi et al., 2011), *Cx3cr1*^{CreERT2} (Kim et al., 2011) and *Rpl22*$^{HA/HA}$ (Sanz et al., 2009) mice were obtained from Jackson Laboratories. *C3C4*$^{-/-}$ (Wessels et al., 1995) and *Rosa26*-Stop-*Rfp*$^{fl/fl}$ (Luche et al., 2007) were obtained from Swiss Immunological Mutant Mouse Repository. *Stat1*$^{fl/fl}$ (Wallner et al., 2012) were kindly provided by M. Müller (University of Veterinary Medicine Vienna, Austria). Animals were housed under specific-pathogen-free condition in individually ventilated cage units. Mice were not involved in previous procedures and were drug or test naive at the beginning of each experiment. Cage bottoms were covered with autoclaved bedding and nesting material for enrichment. Mice were fed irradiated food and drink from autoclaved bottles. All mice were randomly assigned to control or experimental groups at the beginning of each experiment. All animal experimental protocols were performed at the Universities of Geneva with authorization by the responsible Cantonal authority and in accordance with the Swiss law for animal protection.

Human brain samples

All tissue samples were examined by at least two independent board-certified specialists in neuropathology who confirmed the diagnosis. Brain biopsies/autopsies from patients with Rasmussen's encephalitis (RE) (n = 20, 8 males and 12 females, [9.0 ± 8.5 years, mean ± SD]), Limbic encephalitis (LE) (n = 8, 2 males and 6 females, [43.8 ± 17.3 years, mean ± SD]), viral encephalitis (VE) (n = 6, 1 male and 5 females, [48.2 ± 25.3 years, mean ± SD]) and non-neurological disease (NND) (n = 6, 3 males and 3 females, [20.3 ± 14.2 years, mean ± SD]) were obtained from the collection of the Department of Neuropathology at the Universitätsklinikum Erlangen, Universitätsklinikum Freiburg, and Hopîtaux Universitaires de Genève (HUG). Their use for scientific purposes was in accordance with institutional ethical guidelines and was approved by the local ethics committee. Within samples of a study group (RE, LE, VE, NND), no statistical differences between sex were observed with regard to the obtained results. No information about pharmacological treatment prior surgical resection of brain specimens are available for RE, LE, VE.

METHODS DETAILS

Virus infection

Recombinant LCMV strains were generated according to established methods (Kallert et al., 2017; Kreutzfeldt et al., 2013). The following virus strains were used: recombinant LCMV encoding for the glycoprotein of vesicular stomatitis virus (VSV) instead of its own glycoprotein (rLCMV/ INDG, abbreviated rLCMV throughout); rLCMV encoding for Cre recombinase (rLCMV-Cre); LCMVwt (Armstrong strain).

Viral déjà vu setup

Neonatal C57BL/6J (WT), *Stat1*$^{fl/fl}$, *Ccl2*$^{fl/fl}$ and *C3C4*$^{-/-}$ were infected with rLCMV-Cre i.c. (10^4 pfu) to establish a viral carrier status in neurons as described previously (Merkler et al., 2006). Control groups of littermate controls were left uninfected at birth. For newborn *Cx3cr1*$^{creERT2/+}$: *Rosa26*-Stop-*Rfp*$^{fl/+}$, rLCMV i.c. was used. Juvenile mice (> 5 weeks) were challenged with LCMVwt i.v. (10^5 pfu).

Tamoxifen treatment

To induce gene recombination in *Cx3cr1*$^{CreERT2/+}$: *Rosa26*-Stop-*Rfp*$^{fl/+}$, Tamoxifen (Sigma T5648) was dissolved in filter-sterilized corn oil to make solution of 10 mg/ml. The solution was protected from light and placed on a roller mixer to be dissolved over night at 37°C. It was administrated via intraperitoneal injection (i.p.) once every 24 h for 5 consecutive days. The injection dose was determined by weight, using approximately 75 mg tamoxifen/kg body weight. For juvenile mice, a standard dose of 100 μL tamoxifen/corn oil solution was effective to induce Cre recombinase activity.

Pharmacological interventions

To inhibit JAK activity, virus carrier mice were randomized to receive twice daily oral gavage administration of Ruxolitinib (30 mg/kg, Selleck chemicals) or AZD1480 (50 mg/kg, Selleck chemicals) dissolved in Solutol® (Sigma), water and ethanol solution (3:6:1), or a Solutol® solution only starting on day 5 after LCMVwt challenge.

To inhibit phagocyte activation, virus carrier mice received daily intraperitoneal (i.p.) injection of minocycline (50 mg/kg) or PBS (control) starting on day 5 after LCMVwt challenge.

To investigate a potential impact of antibiotics on the *viral déjà vu* disease phenotype, carrier mice were randomized to receive daily oral administration of the broad spectrum antibiotic Amoxicillin-Clavulanate (Amoxicillin trihydrate: potassium Clavulanate (4:1), 50mg/ml, Sigma, catalog number SMB00607-1G in the drinking water) or mock (non-supplemented drinking water) starting on day 5 after LCMVwt challenge.

Antibody treatment for CCR2$^+$ monocyte depletion

For ablation of CCR2$^+$ monocytes, carrier challenged mice were treated with CCR2 mAb (clone: MC-21; 20 μg/ml), i.p. every 24 hours starting on day 5 after challenge, while carrier challenged controls received isotype rat IgG2b.

Rotarod

The ability of motor coordination and balance of mice was monitored with the rotarod test. In this assay, a mouse is placed on a rotating rod that gradually increases its speed of rotation. Thus, the locomotor performance as measured by the time the animal stays on the rotating rod (latency to fall) reflects the maximum rotation speed of the rod up to which the animal can stay in balance. Specifically, mice were placed on a rotating rod (Rotarod 7650; Ugo Basile Biological Research Apparatus) constantly accelerating from 4 to 40 rounds per minute for a maximum of 180 s. Animals were habituated and trained to the rotarod daily from day −3 to day 0 (challenge with LCMVwt), as well on days 3, 5, and 7–10. Endurance time was monitored, and the two best runs out of three at each time point were averaged for analysis. Displayed values (% latency to fall) are relative to the mean of healthy non-carrier controls on disease peak (day 9-10).

Flow cytometry

For staining, the following antibodies were used: anti-CD8a (53–6.7), anti-CD11b (M1/70), anti-CD45 (30-F11), anti-CD45R/B220 (RA3-6B2), anti-CD115 (AFS98), anti-Ly6C (HK1.4), anti-Ly6G (1A8), anti-NK1.1 (PK136), anti-CCR2 (SA203G11). For detection of virus-specific CD8$^+$ T cells, D^b-$NP_{396-404}$-tetramer (NIH tetramer core facility) were used. Peripheral blood samples were collected in FACS-Buffer (10% FCS, 10 mM EDTA, and 0.01% NaN_3 in PBS). Peripheral blood erythrocytes were lysed using BD FACS lysing solution (BD). For the preparation of brain leukocytes, mice were anesthetized and transcardially perfused with PBS. Brains were minced, digested with Collagenase/DNaseI (Roche), and homogenized using 70-μm cell strainers (BD). Leukocytes were separated using a discontinuous Percoll gradient (30% / 70%). Surface staining was performed with directly labeled antibodies and tetramers in FACS buffer. Isolated CD8$^+$ T cell numbers were quantified using AccuCheck Counting Beads (Invitrogen). Dead cells were excluded from the analysis using Zombie NIR Fixable Viability kit (BioLegend). Flow cytometric samples were acquired on a Gallios cytometer (Beckman-Coulter) equipped with three lasers (blue, 488 nm; red, 633 nm; and violet, 405 nm) using appropriate filter sets and compensation controls. Gates were assigned according to appropriate control populations. Analysis was performed with FlowJo software (Treestar, Version X).

Histology

CNS tissue was either fixed with 4% paraformaldehyde (PFA) or in HOPE fixative (DCS Innovative) and was embedded in paraffin as described previously (Kreutzfeldt et al., 2013). For immunohistochemical bright field staining, endogenous peroxidases (PBS/3% H_2O_2) were neutralized and unspecific binding blocked (PBS/10% FCS). After antigen retrieval, PFA-fixed sections were stained with primary antibodies. Bound primary antibodies were visualized either by an avidin-biotin technique with 3,3′-diaminobenzidine (DAB) as chromogen (all reagents from Dako; hemalaun counterstaining of nuclei).

For immunofluorescence staining, after antigen retrieval and unspecific binding blocking, PFA-fixed sections were incubated with primary antibodies. Bound antibodies were visualized with appropriate species-specific Cy2-, Cy3-, or Cy5-conjugated secondary antibodies or anti–rabbit tyramide signal amplification (TSA). Nuclei were stained with DAPI (Invitrogen). Immunostained sections were scanned using Pannoramic 250 FLASH II (3DHISTECH) Digital Slide Scanner with objective magnification of 20 × or 40 × . To perform multiple rounds of immunostaining on a single routine section of deep cerebellar nuclei, an elution method using 2-ME/SDS buffer was used as previously described (Gendusa et al., 2014). Images obtained from multiple immunostainings are then scanned and digitally aligned using Adobe Photoshop CC. Positive signals were quantified by a blinded experimenter using Pannoramic Viewer software (3DHISTECH) and FIJI (NIH Image analysis), or with a custom-made script, which was based on Cognition Network Language (Definiens Cognition Network Technology; Definiens Developer XD software). To analyze the distribution patterns of CD8, pSTAT1, CD68 and CCL2 in the human RE biopsy, we used an image analysis ruleset based on the Definiens Cognition Network Language as previously described (Kreutzfeldt et al., 2013). 2D-signal density maps were stacked and visualized as 3D-surface plot (FIJI plugin). For quantification, clusters were defined as groups of more than ten (for CD8 and pSTAT1, IHC) or five (for CCL2, ISH) positive cells in a 40 × field of view (0.304 mm^2). For representative images, white balance was adjusted and contrast was linearly enhanced using the tools levels, curves, brightness, and contrast in Adobe Photoshop CC. Non-specific background staining in neurons was digitally subtracted with a control staining when appropriate. Image processing was applied uniformly across all images within a given dataset.

Antibodies

Primary antibodies: mouse anti-APC (also known as CC1, clone CC-1, 1:100, Millipore, catalog number OP80), mouse anti-calbindin D28K (D-4:1:500, Santa Cruz Biotechnology catalog number sc-365360), mouse anti-CD68 (clone PG-M1, 1:100, DAKO catalog number M0876), rat anti-CD8 (clone 4SM15, 1:500, Invitrogen catalog number 14-0808-80), rat anti-CD8 (clone YTS169, 1:2000, Invitrogen catalog number MA1-82375, for HOPE tissue), rat anti-F4/80 (clone A3-1, 1:100, Bio-Rad catalog number MCA497RT), mouse anti-GAD65-67 (clone C-9, 1:100, Santa Cruz Biotechnology catalog number sc-365180), mouse anti-gephyrin (clone G-6, 1:100, Santa Cruz Biotechnology catalog number sc-25311), chicken anti-GFAP (polyclonal, 1:2000, Abcam, catalog number

ab4674), rabbit anti-Iba1 (polyclonal, 1:50, WAKO catalog number 019-19741, directly labeled with anti-rabbit Alexafluor 647), rat anti-LAMP1 (clone 1D4B, 1:250, Santa Cruz Biotechnology catalog number sc-19992), rabbit anti-LCMV NP sera (1:4000, generated by prime-boost immunization against purified LCMV-NP), rat anti-LCMV NP sera (1:1000, generated by prime-boost immunization against purified LCMV-NP), rabbit anti-NeuN (clone EPR12763, Abcam ab190195, directly labeled with Alexafluor 488), rabbit anti-P2Y12R (polyclonal, 1:1000, Sigma-Aldrich catalog number HPA014518), rabbit anti–pSTAT1 (clone 58D6; Cell Signaling Technology catalog number 9167), rabbit anti-RFP (polyclonal, 1:400, Abcam catalog number ab124754), mouse anti-synaptophysin (clone 27G12,1:50, Novocastra catalog number NCL-L-SYNAP-299), rabbit anti-TMEM119 (clone 28-3, 1:300, Abcam catalog number ab209064), mouse anti-VGLUT1 (clone A-8, 1:100, Santa Cruz Biotechnology catalog number sc-377425).

Secondary antibodies: anti-mouse Dylight-488 (Jackson ImmunoResearch Laboratories catalog number 715-485-151), anti-rabbit Alexafluor 555 (Thermofisher catalog number A31572), anti-mouse Atto 647 (LifeSpan Biosciences, LS-C209483) anti-rat Cy3 (Jackson ImmunoResearch Laboratories, 712-165-153), anti-mouse AlexaFluor 555 (Thermofisher catalog number A21127), anti-chicken AlexaFluor 647 (Thermofisher catalog number A21449), Alexa Fluor 647 Antibody Labeling Kit (Thermofisher catalog number A20186), anti–rabbit tyramide signal amplification (TSA) 555 (Thermofisher catalog number B40955, with anti-rabbit DAKO EnVision system HRP, catalog number K4003, used to amplify the signals of anti-RFP and anti-TMEM119), anti–mouse tyramide signal amplification (TSA) 647 (Thermofisher catalog number B40958, with anti-mouse DAKO EnVision system HRP, catalog number K4001, used to amplify the signals of anti-CC1;). Secondary antibodies were used at 1:200 dilution.

Analysis of phagocyte morphology

Pannoramic Viewer software was used to draw regions of interest in immunofluorescence brain sections stained for Iba1 and DAPI, and calculate the proportion of $Iba1^+$ signal occupied by the cell soma. Definiens Developer XD software was used to detect $Iba1^+$ $DAPI^+$ objects and export binary images. FIJI software was used to skeletonize binary image. Phagocyte endpoints, branching points and process length were then extracted using the FIJI plugin AnalyzeSkeleton. Average process length is normalized for soma size. Brain sections from WT non-carrier challenged mice served as control.

Quantification of synaptic terminals in the deep cerebellar nuclei

Pannoramic Viewer software (3DHISTECH) was used to calculate the perimeter of $LCMV^+$ neuronal somata and export deep cerebellar nuclei (DCN) regions. FIJI software was then used to enumerate perisomatic synaptophysin (SYP) positive boutons. For each mouse, 27 to 120 neurons were evaluated. To evaluate the density of presynaptic terminals (GAD65-67, VGLUT1) and postsynaptic terminals (gephyrin), DCN were drawn and exported with Pannoramic Viewer software and positive signals were quantified using a custom-made script, based on Cognition Network Language (Definiens Cognition Network Technology; Definiens Developer XD software).

Quantification of synaptic terminals in the hippocampal CA1 region

FIJI software was used to calculate the perimeter of pyramidal CA1 neurons and enumerate perisomatic synaptophysin (SYP) and GAD65-67 positive boutons. For each mouse, 40 to 50 neurons were evaluated. To evaluate the density of $VGLUT1^+$ presynaptic terminals and $gephyrin^+$ postsynaptic terminals, FIJI software was used draw a region of interest in the CA1 stratum pyramidale and stratum radiatum for gephyrin and VGLUT1 immunostaining respectively. FIJI software was then used to threshold single-plane confocal images acquired at 63 × magnification (Zeiss LSM800), and quantify the number of positive punctae inside the region of interest.

Quantification of phagocyte engulfing synaptic terminals

For each mouse, single-plane confocal images were acquired, sampling 0.1 to 0.8 mm^2 of DCN tissue at 63 × magnification. Imaris software (Bitplane) was used to build a colocalization channel of synaptophysin (SYP) and LAMP1 positive punctae. $Iba1^+$ cells showing colocalized SYP^+ $LAMP1^+$ punctae were counted as phagocytes engulfing synaptic terminals, expressed as number of SYP^+ $LAMP1^+$ phagocytes/mm^2.

Electron microscopy

Carrier and non-carrier mice were perfused 10 days after challenge with 2.5% glutaraldehyde and 2% paraformaldehyde in phosphate buffer (0.1M, pH 7.4). Brains were removed and 1 mm coronal slices were cut at the deep cerebellar nuclei level. Following the fixation, the tissue was processed through 2% osmium tetroxide and 4% uranyl acetate, then dehydrated in grades of alcohol. The samples were placed in propyleneoxide for 1 h subsequently infiltrated overnight in a 1:1 mixture of propyleneoxide and Epon resin. The following day the samples were embedded and polymerized at 60°C for 48 h. Ultrathin sections (about 60 nm) were cut on a Ultramicrotome, placed onto copper grids, stained with uranyl acetate and lead citrate and examined on a Philips CM10 transmission electron microscope.

Electrophysiology

In order to measure the miniature inhibitory postsynaptic currents (mIPSCs) in the DCN neurons, *ex-vivo* electrophysiological analyses were performed using 200 – 250 μM thick coronal cerebellum sections prepared from juvenile $Stat1^{+/+}$ non-carrier challenged, $Stat1^{+/+}$

and *Stat1*$^{fl/fl}$ carrier challenged mice. Mice were anaesthetized with isoflurane/O_2 and decapitated. Cerebellum sections were sliced using a cutting solution containing (in mM): 90.89 choline chloride, 24.98 glucose, 25 $NaHCO_3$, 6.98 $MgCl_2$, 11.85 ascorbic acid, 3.09 sodium pyruvate, 2.49 KCl, 1.25 NaH_2PO_4 and 0.50 $CaCl_2$. Brain slices were incubated in cutting solution for 20-30 minutes at 35°C and subsequently transferred in artificial cerebrospinal fluid (aCSF) containing (in mM): 119 NaCl, 2.5 KCl, 1.3 $MgCl_2$, 2.5 $CaCl_2$, 1.0 NaH_2PO_4, 26.2 $NaHCO_3$ and 11 glucose, bubbled with 95% O_2 and 5% CO_2. Whole-cell voltage clamp electrophysiological recordings were conducted at −70mV at 32°-34°C in aCSF (2 – 3 ml.min-1, submerged slices). mIPSCs were recorded from DCN neurons of the cerebellum in the presence of 3 mM kynurenic acid and TTX 1 μM. The patch pipettes were filled with (in mM): 30 KGlu, 100 KCl, 10.0 Creatin Phosphate, 4 $MgCl_2$, 1.1 EGTA, 3.4 Na_2-ATP, 0.1 Na_3-GTP, 5 HEPES, pH adjusted to 7.3, osmolarity to 288 mOsm.

In order to measure the spontaneous inhibitory postsynaptic currents (sIPSCs) in the hippocampal CA1 neurons, *ex-vivo* electrophysiological analyses were performed using 200 – 250 μM thick coronal hippocampal slices prepared from juvenile *Stat1*$^{+/+}$ non-carrier challenged, *Stat1*$^{+/+}$ and *Stat1*$^{fl/fl}$ carrier challenged mice. Mice were anaesthetized with isoflurane/O_2 and decapitated. Brains were sliced by using an artificial cerebrospinal fluid (aCSF) containing (in mM): 119 NaCl, 2.5 KCl, 1.3 $MgCl_2$, 2.5 $CaCl_2$, 1.0 NaH_2PO_4, 26.2 $NaHCO_3$ and 11 glucose, bubbled with 95% O_2 and 5% CO_2. Brain slices were incubated for 20-30 minutes at 35°C and subsequently slices were transferred at room temperature.

Both mIPSCs and sIPSCs were collected with a Multiclamp 700B-amplifier (Axon Instruments, Foster City, CA), filtered at 2.2 kHz, digitized at 5 Hz, and analyzed using MiniAnalysis 6 (Synaptosoft) software. Electrophysiology experiments were blinded to group assignment.

In situ hybridization

In situ hybridization (ISH) was performed on 4 μm thick brain sections from FFPE (formalin fixed paraffin embedded) tissue. Brain sections were applied on Superfrost slides and loaded onto the Discovery automated slide-processing system (Ventana Medical Systems, Inc). Baking and deparaffinization steps were performed on the instrument. ISH protocol was designed based on the standard protocol described in the manufacture's RiboMap application note. In brief, the first fixation step was performed using formalin-based RiboPrep reagent for 36 minutes at 37°C. Sections were then acid-treated using hydrochloride-based RiboClear reagent for 12 minutes at 37°C. Templates encompassing partial coding region for the human and mouse *Ccl2* mRNAs as well as for the mouse Cxcl10 mRNA were generated by PCR from respective synthetic DNAs (GenScript) using the following primers: for human *CCL2*, forward 5′CCGTAATACGACTCACTATAGGGAAAGTCTCTGCCGCCCTTC3′ and reverse 5′CCGATTTAGGTGACACTATAGAAT CGGAGTTTGGGTTTGCTTG3′; for mouse *Ccl2*, forward 5′CCGTAATACGACTCACTATAGGGCAGGTGTCCCAAAGAAGCTG3′ and reverse 5′-CCGATTTAGGTGACACTATAGAATGGATTCACAGAGAGGGAAAA-3′; for mouse *Cxcl10*, forward 5′CCGTAATAC GACTCACTATAGGGAGAGACATCCCGAGCCAAC-3′ and reverse 5′-CCGATTTAGGTGACACTATAGAAGAGGCTCTCTGCTGTC CATC-3′. mRNAs were detected with digoxygenin-tagged riboprobes transcribed from the antisense SP6 promoter. The slides were processed for protease digestion using Protease 1 reagent (0.5U/ml, Ventana Medical Systems) for 4 minutes at 37°C and incubated with antisense riboprobes (50-75 ng/slide) in RiboHybe hybridization buffer (Ventana Medical Systems, Inc) for 6 hours at 65°C after 8 minutes denaturing step at 75°C. After 3 stringency washes using 0.1 × RiboWash (Ventana Medical Systems) for 8 minutes each at 75°C, a second fixation step was performed using RiboFix (Ventana Medical Systems) reagent for 32 minutes at 37°C followed by incubation with Alkaline Phosphatase-labeled antidigoxigenin antibody (Roche, dilution 1:500) for 32 minutes at 37°C. The signal was detected automatically using the BlueMap NBT/BCIP substrate kit (Ventana Medical Systems, Inc.) for 6 hours at 37°C. Finally, the sections were counterstained with a nuclear red dye (Ventana Medical Systems, Inc) for 4 minutes before coverslipping in Aquatex (Merck).

RNAscope *in situ* hybridization

Fluorescent *in situ* hybridization (FISH) was done using the RNAscope Fluorescent Multiplex Kit V2 (323100, Advanced Cell Diagnostics, Inc.). *In situ* hybridization protocol was performed following recommended specifications for murine and human FFPE brain tissue. Probes against murine *Ccl2* (311791) and *Rbfox3*-C2 (NeuN) (313311-C2) were commercially available from Advanced Cell Diagnostics, Inc. RNAscope. FISH protocol on murine brains was followed by fluorescence immunostaining for LCMV nucleoprotein (LCMV). FISH on human FFPE brain tissues was performed using RNAscope Fluorescent Multiplex Kit V2 (323100, Advanced Cell Diagnostics, Inc.) along with human *Ccl2* (423811) probe according to manufacturer's protocol.

RiboTag-purification

Rpl22$^{HA/+}$x*Stat1*$^{+/+}$ carrier non-challenged, *Rpl22*$^{HA/+}$x*Stat1*$^{+/+}$ carrier challenged and *Rpl22*$^{HA/+}$x*Stat1*$^{fl/fl}$ carrier challenged mice were sacrificed 9 days after LCMVwt challenge. Immunoprecipitation and purification of ribosome associated RNA was performed essentially as described (Sanz et al., 2009). In brief, brains were isolated and stored in RNAlater solution (Thermofisher) at −80°C. Frozen tissue was transferred in Supplemented Homogenization Buffer (HB-S) and lysed with tissue lyser (QIAGEN). After lysis of the tissues and before immunopurification, a small fraction of lysate of each sample (input) was set aside and total RNA was extracted with TRIzol (Thermofisher) reagent followed by the RNeasy plus Micro Kit's procedure (QIAGEN). After immunopurification of the ribosome-associated RNAs, RNA quality was assessed on a 2100 BioAnalyzer (Agilent) and RNA amounts were quantified using the Qubit 2.0 Fluorometer (Life Technologies). The RNA integrity value (RIN) of the samples selected to be sequenced ranged between 7 and 9.2.

RNA-seq analysis

For sequencing, the RNA-samples were prepared using TruSeq Stranded Total RNA Library Prep Kit with Ribo-Zero Gold (Cat. No. RS-122-2301, RS-122-2302, and RS-122-2303) according to the manufacturer's protocol (Illumina). Samples were sequenced using the HiSeq 4000 (Illumina) (SE, 50 bp, ca. 30 Mio reads/sample). Independent biological replicates (n = 4-7) were analyzed for each group. Sequencing quality was checked and approved via the FastQC software (http://www.bioinformatics.babraham.ac.uk/projects/fastqc/). Sequence images were transformed to BCL files with the Illumina BaseCaller software and samples were demultiplexed to FASTQ files with CASAVA (version 1.8.2). Sequences were aligned to the reference genome of *Mus musculus* (UCSC genome assembly version mm10). Alignment was performed using the STAR alignment software (version 2.3.0e) allowing 2 mismatches within 50 bases. Subsequently, conversion of resulting SAM files to sorted BAM files, filtering of unique hits and counting was conducted with SAMtools (version 0.1.18) and HTSeq (version 0.6.1p1). Data was preprocessed and analyzed in the R/Bioconductor environment (https://www.bioconductor.org) using the DESeq2 package (version 1.8). Specifically, the data were normalized and tested for differentially expressed genes based on a generalized linear model likelihood ratio test assuming negative binomial data distribution. Candidate genes were filtered to a minimum of $\log_2$ 1.5-fold change and FDR-corrected $p < 0.05$. Gene annotation was performed using *Mus musculus* entries from Ensembl (https://www.ensembl.org/index.html) via the biomaRt package (version 2.24.0). For gene set enrichment analysis (GSEA), rank scores for differential mRNA expression between $Stat1^{+/+}$ and $Stat1^{fl/fl}$ carrier challenged groups were calculated as -log10 (p value) multiplied by the sign of the fold change such that upregulated genes had positive scores and downregulated genes had negative scores.

The java GSEA Desktop Application v2.2.1 was used to run the analysis and evaluate enriched GO and KEGG pathways. Normalized Enrichment Scores were calculated using the function GseaPreranked. Enrichment analysis for Gene Ontology (GO) was visualized using the Enrichment Map plugin (http://www.baderlab.org/Software/EnrichmentMap) for Cytoscape (version 3.6.0) (http://www.cytoscape.org/). Default settings were used for visualization, using p value < 0.01 and q-value < 0.01 and an overlap coefficient cutoff of 0.5. Enriched GO terms were uploaded to Enrichment Map, and a network graph was constructed. Nodes represent enriched GO terms and edges the degree of similarity between them using the overlap coefficient. After normalization of mean RPKM values, translatome data obtained from rLCMV-Cre carrier $Rpl22^{HA/+}$ mice and Thy1-Cre x $Rpl22^{HA/+}$ were compared with lists of specific neuronal and non-neuronal markers and plotted as heatmap. These lists were based on the markers described by Tasic and colleagues (Tasic et al., 2016) and augmented with known markers from the literature. Translatome datasets were also compared with single cell profiles of distinct neuronal and non-neuronal cells (microglia, astrocytes, oligodendrocytes, OPC and endothelial cells), available from the deposited GSE71585 (Tasic et al., 2016).

CART analysis

We performed multivariate analyses to evaluate which clinical and pathologic factors associated with epilepsia partialis continua (EPC) occurrence in Rasmussen's encephalitis (RE) patients. The classification and regression tree (CART) analysis was used to separate patients into different homogeneous risk groups and to determine predictors for drug-resistant epilepsy using the R language (R Development Core Team, 2017) together with the "rpart" package. Variables included in the CART analysis: sex, age at onset of RE and surgery, disease duration, region and side of resection, density of positive clusters for CD8, pSTAT1 and CCL2. ANOVA was selected as splitting method.

QUANTIFICATION AND STATISTICAL ANALYSIS

Data are shown as individual values. Horizontal lines represent mean ± SEM or median as reported in the figure legends. Normal distribution was confirmed using the D'Agostino–Pearson omnibus normality test where appropriate. To compare two groups, Student's t test (two-tailed) was used as indicate in figure legends (unpaired or paired). Variance between samples was tested using the Brown–Forsythe test. To compare multiple groups with equal variance, one-way ANOVA test was used while Kruskal–Wallis test was applied for groups with unequal variance. Post hoc tests for multiple comparisons are indicated in the figure legends. Linear regression and Pearson correlation coefficient R^2 were calculated.

In figures, asterisks denote statistical significance as *, $p < 0.05$; **, $p < 0.01$; ***, $p < 0.001$. Statistical analysis was performed in GraphPad Prism7.

DATA AND SOFTWARE AVAILABILITY

Software

All software is freely or commercially available and is listed in the Key Resources Table. Custom-made scripts used for cell detection and synaptic terminal quantification will be provided upon request to the Lead Contact.

Data Resources

The data that support the findings of this study are available from the corresponding authors upon request. The accession number for the RNA-seq data reported in this paper is GEO: GSE110593.

Supplemental Figures

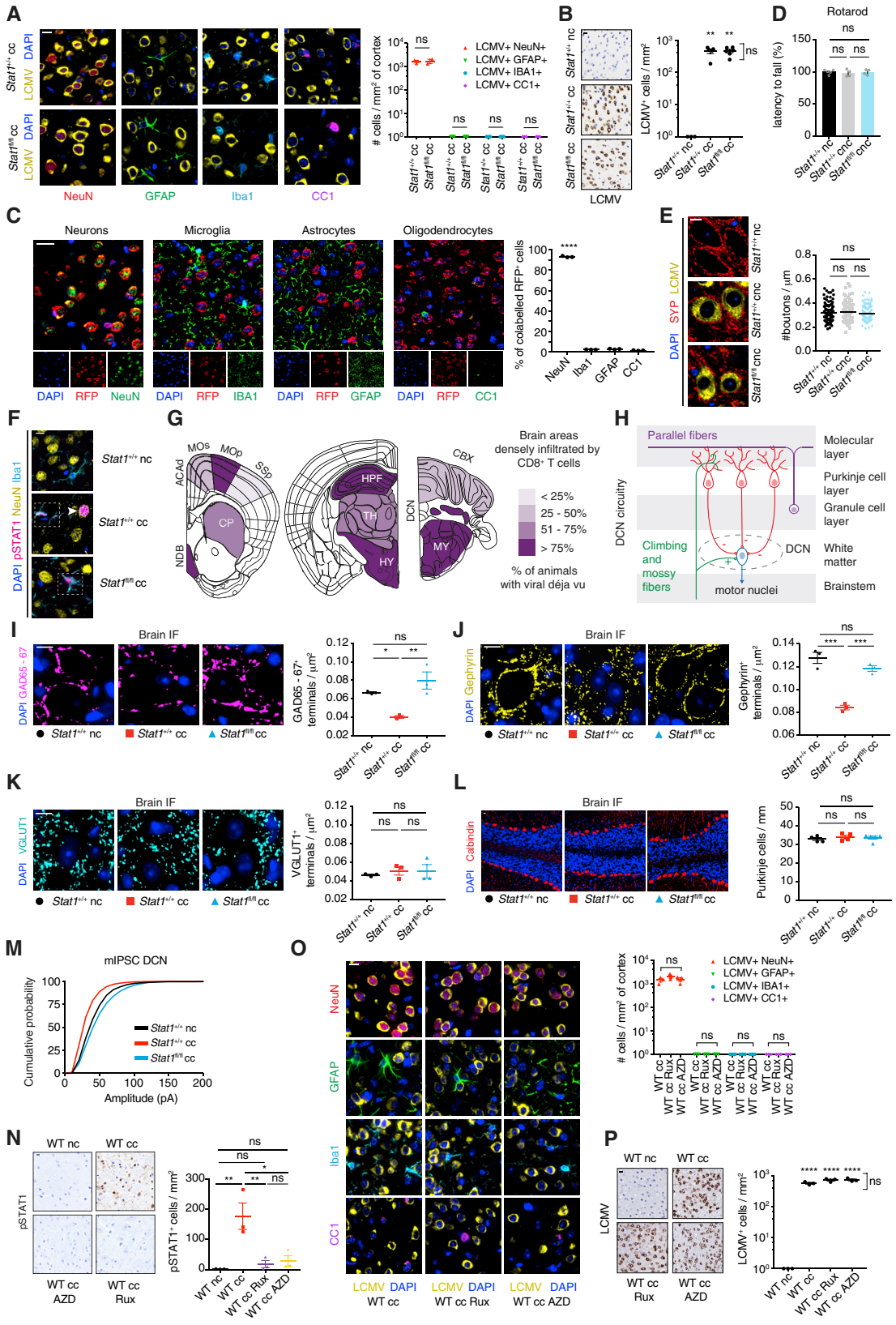

(legend on next page)

Figure S1. Neuronal STAT1-Dependent Decrease in Inhibitory Projections to DCN in Viral *Déjà Vu*, Related to Figure 1

(A) Representative images of co-immunostained sections for LCMV nucleoprotein (LCMV) together with neuronal (NeuN$^+$) or non-neuronal markers (GFAP for astrocytes, Iba1 for phagocytes and CC1 for oligodendrocytes) and quantification of positive cells in the brain cortex of *Stat1*$^{+/+}$ and *Stat1*$^{fl/fl}$ carrier mice (n = 3 mice per group)

(B) Representative images of immunostained brain sections for LCMV nucleoprotein (LCMV) and quantification thereof of indicated groups (*Stat1*$^{+/+}$ nc, n = 3; *Stat1*$^{+/+}$ cc, n = 5; *Stat1*$^{fl/fl}$ cc, n = 6).

(C) Reporter mice expressing tandem RFP after Cre-mediated recombination were neonatally infected with rLCMV-Cre. Representative images of one month old rLCMV-Cre reporter carrier mice immunostained for red fluorescent protein (RFP) along with NeuN, GFAP, Iba1, and CC1, and quantification of the proportion of co-labeled RFP$^+$ cells in n = 3 mice, evaluating n = 400 – 522 cells per brain).

(D-E) Rotarod performance (D) and axosomatic synaptic density (E) of non-challenged *Stat1*$^{+/+}$ and *Stat1*$^{fl/fl}$ carrier mice (cnc). *Stat1*$^{+/+}$ non-carrier mice (nc) were evaluated 9 days after challenge with LCMVwt (*Stat1*$^{+/+}$ nc, n = 5; *Stat1*$^{+/+}$ cnc and *Stat1*$^{fl/fl}$ cnc, n = 4). For synapse quantification, 3 mice per group were evaluated (n = 30 DCN neurons per mouse).

(F) Representative images of immunofluorescence co-staining for pSTAT1, NeuN (neurons) and Iba1 (phagocytes) on brain sections of indicated groups. Arrowhead indicates pSTAT1$^+$ neuron whereas dashed square indicates pSTAT1$^+$ phagocytes.

(G) Frequency map of affected brain regions with CD8$^+$ T cell infiltrates in *déjà vu* mice (n = 10). Listed areas: ACAd, Dorsal anterior cingulate area; CP, Caudatoputamen; CBX, Cerebellar cortex; DCN, Deep Cerebellar nuclei; HPF, Hippocampus formation; HY, Hypothalamus; MOs, Secondary Motor area; Mop, Primary Motor area; MY, Medulla; NDB, Diagonal band nucleus; SSp, Primary Somatosensory area; TH, Thalamus. Map adapted from *Allen Mouse Brain Atlas*.

(H) Schematic illustration of the cerebellar circuitry showing main inhibitory and excitatory projections to DCN cells.

(I-K) Representative images of Immunofluorescence stained DCN sections for the inhibitory presynaptic marker GAD65-67 (I), and post-synaptic marker gephyrin (J) and quantification thereof in the indicated groups. (K) Representative images of Immunofluorescence stained DCN sections for presynaptic excitatory marker VGLUT1 and quantification thereof in the indicated groups. The density of each synaptic marker was quantified as number of positive boutons per DCN area (μm^2), (n = 3 mice per group).

(L) Representative immunostained sections for calbindin$^+$ Purkinje cells in cerebellar cortex and quantification of cellular density in the indicated groups (*Stat1*$^{+/+}$ nc and *Stat1*$^{+/+}$ cc, n = 4; *Stat1*$^{fl/fl}$ cc, n = 5).

(M) Cumulative probability plot for mIPSC amplitude recorded from DCN neurons (n = 8 cells for *Stat1*$^{+/+}$ nc and *Stat1*$^{fl/fl}$ cc; n = 9 cells for *Stat1*$^{+/+}$ cc).

(N) Representative images of immunostained brain sections for pSTAT1 and quantification thereof in the indicated groups (n = 3 mice per group).

(O) Representative images of co-immunostained brain section for LCMV nucleoprotein (LCMV) together with neuronal and non-neuronal markers (as described in (A) and quantification of positive cells in the brain cortex of indicated groups (n = 3 mice per group).

(P) Representative images of immunostained brain sections for LCMV nucleoprotein (LCMV) and quantification thereof of indicated groups (n = 3 mice per group).

All panels: scale bars, 10 μm; Error bars, SEM; ***p < 0.001, **p < 0.01, *p < 0.05, ns, non-significant by one-way ANOVA test with Tukey correction for multiple comparisons. Representative data of at least four (A-P) independent experiments.

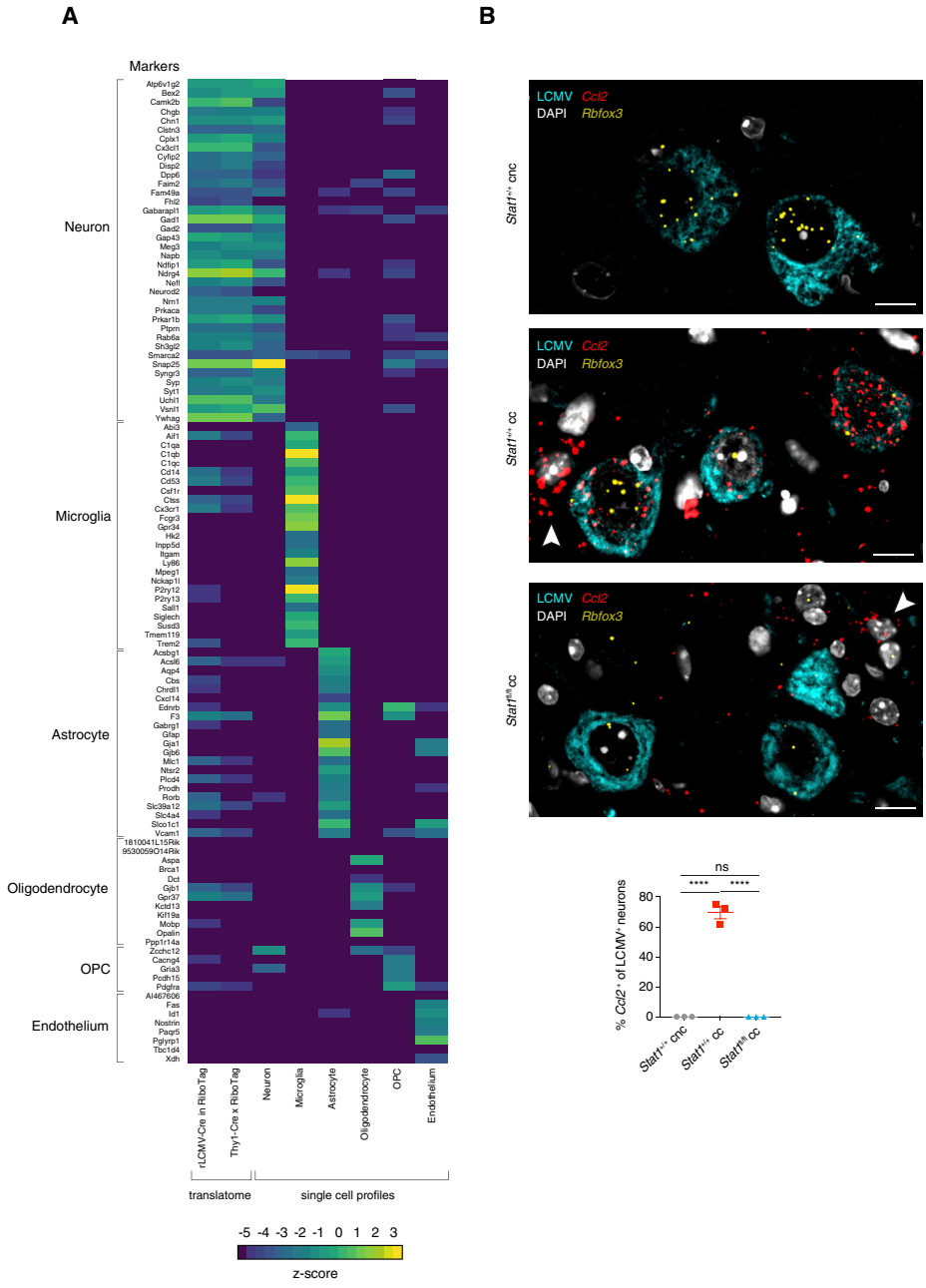

Figure S2. Enrichment of Neuronal Transcripts in rLCMV-Cre Carrier RiboTag Mice, Related to Figure 2

(A) Heatmaps of RNA-seq data show relative expression of transcripts obtained from rLCMV-Cre RiboTag carrier mice, Thy1-Cre x RiboTag mice compared to single cell transcriptome profiles of neurons, microglia, astrocytes, oligodendrocytes, OPC (oligodendrocyte progenitor cells) and endothelial cells (Tasic et al., 2016). The column for rLCMV-Cre RiboTag carrier mice represents the average value of n = 7 mice, whereas the column for Thy1-Cre x RiboTag mice the average value of n = 3 mice.

(B) *Stat1*$^{fl/fl}$ or *Stat1*$^{+/+}$ mice were neonatally infected with rLCMV-Cre. Carrier mice were challenged (cc) with LCMVwt i.v. at around 5 weeks of age. 9-10 days later, animals were sacrificed and brains were processed for histological analysis. Nonchallenged *Stat1*$^{+/+}$ carrier mice (cnc) served as controls. Representative sections co-stained for *Ccl2* and neuronal marker *Rbfox3* detected by RNAscope fluorescence *in situ* hybridization, and LCMV nucleoprotein (LCMV) by immunofluorescence. Arrowheads depict non-neuronal cells expressing *Ccl2* in challenged *Stat1*$^{fl/fl}$ and *Stat1*$^{+/+}$ carrier mice. Lower graph shows quantification of LCMV^{+} neurons expressing *Ccl2* (n = 3 mice per group). Scale bars, 10 μm. Error bars, SEM; ***p < 0.001, ns, non-significant by one-way ANOVA test with Tukey correction for multiple comparisons.

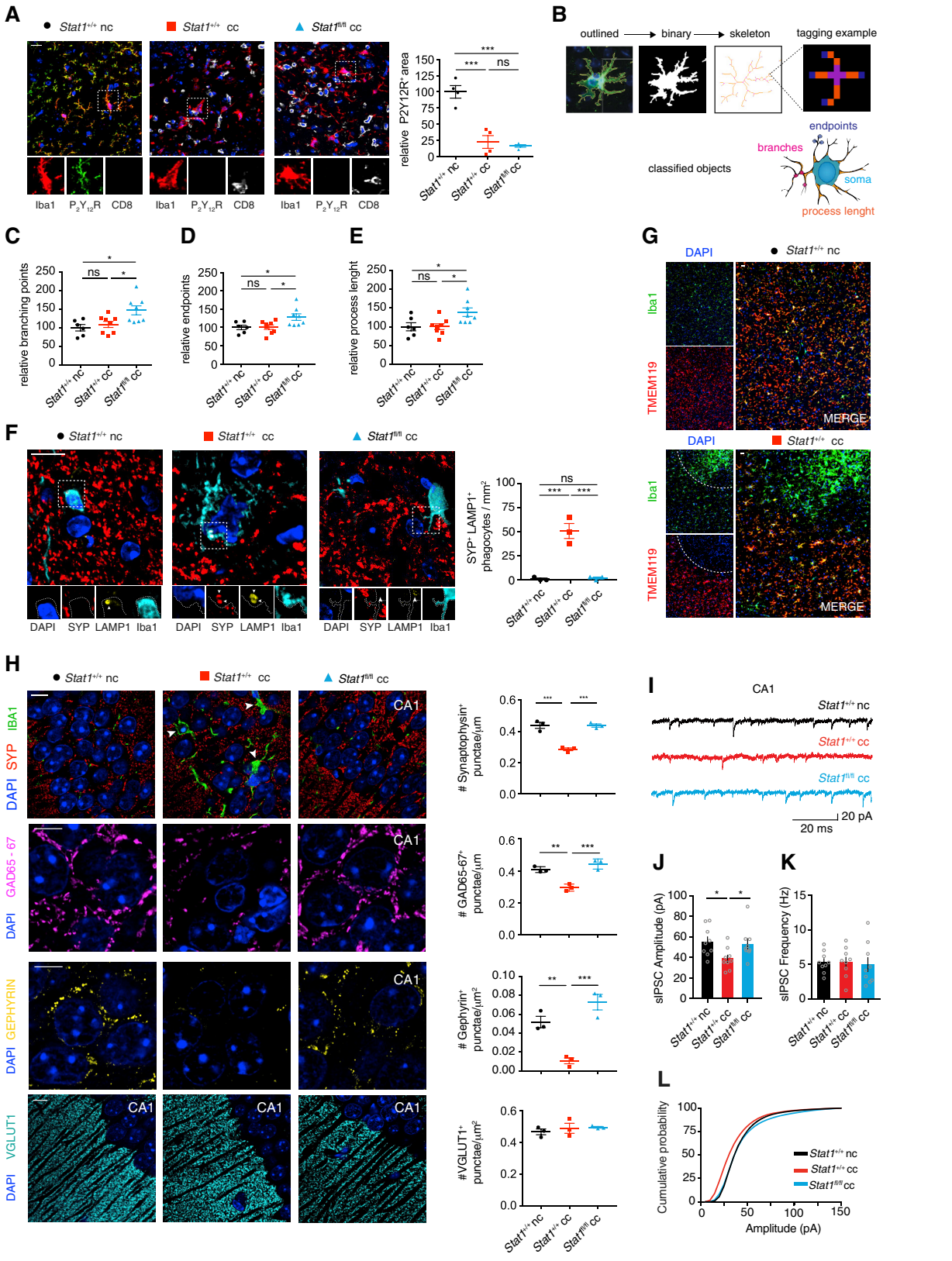

(legend on next page)

Figure S3. Activated CNS Phagocytes Show Ameboid Morphology and Engulfment of Synapses, Related to Figure 3

(A) Representative images of immunostained sections for Iba1, P2Y12R and CD8 of indicated groups, and quantification of $P2Y12R^+$ area in $Iba1^+$ CNS phagocytes.

(B-E) Representative $Iba1^+$ phagocyte outlined, converted to binary and skeletonized (B) to analyze branching points (C), endpoints (D) and process length (E) relative to $Stat1^{+/+}$ nc mice (n = 5 mice per group).

(F) Confocal immunofluorescence images for synaptic structures (SYP^+) localized in the lysosomal compartment ($LAMP1^+$) of CNS phagocytes (Iba1) in brain sections of $Stat1^{+/+}$ nc, $Stat1^{+/+}$ cc and $Stat1^{fl/fl}$ cc mice (n = 3 mice per group). Number of SYP^+ $LAMP1^+$ phagocytes per mm^2 are shown.

(G) Representative brain sections co-immunostained for the microglia specific marker TMEM119 and Iba1 showing infiltrates of amoeboid phagocytes (Iba1) lacking TMEM119 expression in WT carrier challenged mice.

(H) Confocal immunofluorescence images and quantification for presynaptic terminals (synaptophysin, SYP), inhibitory presynaptic terminals (GAD65-57), inhibitory postsynaptic terminals (gephyrin) and Iba1 for phagocytes stained in the pyramidal layer of CA1. Excitatory presynaptic terminals (VGLUT1) are shown in the stratum radiatum of hippocampal CA1 from brain sections of indicated groups (n = 3 mice per group).

(I-L) sIPSC sample traces (I), mean sIPSC amplitude (J), mean sIPSC frequency (K) and cumulative amplitude (L) in pyramidal hippocampal CA1 neurons; n = 9 cells per group.

All panels: scale bars, 10 μm; error bars, SEM; ***$p < 0.001$, **$p < 0.01$, *$p < 0.05$, one-way ANOVA with Tukey correction for multiple comparisons (A-H) or with Fisher's least significant difference (LSD) for multiple comparisons (J-K). The data shown are representative of four independent experiment.

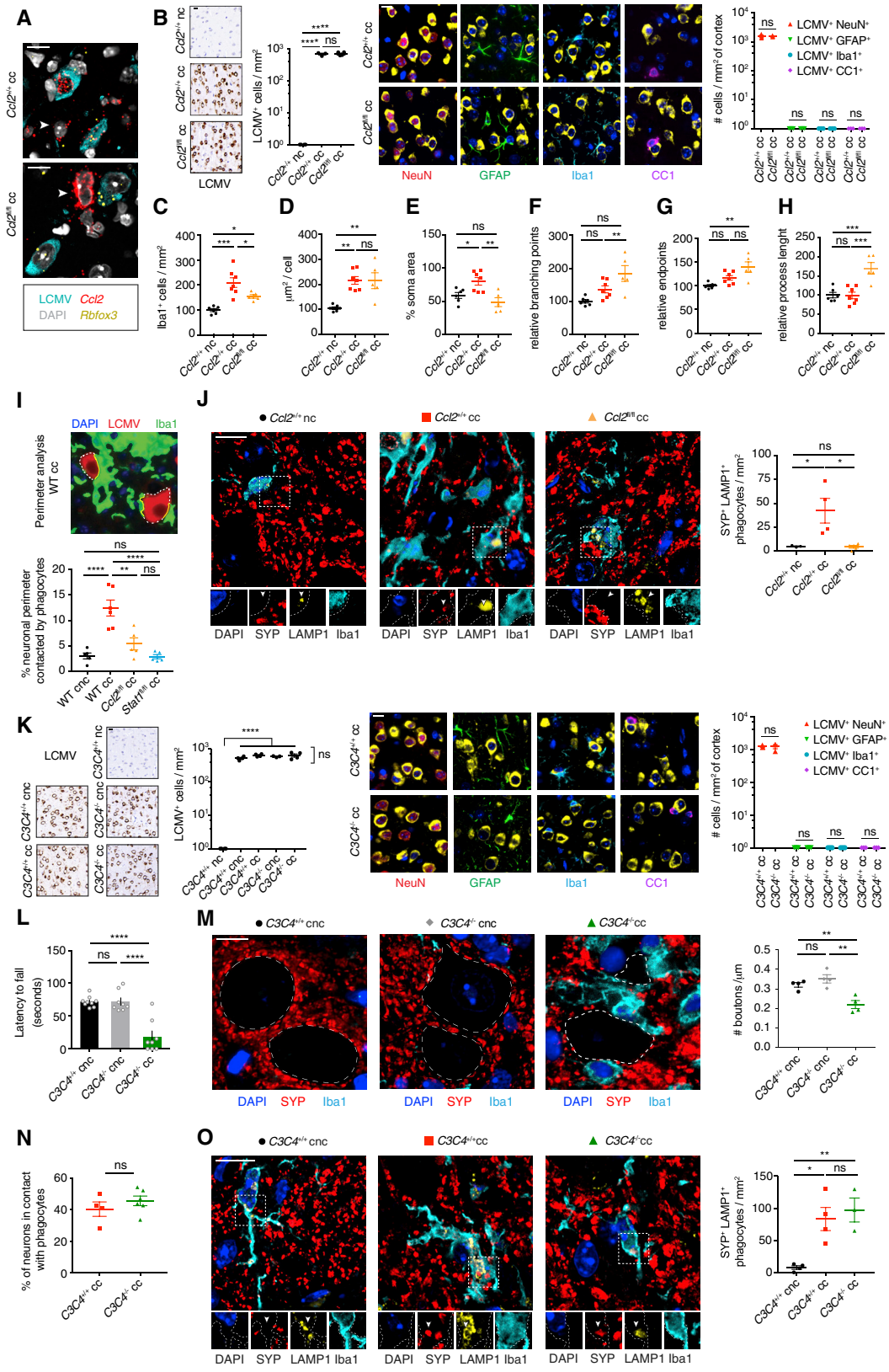
A
B
C
D
E
F
G
H
I
J
K
L
M
N
O
LCMV Ccl2
DAPI Rbfox3
LCMV
NeuN
GFAP
Iba1
CC1
DAPI SYP LAMP1 Iba1
Perimeter analysis WT cc
(legend on next page)

Figure S4. Effect of Abrogation of CCL2 or C3C4 on Phagocyte Features and Synaptic Stripping, Related to Figure 4

(A) *Ccl2*$^{fl/fl}$ or *Ccl2*$^{+/+}$ mice were neonatally infected with rLCMV-Cre. Carrier mice were challenged (cc) with LCMVwt i.v. at around 5 weeks of age. 9-10 days later, animals were sacrificed and brains were processed for histological analysis. Representative sections co-stained for *Ccl2* and neuronal marker *Rbfox3* by fluorescence RNAscope *in situ* hybridization, and LCMV nucleoprotein (LCMV) by immunofluorescence. Arrowheads depict non-neuronal cells expressing *Ccl2* in challenged *Ccl2*$^{fl/fl}$ and *Ccl2*$^{+/+}$ carrier mice.

(B) Quantification of viral burden by immunohistochemistry for LCMV nucleoprotein (LCMV) in brain sections of *Ccl2*$^{+/+}$ non-carrier challenged (*Ccl2*$^{+/+}$ nc, n = 4), *Ccl2*$^{+/+}$ cc (n = 3) and *Ccl2*$^{fl/fl}$ cc (n = 6), and evaluation of viral tropism by immunofluorescence co-staining for LCMV nucleoprotein together with neuronal (NeuN) and glial markers (GFAP for astrocytes, Iba1 for phagocytes and CC1 for oligodendrocytes) of indicated groups (n = 3 mice per group).

(C-H) Quantification of Iba1^{+} phagocytes indicating cell density (C), cellular size (μm^2/cell) (D), and soma proportion (E) from brain sections of indicated groups. Skeleton analysis showing branching points (F), endpoints (G) and process length (H) of phagocyte sampled from indicated groups (*Ccl2*$^{+/+}$ nc, n = 6, *Ccl2*$^{+/+}$ cc, n = 7, *Ccl2*$^{fl/fl}$ cc, n = 5). *Ccl2*$^{+/+}$ nc, served as control.

(I) Proportion of neuronal perimeter in contact with phagocytes on brain sections stained for Iba1, LCMV and DAPI. Wild-type (WT) carrier non-challenged (WT cnc, n = 5) served as control, WT carrier challenged (WT cc, n = 6), *Ccl2*$^{fl/fl}$ carrier challenged (*Ccl2*$^{fl/fl}$ cc, n = 5), *Stat1*$^{fl/fl}$ carrier challenged (*Stat1*$^{fl/fl}$ cc, n = 5).

(J) Confocal immunofluorescence images for synaptic structures (SYP^{+}) localized in the lysosomal compartment (LAMP1^{+}) of CNS phagocytes (Iba1) in brain sections of *Ccl2*$^{+/+}$ nc (n = 3), *Ccl2*$^{+/+}$ cc (n = 4), and *Ccl2*$^{fl/fl}$ cc (n = 5) mice. Number of SYP^{+} LAMP1^{+} phagocytes per mm^2 are shown.

(K) Quantification of viral burden by immunohistochemistry for LCMV nucleoprotein (LCMV) in brain sections of indicated groups (n = 3 – 4 mice per group), and evaluation of viral tropism by immunofluorescence co-staining for LCMV nucleoprotein together with neuronal (NeuN) and glial markers (GFAP for astrocytes, Iba1 for phagocytes and CC1 for oligodendrocytes) of rLCMV-Cre carrier *C3C4*$^{+/+}$ and *C3C4*$^{-/-}$ mice (n = 3 mice per group).

(L-M) Rotarod performance (L) and quantification of perisomatic synaptic density (M) of *C3C4*$^{+/+}$ and *C3C4*$^{-/-}$ carrier non-challenged (cnc) mice in comparison with *viral déja vu* diseased *C3C4*$^{+/+}$ carrier challenged mice (n = 8 - 9 mice per group for Rotarod test, n = 4 mice per group for evaluation of synaptic density).

(N) Proportion of neurons in contact with phagocytes in *C3C4*$^{+/+}$ and *C3C4*$^{-/-}$ carrier challenged mice (*C3C4*$^{+/+}$ cc, n = 4; *C3C4*$^{-/-}$, n = 6).

(O) Confocal immunofluorescence images for synaptic structures (SYP^{+}) localized in the lysosomal compartment (LAMP1^{+}) of CNS phagocytes (Iba1) in brain sections of *C3C4*$^{+/+}$ cnc (n = 4), *C3C4*$^{+/+}$ cc (n = 4), and *C3C4*$^{-/-}$ cc (n = 3) mice. Number of SYP^{+} LAMP1^{+} phagocytes per mm^2 are shown.

All panels: scale bars, 10 μm; error bars, SEM; ***p < 0.001, **p < 0.01, *p < 0.05, ns, non-significant by one-way ANOVA test with Tukey correction for multiple comparisons (B-M, O) and unpaired t test (N). The data shown are representative of two independent experiment (A-H, J-N) or pooled data of three independent experiments (I).

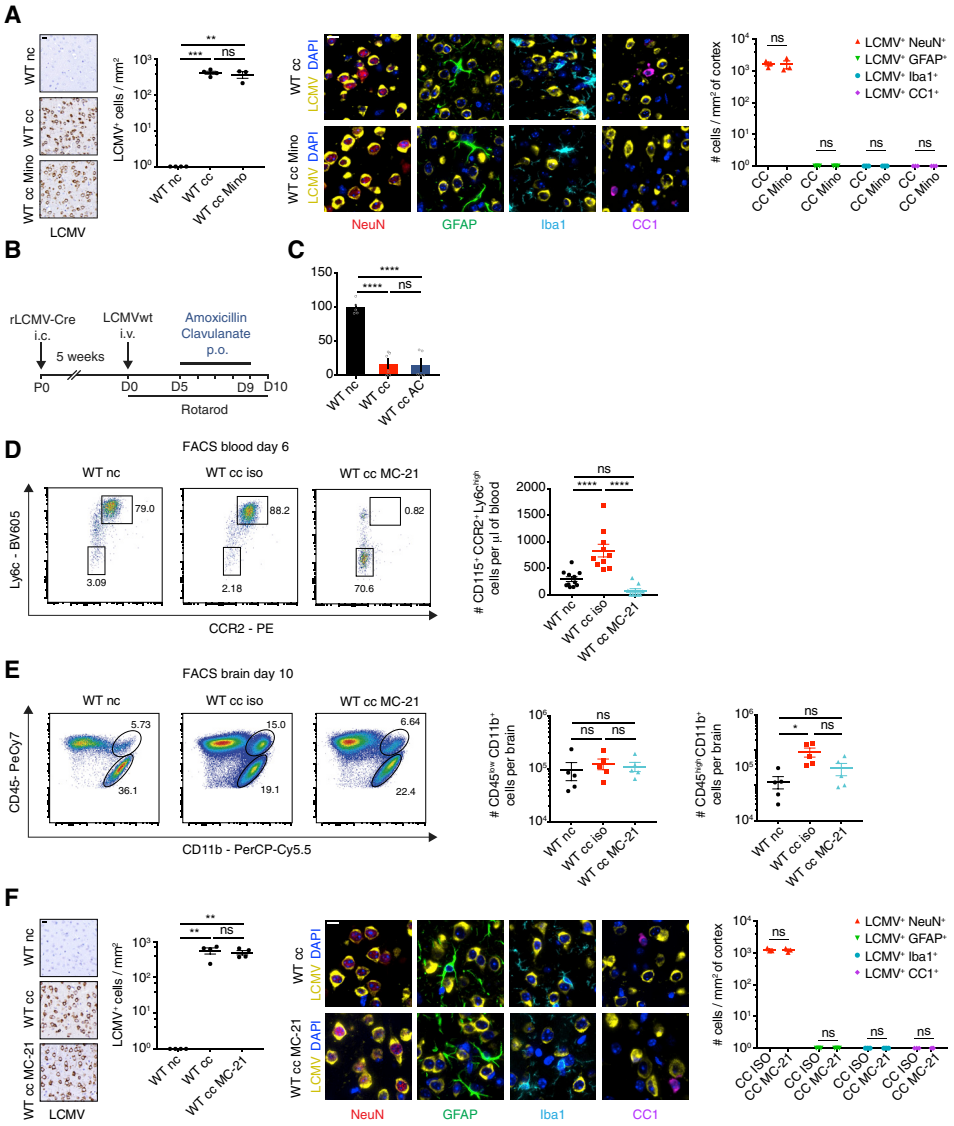

Figure S5. Inhibition of Brain Phagocytes and Depletion of CCR2+ Monocytes, Related to Figure 5

(A) Experimental setup as in Figure 5A. *Left:* Representative images and quantification of viral burden on brain sections evaluated by immunostaining for LCMV nucleoprotein (LCMV) of wild-type (WT) carrier challenged (cc) mice (n = 3 – 4 mice per group) treated with either minocycline (Mino) or PBS. *Right:* Representative images and quantification of viral tropism evaluated by immunofluorescence co-staining for LCMV nucleoprotein together with neuronal (NeuN) and glial markers (GFAP for astrocytes, Iba1 for phagocytes and CC1 for oligodendrocytes) in these mice (n = 3 mice per group).

(B) Experimental setup for administration of amoxicillin-clavulanate (AC, oral).

(C) Rotarod performance at peak of disease in mice from B; WT non-carrier challenged (WT nc, n = 5) mice served as control; WT cc (n = 6); WT cc AC (n = 5).

(D) FACS analysis of CD115^{+} Ly6c^{high} CCR2^{+} peripheral blood monocytes sampled from WT non-carrier challenged (WT nc), WT carrier challenged isotype-treated (WT cc iso) and MC21-treated (WT cc MC21) on day 6 after challenge.

(E) FACS analysis of CD45^{low} CD11b^{+} (microglia) and CD45^{high} CD11b^{+} (macrophage) peripheral blood monocytes sampled from indicated groups on D10 after challenge.

(F) Experimental setup as in Figure 5F. *Left:* Representative images and quantification of viral burden on brain sections evaluated by immunohistochemistry for LCMV nucleoprotein (LCMV) in MC-21- (WT cc MC-21) or isotype-treated (WT cc iso) carrier challenged mice (n = 4 mice per group). *Right:* Representative images and quantification of viral tropism evaluated by immunofluorescence co-staining for LCMV nucleoprotein together with neuronal (NeuN) and glial markers (GFAP for astrocytes, Iba1 for phagocytes and CC1 for oligodendrocytes) in these mice (n = 3 mice per group)

All panels: scale bars, 10 µm; error bars, SEM; ***p < 0.001, **p < 0.01, *p < 0.05, ns, non-significant by one-way ANOVA test with Tukey correction for multiple comparisons. The data shown are representative of two independent experiment.

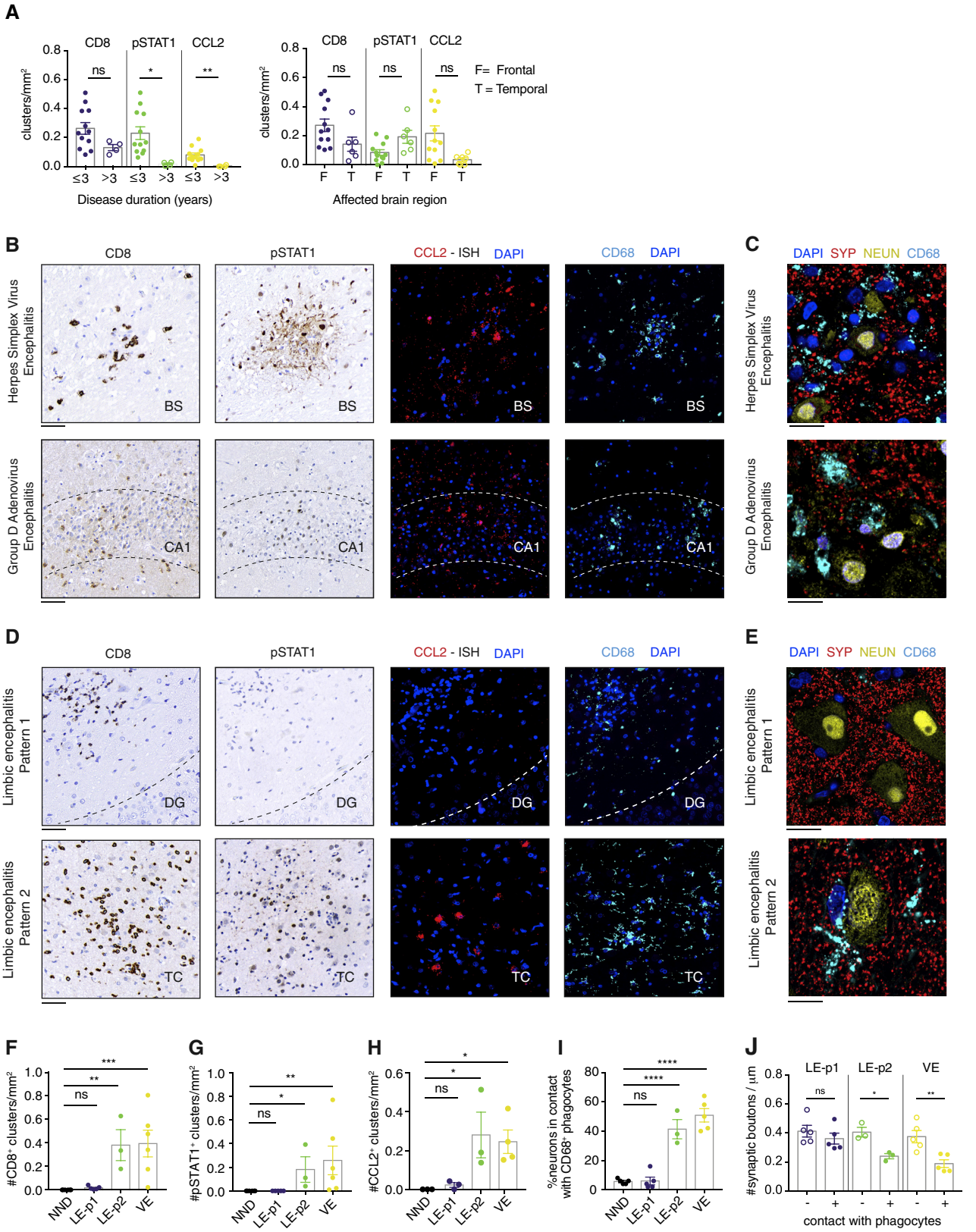

(legend on next page)

Figure S6. Neuronal pSTAT1 and Phagocyte-Associated Synaptic Loss in RE and Viral and Limbic Encephalitis, Related to Figure 6

(A) Quantification of $CD8^+$, $pSTAT1^+$ and CCL2+ cluster density in RE stratified by disease duration ($\leq$3 or > 3 years from disease onset to surgery) and by affected brain region. Symbols represents individual RE patients.

(B) Representative sections of viral encephalitis (Herpes simplex virus and Group D adenovirus encephalitis). Adjacent brain sections show immunostaining for cytotoxic T cells (CD8) and pSTAT1, fluorescence *in situ* hybridization (ISH) for *Ccl2* and immunofluorescence staining for $CD68^+$ phagocytes and nuclei counterstaining (DAPI). Dashed lines indicate the hippocampal CA1 region. BS, brainstem.

(C) Representative section as in (B) co-immunostained for neurons (NeuN), presynaptic terminal (synaptophysin, SYP), activated phagocytes (CD68) and nuclei (DAPI).

(D) Representative sections of limbic encephalitis (LE, *upper row* pattern 1 (p1), *lower row* pattern 2 (p2)). Representative images of adjacent sections were stained as in B. DG, dentate gyrus; TC, temporal cortex.

(E) Representative section as in D co-immunostained as in C.

(F-G) Quantification of $CD8^+$ (F), $pSTAT1^+$ (G) cluster density in tissue samples. NND, non-neurological disease (n = 6); LE-p1 (n = 5); LE-p2, (n = 3); VE, viral encephalitis (n = 5).

(H) Quantification of $CCL2^+$ cluster density in tissue samples evaluated by fluorescent *in situ* hybridization. NND (n = 3); LE-p1, LE-p1 (n = 3); LE-p2, LE-p2 (n = 3); VE, viral encephalitis (n = 4).

(I) Proportion of neurons in contact with $CD68^+$ phagocytes in indicated groups.

(J) Quantification of axosomatic synaptic density stratified by contact with phagocytes in indicated groups.

All panels, scale bar: 10 μm; error bars, SEM; All panels, ***$p < 0.001$, **$p < 0.01$, *$p < 0.05$, ns, not significant by unpaired t test (A), Kruskal–Wallis test with Dunn's correction for multiple comparisons (F-G), one-way ANOVA with Fisher's least significant difference (LSD) (H), Dunnett's (I) or Sidak's correction for multiple comparisons (J).

Table S1 – Top 100 upregulated transcripts by fold change and adjusted p-value in *Rpl22*$^{HA/+}$ x *Stat1*$^{+/+}$ carrier challenged RiboTag mice, Related to Figure 2.

Full list available at journal website: https://doi.org/10.1016/j.cell.2018.07.049

Rank	Ensembl gene id	Gene name	Description	log2 Fold Change	p-adj
1	ENSMUSG00000035692	Isg15	ISG15 ubiquitin-like modifier	4.29	4.59E-31
2	ENSMUSG00000082292	Gm12250	predicted gene 12250	4.27	2.05E-23
3	ENSMUSG00000041827	Oasl1	2'-5' oligoadenylate synthetase-like 1	4.26	1.11E-37
4	ENSMUSG00000078920	Ifi47	interferon gamma inducible protein 47	4.05	4.92E-28
5	ENSMUSG00000078853	Igtp	interferon gamma induced GTPase	4.02	1.83E-33
6	ENSMUSG00000029561	Oasl2	2'-5' oligoadenylate synthetase-like 2	4.01	3.43E-29
7	ENSMUSG00000030107	Usp18	ubiquitin specific peptidase 18	4.00	1.48E-54
8	ENSMUSG00000066861	Oas1g	2'-5' oligoadenylate synthetase 1G	3.97	5.41E-30
9	ENSMUSG00000054072	Iigp1	interferon inducible GTPase 1	3.93	1.34E-23
10	ENSMUSG00000020641	Rsad2	radical S-adenosyl methionine domain containing 2	3.93	9.73E-54
11	ENSMUSG00000068606	Gm4841	predicted gene 4841	3.93	1.23E-18
12	ENSMUSG00000034855	Cxcl10	chemokine (C-X-C motif) ligand 10	3.92	3.10E-27
13	ENSMUSG00000028270	Gbp2	guanylate binding protein 2	3.86	1.15E-26
14	ENSMUSG00000046718	Bst2	bone marrow stromal cell antigen 2	3.84	1.41E-39
15	ENSMUSG00000026104	Stat1	signal transducer and activator of transcription 1	3.84	3.94E-35
16	ENSMUSG00000073555	Gm4951	predicted gene 4951	3.80	4.25E-27
17	ENSMUSG00000024675	Ms4a4c	membrane-spanning 4-domains, subfamily A, member 4C	3.79	1.04E-29
18	ENSMUSG00000027514	Zbp1	Z-DNA binding protein 1	3.77	5.39E-20
19	ENSMUSG00000029605	Oas1b	2'-5' oligoadenylate synthetase 1B	3.75	3.24E-30
20	ENSMUSG00000000386	Mx1	MX dynamin-like GTPase 1	3.74	3.34E-26
21	ENSMUSG00000033576	Apol6	apolipoprotein L 6	3.72	1.24E-15
22	ENSMUSG00000033355	Rtp4	receptor transporter protein 4	3.72	9.12E-23
23	ENSMUSG00000035385	Ccl2	chemokine (C-C motif) ligand 2	3.71	2.70E-17
24	ENSMUSG00000046879	Irgm1	immunity-related GTPase family M member 1	3.68	5.76E-54
25	ENSMUSG00000067212	H2-T23	histocompatibility 2, T region locus 23	3.68	3.83E-71
26	ENSMUSG00000032661	Oas3	2'-5' oligoadenylate synthetase 3	3.67	1.55E-18
27	ENSMUSG00000052776	Oas1a	2'-5' oligoadenylate synthetase 1A	3.66	6.94E-22
28	ENSMUSG00000075602	Ly6a	lymphocyte antigen 6 complex, locus A	3.65	4.05E-20
29	ENSMUSG00000070427	Il18bp	interleukin 18 binding protein	3.63	8.27E-40

Rank	Ensembl gene id	Gene name	Description	log2 Fold Change	p-adj
30	ENSMUSG00000073490	AI607873	expressed sequence AI607873	3.61	9.84E-20
31	ENSMUSG00000066677	Pydc3	pyrin domain containing 3	3.61	8.23E-16
32	ENSMUSG00000079362	Gbp6	guanylate binding protein 6	3.59	1.13E-32
33	ENSMUSG00000035373	Ccl7	chemokine (C-C motif) ligand 7	3.58	7.67E-15
34	ENSMUSG00000078922	Tgtp1	T cell specific GTPase 1	3.56	3.72E-19
35	ENSMUSG00000016496	Cd274	CD274 antigen	3.54	1.21E-27
36	ENSMUSG00000037321	Tap1	transporter 1, ATP-binding cassette, sub-family B (MDR/TAP)	3.51	4.92E-28
37	ENSMUSG00000079017	Ifi27l2a	interferon, alpha-inducible protein 27 like 2A	3.50	1.91E-17
38	ENSMUSG00000078763	Slfn1	schlafen 1	3.49	4.33E-22
39	ENSMUSG00000044703	Phf11a	PHD finger protein 11A	3.48	6.24E-16
40	ENSMUSG00000026536	Mnda	myeloid cell nuclear differentiation antigen	3.48	4.65E-14
41	ENSMUSG00000025498	Irf7	interferon regulatory factor 7	3.48	4.24E-16
42	ENSMUSG00000073489	Ifi204	interferon activated gene 204	3.47	4.53E-19
43	ENSMUSG00000057346	Apol9a	apolipoprotein L 9a	3.44	3.17E-17
44	ENSMUSG00000040809	Chil3	chitinase-like 3	3.43	7.08E-11
45	ENSMUSG00000028037	Ifi44	interferon-induced protein 44	3.42	2.36E-13
46	ENSMUSG00000035186	Ubd	ubiquitin D	3.42	4.14E-12
47	ENSMUSG00000034438	Gbp8	guanylate-binding protein 8	3.41	6.92E-20
48	ENSMUSG00000024338	Psmb8	proteasome (prosome, macropain) subunit, beta type 8 (large multifunctional peptidase 7)	3.41	6.18E-30
49	ENSMUSG00000012519	Mlkl	mixed lineage kinase domain-like	3.40	5.88E-21
50	ENSMUSG00000054203	Ifi205	interferon activated gene 205	3.35	8.95E-15
51	ENSMUSG00000073491	Pydc4	pyrin domain containing 4	3.35	5.16E-15
52	ENSMUSG00000033213	AA467197	expressed sequence AA467197	3.35	4.74E-15
53	ENSMUSG00000079363	Gbp4	guanylate binding protein 4	3.35	2.37E-15
54	ENSMUSG00000043263	Pyhin1	pyrin and HIN domain family, member 1	3.35	2.38E-20
55	ENSMUSG00000069874	Irgm2	immunity-related GTPase family M member 2	3.34	3.41E-22
56	ENSMUSG00000041481	Serpina3g	serine (or cysteine) peptidase inhibitor, clade A, member 3G	3.33	3.97E-20
57	ENSMUSG00000068246	Apol9b	apolipoprotein L 9b	3.32	1.93E-14
58	ENSMUSG00000060550	H2-Q7	histocompatibility 2, Q region locus 7	3.30	6.16E-19
59	ENSMUSG00000074151	Nlrc5	NLR family, CARD domain containing 5	3.27	1.18E-20
60	ENSMUSG00000018899	Irf1	interferon regulatory factor 1	3.26	2.03E-31
61	ENSMUSG00000073409	H2-Q6	histocompatibility 2, Q region locus 6	3.25	2.15E-21

Rank	Ensembl gene id	Gene name	Description	log2 Fold Change	p-adj
62	ENSMUSG00000079419	Ms4a6c	membrane-spanning 4-domains, subfamily A, member 6C	3.24	6.49E-24
63	ENSMUSG00000057135	Scimp	SLP adaptor and CSK interacting membrane protein	3.22	1.13E-17
64	ENSMUSG00000000791	Il12rb1	interleukin 12 receptor, beta 1	3.20	1.18E-39
65	ENSMUSG00000039699	Batf2	basic leucine zipper transcription factor, ATF-like 2	3.20	1.00E-16
66	ENSMUSG00000029322	Plac8	placenta-specific 8	3.20	1.14E-22
67	ENSMUSG00000000204	Slfn4	schlafen 4	3.19	1.10E-09
68	ENSMUSG00000028268	Gbp3	guanylate binding protein 3	3.19	4.92E-20
69	ENSMUSG00000035929	H2-Q4	histocompatibility 2, Q region locus 4	3.18	2.28E-26
70	ENSMUSG00000035208	Slfn8	schlafen 8	3.17	4.40E-26
71	ENSMUSG00000074896	Ifit3	interferon-induced protein with tetratricopeptide repeats 3	3.16	4.82E-45
72	ENSMUSG00000037849	Gm4955	predicted gene 4955	3.16	7.90E-11
73	ENSMUSG00000096727	Psmb9	proteasome (prosome, macropain) subunit, beta type 9 (large multifunctional peptidase 2)	3.14	1.34E-23
74	ENSMUSG00000078921	Tgtp2	T cell specific GTPase 2	3.14	1.49E-16
75	ENSMUSG00000090942	F830016B08Rik	RIKEN cDNA F830016B08 gene	3.14	1.16E-10
76	ENSMUSG00000034422	Parp14	poly (ADP-ribose) polymerase family, member 14	3.13	3.47E-30
77	ENSMUSG00000048852	Gm12185	predicted gene 12185	3.13	1.99E-09
78	ENSMUSG00000010358	Ifi35	interferon-induced protein 35	3.11	3.94E-40
79	ENSMUSG00000054588			3.11	4.37E-12
80	ENSMUSG00000059089	Fcgr4	Fc receptor, IgG, low affinity IV	3.10	3.25E-13
81	ENSMUSG00000061232	H2-K1	histocompatibility 2, K1, K region	3.10	2.40E-30
82	ENSMUSG00000035273	Hpse	heparanase	3.10	5.40E-19
83	ENSMUSG00000002944	Cd36	CD36 antigen	3.08	4.40E-19
84	ENSMUSG00000003484	Cyp4f18	cytochrome P450, family 4, subfamily f, polypeptide 18	3.08	5.83E-12
85	ENSMUSG00000034459	Ifit1	interferon-induced protein with tetratricopeptide repeats 1	3.08	1.80E-19
86	ENSMUSG00000063268	Parp10	poly (ADP-ribose) polymerase family, member 10	3.07	8.18E-36
87	ENSMUSG00000091649	Phf11b	PHD finger protein 11B	3.07	1.75E-20
88	ENSMUSG00000025279	Dnase1l3	deoxyribonuclease 1-like 3	3.06	7.62E-13
89	ENSMUSG00000002831	Plin4	perilipin 4	3.05	6.57E-14
90	ENSMUSG00000030921	Trim30a	tripartite motif-containing 30A	3.05	6.87E-22
91	ENSMUSG00000040253	Gbp7	guanylate binding protein 7	2.99	1.90E-19
92	ENSMUSG00000040483	Xaf1	XIAP associated factor 1	2.99	2.38E-50
93	ENSMUSG00000070327	Rnf213	ring finger protein 213	2.95	2.28E-30

Rank	Ensembl gene id	Gene name	Description	log2 Fold Change	p-adj
94	ENSMUSG00000040264	Gbp2b	guanylate binding protein 2b	2.95	3.63E-15
95	ENSMUSG00000022126	Irg1	immunoresponsive gene 1	2.93	3.65E-09
96	ENSMUSG00000030713	Klk7	kallikrein related-peptidase 7 (chymotryptic, stratum corneum)	2.93	2.56E-09
97	ENSMUSG00000060183	Cxcl11	chemokine (C-X-C motif) ligand 11	2.92	5.40E-10
98	ENSMUSG00000055172	C1ra	complement component 1, r subcomponent A	2.91	4.09E-33
99	ENSMUSG00000032690	Oas2	2'-5' oligoadenylate synthetase 2	2.90	2.70E-19
100	ENSMUSG00000039899	Fgl2	fibrinogen-like protein 2	2.89	2.12E-24

Table S2 – Top 100 downregulated transcripts by fold change and adjusted p-value in *Rpl22*$^{HA/+}$ x *Stat1*$^{+/+}$ carrier challenged RiboTag mice, Related to Figure 2.

Full list available at journal website: https://doi.org/10.1016/j.cell.2018.07.049

Rank	Ensembl gene id	Gene name	Description	log2 Fold Change	p-adj
1	ENSMUSG00000082431	Tdpx-ps1	thioredoxin peroxidase, pseudogene 1	-5.04	6.03E-50
2	ENSMUSG00000067189	Gm7335	predicted gene 7335	-5.04	1.67E-27
3	ENSMUSG00000093077			-2.53	1.18E-13
4	ENSMUSG00000038242	Aox4	aldehyde oxidase 4	-2.30	1.52E-29
5	ENSMUSG00000045337	Defb11	defensin beta 11	-2.14	1.10E-05
6	ENSMUSG00000093098			-1.99	1.76E-09
7	ENSMUSG00000015852	Fcrls	Fc receptor-like S, scavenger receptor	-1.96	5.25E-16
8	ENSMUSG00000035896	Rnase1	ribonuclease, RNase A family, 1 (pancreatic)	-1.91	3.38E-07
9	ENSMUSG00000093337			-1.89	4.82E-10
10	ENSMUSG00000046341	Gm11223	predicted gene 11223	-1.86	1.62E-03
11	ENSMUSG00000086324	Gm15564	predicted gene 15564	-1.81	2.73E-07
12	ENSMUSG00000035202	Lars2	leucyl-tRNA synthetase, mitochondrial	-1.81	7.03E-08
13	ENSMUSG00000081824	BC002163	cDNA sequence BC002163	-1.73	3.48E-03
14	ENSMUSG00000076258	Gm23935	predicted gene, 23935	-1.72	1.95E-06
15	ENSMUSG00000044734	Serpinb1a	serine (or cysteine) peptidase inhibitor, clade B, member 1a	-1.69	2.70E-17
16	ENSMUSG00000031410	Nxf7	nuclear RNA export factor 7	-1.66	4.40E-04
17	ENSMUSG00000000402	Egfl6	EGF-like-domain, multiple 6	-1.58	1.81E-07
18	ENSMUSG00000079733			-1.55	4.11E-03
19	ENSMUSG00000045027	Prss22	protease, serine 22	-1.55	2.18E-08
20	ENSMUSG00000059343	Aldoart1	aldolase 1 A, retrogene 1	-1.55	5.13E-03
21	ENSMUSG00000028174	Rpe65	retinal pigment epithelium 65	-1.52	1.53E-04
22	ENSMUSG00000096780	Tmem181b-ps	transmembrane protein 181B, pseudogene	-1.52	5.19E-03
23	ENSMUSG00000061062	Gm10093	predicted pseudogene 10093	-1.52	4.83E-03
24	ENSMUSG00000030048	Gkn3	gastrokine 3	-1.51	1.71E-03
25	ENSMUSG00000029371	Cxcl5	chemokine (C-X-C motif) ligand 5	-1.47	5.34E-04
26	ENSMUSG00000071035	Gm5499	predicted pseudogene 5499	-1.44	3.47E-03
27	ENSMUSG00000037086	Prr32	proline rich 32	-1.44	2.14E-08
28	ENSMUSG00000096255	Dynlt1b	dynein light chain Tctex-type 1B	-1.43	2.68E-06
29	ENSMUSG00000085069	Gm13111	predicted gene 13111	-1.42	7.29E-07

Rank	Ensembl gene id	Gene name	Description	log2 Fold Change	p-adj
30	ENSMUSG00000086815	3110082J24Rik	RIKEN cDNA 3110082J24 gene	-1.40	9.30E-03
31	ENSMUSG00000059195	Gm12715	predicted gene 12715	-1.39	3.20E-04
32	ENSMUSG00000022209	Dhrs2	dehydrogenase/reductase member 2	-1.39	2.39E-03
33	ENSMUSG00000051606	2010001K21Rik	RIKEN cDNA 2010001K21 gene	-1.34	1.44E-02
34	ENSMUSG00000085067	Gm15631	predicted gene 15631	-1.34	4.48E-06
35	ENSMUSG00000061808	Ttr	transthyretin	-1.33	3.04E-14
36	ENSMUSG00000085527	Gm15535	predicted gene 15535	-1.32	2.29E-02
37	ENSMUSG00000055368	Slc6a2	solute carrier family 6 (neurotransmitter transporter, noradrenalin), member 2	-1.32	1.92E-03
38	ENSMUSG00000073940	Hbb-bt	hemoglobin, beta adult t chain	-1.31	5.11E-03
39	ENSMUSG00000052234	Epx	eosinophil peroxidase	-1.31	1.84E-04
40	ENSMUSG00000086900	Kcnab3os	potassium voltage-gated channel, shaker-related subfamily, beta member 3, opposite strand	-1.30	2.36E-02
41	ENSMUSG00000097727	F630040K05Rik	RIKEN cDNA F630040K05 gene	-1.30	4.61E-03
42	ENSMUSG00000082235	Gm13326	predicted gene 13326	-1.29	2.94E-02
43	ENSMUSG00000097276	4930525G20Rik	RIKEN cDNA 4930525G20 gene	-1.28	4.88E-03
44	ENSMUSG00000054944	5330416C01Rik	RIKEN cDNA 5330416C01 gene	-1.28	1.34E-02
45	ENSMUSG00000097692	A230060F14Rik	RIKEN cDNA A230060F14 gene	-1.27	1.66E-02
46	ENSMUSG00000086688	Gm11560	predicted gene 11560	-1.26	4.58E-02
47	ENSMUSG00000021823	Vcl	vinculin	-1.25	3.68E-03
48	ENSMUSG00000087611	4930458D05Rik	RIKEN cDNA 4930458D05 gene	-1.25	1.21E-02
49	ENSMUSG00000096146	Kcnj11	potassium inwardly rectifying channel, subfamily J, member 11	-1.24	9.86E-05
50	ENSMUSG00000072944	Nup62cl	nucleoporin 62 C-terminal like	-1.24	3.56E-05
51	ENSMUSG00000087541	Hopxos	HOP homeobox, opposite strand	-1.23	5.33E-03
52	ENSMUSG00000038239	Hrc	histidine rich calcium binding protein	-1.23	3.14E-02
53	ENSMUSG00000029420	Rimbp2	RIMS binding protein 2	-1.23	6.35E-05
54	ENSMUSG00000026413	Pkp1	plakophilin 1	-1.22	2.42E-02
55	ENSMUSG00000045903	Npas4	neuronal PAS domain protein 4	-1.21	3.83E-02
56	ENSMUSG00000083094	Gm4908	predicted gene 4908	-1.21	1.27E-02
57	ENSMUSG00000033730	Egr3	early growth response 3	-1.21	1.13E-02
58	ENSMUSG00000058523	Mup5	major urinary protein 5	-1.20	4.94E-02
59	ENSMUSG00000087478	4930506C21Rik	RIKEN cDNA 4930506C21 gene	-1.19	1.32E-04
60	ENSMUSG00000000889	Dbh	dopamine beta hydroxylase	-1.19	2.77E-03
61	ENSMUSG00000074056			-1.18	9.38E-03

Rank	Ensembl gene id	Gene name	Description	log2 Fold Change	p-adj
62	ENSMUSG00000071015	Gm136	predicted gene 136	-1.17	3.54E-02
63	ENSMUSG00000086213	A330040F15Rik	RIKEN cDNA A330040F15 gene	-1.17	3.92E-03
64	ENSMUSG00000085260	Med9os	mediator complex subunit 9, opposite strand	-1.17	7.05E-03
65	ENSMUSG00000090534	Gm4675	predicted gene 4675	-1.17	4.24E-03
66	ENSMUSG00000098035	Gm5335	predicted gene 5335	-1.17	2.87E-02
67	ENSMUSG00000031111	Igsf1	immunoglobulin superfamily, member 1	-1.17	4.04E-08
68	ENSMUSG00000074899	Sptbn5	spectrin beta, non-erythrocytic 5	-1.16	3.43E-04
69	ENSMUSG00000001494	Sost	sclerostin	-1.15	4.23E-02
70	ENSMUSG00000031074	Fgf3	fibroblast growth factor 3	-1.15	1.46E-03
71	ENSMUSG00000067215	Usp51	ubiquitin specific protease 51	-1.15	1.71E-02
72	ENSMUSG00000074758	Gm5535	predicted gene 5535	-1.14	2.45E-02
73	ENSMUSG00000052301	Doc2a	double C2, alpha	-1.14	3.06E-06
74	ENSMUSG00000070306	Ccdc153	coiled-coil domain containing 153	-1.14	2.97E-06
75	ENSMUSG00000030054	Gp9	glycoprotein 9 (platelet)	-1.13	2.40E-02
76	ENSMUSG00000021541	Trpc7	transient receptor potential cation channel, subfamily C, member 7	-1.13	4.90E-08
77	ENSMUSG00000097338	Gm2464	predicted gene 2464	-1.12	3.85E-03
78	ENSMUSG00000072473	1700024G13Rik	RIKEN cDNA 1700024G13 gene	-1.11	1.73E-02
79	ENSMUSG00000041717			-1.11	2.16E-03
80	ENSMUSG00000074865	Zfp934	zinc finger protein 934	-1.11	3.50E-02
81	ENSMUSG00000045114	Prrt2	proline-rich transmembrane protein 2	-1.10	2.06E-03
82	ENSMUSG00000091898	Tnnc1	troponin C, cardiac/slow skeletal	-1.10	3.37E-05
83	ENSMUSG00000030792	Dkkl1	dickkopf-like 1	-1.10	3.02E-08
84	ENSMUSG00000037185	Krt80	keratin 80	-1.09	1.92E-02
85	ENSMUSG00000026976	Pax8	paired box 8	-1.09	4.08E-02
86	ENSMUSG00000044676	Zfp612	zinc finger protein 612	-1.09	5.11E-03
87	ENSMUSG00000025488	Cox8b	cytochrome c oxidase subunit VIIIb	-1.09	1.20E-02
88	ENSMUSG00000060424	Pantr1	POU domain, class 3, transcription factor 3 adjacent noncoding transcript 1	-1.09	2.92E-06
89	ENSMUSG00000063297	Luzp2	leucine zipper protein 2	-1.09	2.03E-02
90	ENSMUSG00000015829	Tnr	tenascin R	-1.09	4.58E-03
91	ENSMUSG00000030486	Zfp108	zinc finger protein 108	-1.09	1.75E-03
92	ENSMUSG00000021940	Ptpn20	protein tyrosine phosphatase, non-receptor type 20	-1.08	4.91E-02
93	ENSMUSG00000021609	Slc6a3	solute carrier family 6 (neurotransmitter transporter, dopamine), member 3	-1.08	2.60E-03
94	ENSMUSG00000055197	Fev	FEV (ETS oncogene family)	-1.07	2.75E-02
95	ENSMUSG00000026969	Fam166a	family with sequence similarity 166, member A	-1.07	2.92E-02
96	ENSMUSG00000072974	Gm4787	predicted gene 4787	-1.06	4.32E-02
97	ENSMUSG00000059246	Foxb1	forkhead box B1	-1.06	4.40E-03
98	ENSMUSG00000058420	Syt17	synaptotagmin XVII	-1.06	7.89E-03
99	ENSMUSG00000024395	Lims2	LIM and senescent cell antigen like domains 2	-1.05	5.09E-07
100	ENSMUSG00000074273			-1.05	3.95E-02

Table S3 – Gene Ontology (GO) gene sets enriched in *Stat1*$^{+/+}$ versus *Stat1*$^{fl/fl}$ carrier challenged mice by GSEA analysis with GO modules. Annotation of Enrichment Map nodes, false discovery rate (FDR) q-value <0.05, p-value <0.01 in *Stat1*$^{+/+}$ versus *Stat1*$^{fl/fl}$ carrier challenged.

Cluster	Gene Ontology Gene Sets	SIZE	ES	NES	q-value
Defense response to other organism	Regulation of multi organism process	83	0.570431	1.8753458	0.0101
	Defense response to other organism	96	0.61203	2.0279803	0.0006
	Regulation of defense response	145	0.514755	1.7398173	0.0499
	Negative regulation of multi organism process	22	0.720159	2.0469508	0.0005
	Response to biotic stimulus	165	0.532978	1.8128475	0.0208
	Regulation of symbiosis encompassing mutualism through parasitism	37	0.72937	2.256392	0.0000
	Defense response	229	0.53231	1.8298094	0.0171
Antiviral response	Regulation of viral genome replication	17	0.814234	2.1271625	0.0000
	Defense response to virus	51	0.735283	2.337653	0.0000
	Response to virus	68	0.670684	2.1929545	0.0000
	Negative regulation of viral genome replication	26	0.776341	2.2406237	0.0000
	Negative regulation of viral process	16	0.685275	1.8455129	0.0138
Immune response	Innate immune response	142	0.607403	2.0357122	0.0006
	Immune effector process	119	0.57014	1.8789309	0.0104
	Regulation of innate immune response	89	0.57935	1.8891438	0.0089
	Immune response	236	0.54251	1.8505226	0.0140
	Negative regulation of immune response	37	0.678094	2.0312166	0.0007
Interferon gamma and interferon type I response	Negative regulation of type I interferon production	15	0.847699	2.2566185	0.0000
	Regulation of type I interferon production	38	0.613075	1.854307	0.0146
	Interferon gamma mediated signaling pathway	25	0.699788	2.035723	0.0007
	Response to interferon gamma	44	0.671744	2.0884304	0.0000
	Response to type I interferon	31	0.837703	2.4849362	0.0000
	Cellular response to interferon gamma	38	0.641395	1.9291822	0.0048
Cytokine and chemokine signaling	Cytokine mediated signaling pathway	100	0.631767	2.1247213	0.0000
	Response to cytokine	142	0.578476	1.922064	0.0051
	Cellular response to cytokine stimulus	120	0.597768	2.0036106	0.0011
	Negative regulation of cytokine production	29	0.596446	1.7668067	0.0365
Antigen processing and presentation (see next page)	Protein catabolic process	59	0.556078	1.7834975	0.0303
	Protein ubiquitination	56	0.563138	1.7809906	0.0306
	Antigen processing and presentation via MHC class I	20	0.693678	1.9263308	0.0047
	Regulation of protein modification by small protein conjugation or removal	40	0.599116	1.8513186	0.0143

Cluster	Gene Ontology Gene Sets	SIZE	ES	NES	q-value
	Negative regulation of protein modification by small protein conjugation or removal	16	0.786957	2.0863414	0.0000
	Positive regulation of ligase activity	16	0.685275	1.8455129	0.0138
	Regulation of protein ubiquitination involved in ubiquitin dependent protein catabolic process	16	0.747788	1.998166	0.0013
	Protein modification by small protein conjugation or removal	69	0.569563	1.8535887	0.0142
Synaptic activity	Synapse part	43	-0.3788	-2.1788204	0.0101
	Exocytic vesicle	19	-0.51464	-2.4543877	0.0026
	Modulation of synaptic transmission	25	-0.44612	-2.2485328	0.0080
	Presynapse	23	-0.52556	-2.4930341	0.0026
	Regulation of synapse structure or activity	17	-0.48087	-2.0876966	0.0208
	Synaptic signaling	30	-0.41507	-2.1991942	0.0104
	Synapse	55	-0.33751	-2.2775242	0.0089
	Regulation of neurotransmitter level	16	-0.55494	-2.4667056	0.0027
Disconnected nodes (not shown)	Transferase activity transferring glyvcosil groups	21	0.653455	1.8479416	0.0137
	Cell morphogenesis involved in neuron differentiation	16	-0.6151	-2.6821442	0.0011
	Myelin sheath	17	-0.62499	-2.7597141	0.0000

Table S4 – Biological pathways enriched in *Stat1*$^{+/+}$ versus *Stat1*$^{fl/fl}$ carrier challenged mice by GSEA analysis with KEGG modules. Top 20 pathways of GSEA using gene sets derived from KEGG pathway database with false discovery rate (FDR) q-value <0.05 in *Stat1*$^{+/+}$ versus *Stat1*$^{fl/fl}$ carrier challenged.

Rank	KEGG pathways	SIZE	NES	FDR q-val	Top 10 genes in core enrichment
1	JAK STAT SIGNALING PATHWAY	100	1.756817	0.00266545	IL12RB1, STAT1, STAT2, IRF9, SOCS1, IL10RA, STAT3, SOCS3, IL21R, CSF2RB
2	ANTIGEN PROCESSING AND PRESENTATION	36	1.751578	0.00133273	TAPBP, TAP2, TAP1, B2M, PSME2, PSME1, LGMN, CTSS, CIITA, IFI30, CD74, CTSB
3	COMPLEMENT AND COAGULATION CASCADES	38	1.738737	0.00175913	SERPING1, C2, C1QA, F13A1, C1QB, C1QC, C5AR1, CFB, C3AR1, C4B, SERPINE1, PLAU
4	CYTOSOLIC DNA SENSING PATHWAY	38	1.677005	0.00887567	DDX58, CXCL10, ZBP1, IRF7, CASP1, AIM2, NFKBIA, RIPK3, PYCARD, TMEM173
5	TOLL LIKE RECEPTOR SIGNALING PATHWAY	83	1.672281	0.008312	STAT1, CXCL10, TLR7, IRF7, CD40, MYD88, IRF5, CD86, TLR3, CXCL11, CXCL9, TLR4
6	PRIMARY IMMUNODEFICIENCY	28	1.653865	0.01194378	TAP2, TAP1, CD40, ADA, CIITA, IL2RG, PTPRC, BTK, BLNK, CD3D, LCK
7	RIG I LIKE RECEPTOR SIGNALING PATHWAY	50	1.628828	0.018949	DDX58, ISG15, IFIH1, TRIM25, CXCL10, DHX58, IRF7, NFKBIA, TMEM173, IKBKE, CASP8, TNF
8	PROTEASOME	44	1.624859	0.01779461	PSMB8, PSMB10, PSMB9, PSME2, PSME1
9	LYSOSOME	110	1.616313	0.01875102	CTSZ, LGMN, CTSS, SLC11A1, CTSC, LAPTM5, NPC2, TCIRG1, CTSD, LAMP2, CTSH, GNS
10	LEISHMANIA INFECTION	50	1.613047	0.01775985	STAT1, MYD88, NCF1, CYBA, ITGB2, NCF2, TLR4, NFKBIA, TLR2, PTPN6, NCF4, TNF
11	NATURAL KILLER CELL MEDIATED CYTOTOXICITY	82	1.596716	0.02402304	SH3BP2, ITGAL, FCER1G, VAV1, HCST, TNFSF10, ITGB2, RAC2, NFATC1, IFNAR2, PLCG2, PIK3CG
12	CYTOKINE CYTOKINE RECEPTOR INTERACTION	164	1.591419	0.02469856	IL12RB1, CXCL10, IL10RA, CCL2, CD40, CCL7, CXCL16, CXCL11, TNFSF10, IL21R, CSF2RB, IL3RA

13	B CELL RECEPTOR SIGNALING PATHWAY	71	1.59084	0.02312113	LYN, INPP5D, CD72, VAV1, CARD11, PIK3AP1, NFKBIA, RAC2, NFATC1, PLCG2, PIK3CG, PTPN6
14	NOD LIKE RECEPTOR SIGNALING PATHWAY	48	1.589323	0.02179329	CCL2, CCL7, CASP1, NOD1, TNFAIP3, BIRC3, RIPK2, NFKBIA, PSTPIP1, PYCARD, CCL8, CARD9
15	HEMATOPOIETIC CELL LINEAGE	53	1.586595	0.02146773	CD36, CD37, CD44, IL3RA, CD3G, CD3D, CD34, CD33, CD22, TNF, CSF1, CD3E
16	CHEMOKINE SIGNALING PATHWAY	152	1.578879	0.02328962	STAT1, STAT2, CXCL10, HCK, CCL2, LYN, CCL7, STAT3, CXCL16, VAV1, NCF1, CXCL11
17	P53 SIGNALING PATHWAY	59	1.576515	0.02316658	SHISA5, CDK1, CDKN2A, CCNB2, RRM2, CDKN1A, BID, IGFBP3, SERPINE1, GTSE1, CASP8, FAS
18	SYSTEMIC LUPUS ERYTHEMATOSUS	44	1.555876	0.0334506	TRIM21, C2, C1QA, CD40, C1QB, CD86, C1QC, C4B, FCGR2B, TNF
19	FC GAMMA R MEDIATED PHAGOCYTOSIS	89	1.545015	0.03875691	HCK, LYN, INPP5D, VAV1, NCF1, DOCK2, VASP, RAC2, PTPRC, PLCG2, PIK3CG, LAT
20	ABC TRANSPORTERS	33	1.541276	0.03889912	TAP2, TAP1, ABCA1, ABCC3

Table S5 – Human brain tissues of patients with Rasmussen's encephalitis and non-neurological disease.

Relevant information on patients with Rasmussen's encephalitis (RE) and non-neurological disease (NND) used in this study: sex, age at onset and surgery, epilepsy duration, region and side of resection and type of seizure when applicable. Abbreviations used: not applicable (n.a.), right (R), left (L), epilepsia partialis continua (EPC), focal aware seizure (FAS), focal onset with impaired awareness (FOIA), generalized tonic clonic seizure (GTCS).

ID	Diagnosis	Sex	Age at onset (years)	Age at surgery (years)	Epilepsy duration (years)	Region of resection	Side of resection	Seizure type
E1	RE	M	n.a.	14	n.a.	temporal	R	EPC
E2	RE	F	9	9	0.3	temporal	L	FOIA
E3	RE	F	n.a.	5	n.a.	frontal	L	n.a.
E4	RE	F	n.a.	7	n.a.	frontal	R	EPC
E5	RE	F	4.0	6	2	frontal	R	EPC
E6	RE	F	3.5	5	1.5	frontal	L	FOIA; GTCS
E7	RE	M	5	6	0.6	frontal	R	EPC
E8	RE	M	5	7	2	frontal	R	EPC
E9	RE	F	2	3	1	frontal	L	FAS
E10	RE	F	3	6	3	frontal	R	EPC
E11	RE	M	5	6	0.8	temporal	R	EPC
E12	RE	F	2	3	1	temporal	L	EPC
E13	RE	F	2	3	1	frontal	R	EPC
E14	RE	M	3.5	5	1.5	frontal	L	EPC
E15	RE	M	6	8	2	temporal	L	EPC
E16	RE	M	5	9	4	frontal	L	FAS, FOIA
E17	RE	F	6	15	9	frontal, temporal	L	aura, myoclonia, FAS
E18	RE	F	33	42	9	temporal	R	FAS
E19	RE	M	3	14	11	frontal	R	n.a.
E20	RE	F	n.a.	7	n.a.	frontal, temporal	L	n.a.
N1	NND	F	n.a.	31	n.a.	frontal	n.a.	n.a.
N2	NND	M	n.a.	43	n.a.	frontal	n.a.	n.a.
N3	NND	M	n.a.	19	n.a.	frontal	n.a.	n.a.
N4	NND	F	n.a.	6	n.a.	frontal, temporal	n.a.	n.a.
N5	NND	F	n.a.	9	n.a.	frontal, temporal	n.a.	n.a.
N6	NND	M	n.a.	14	n.a.	frontal, temporal	n.a.	n.a.

Table S6 – Human brain tissues of patients with limbic and viral encephalitis

Relevant information on patients with limbic encephalitis (LE) and viral encephalitis (VE) used in this study: sex, age at surgery (years), region of resection and additional clinical data. Abbreviations: Herpes simplex virus 1 (HSV1).

ID	Diagnosis	Sex	Age at surgery	Resected region	Additional clinical data
LE1	Limbic encephalitis	F	21	temporal	-
LE2	Limbic encephalitis	F	47	temporal	-
LE3	Limbic encephalitis	F	78	temporal	-
LE4	Limbic encephalitis	M	34	temporal	-
LE5	Limbic encephalitis	M	32	temporal	History of seminoma
LE6	Limbic encephalitis	F	36	temporal	-
LE7	Limbic encephalitis	F	52	temporal	anti-GAD autoantibodies
LE8	Limbic encephalitis	F	50	temporal	-
VE1	Herpes simplex virus encephalitis	F	46	temporal	HSV1+
VE2	Herpes simplex virus encephalitis	F	1	temporal	HSV1+
VE3	Herpes simplex virus encephalitis	M	61	brainstem	HSV1+
VE4	Herpes simplex virus encephalitis	F	74	temporal	HSV1+
VE5	Herpes simplex virus encephalitis	F	60	temporal	HSV1+
VE6	Group D adenovirus encephalitis	F	47	temporal	Group D adenovirus +